2-2012

A Comprehensive Model of Human Neuromuscular Function During Repeated Isometric Contractions: Predicting the Effect of Age on Fatigue

Damien Mark Callahan
University of Massachusetts Amherst, damcall@gmail.com

A COMPREHENSIVE MODEL OF HUMAN NEUROMUSCULAR FUNCTION DURING REPEATED ISOMETRIC CONTRACTIONS: PREDICTING THE EFFECT OF AGE ON FATIGUE

A Dissertation Presented

by

Damien M. Callahan

Submitted to the Graduate School of the
University of Massachusetts Amherst in partial fulfillment
of the requirements for the degree of

DOCTOR OF PHILOSOPHY

February 2012

Kinesiology

**A COMPREHENSIVE MODEL OF HUMAN NEUROMUSCULAR FUNCTION
DURING REPEATED ISOMETRIC CONTRACTIONS: PREDICTING THE
EFFECT OF AGE ON FATIGUE**

A Dissertation Presented

by

Damien M. Callahan

Approved as to style and content by:

_____
Jane A. Kent-Braun, Chair

_____
Edward P. Debold, Member

_____
John Staudenmayer, Member

_____
Brian Umberger, Member

_____
Jane A. Kent-Braun, Graduate Program Director
Department of Kinesiology

ACKNOWLEDGMENTS

ABSTRACT

**A COMPREHENSIVE MODEL OF HUMAN NEUROMUSCULAR FUNCTION
DURING REPEATED ISOMETRIC CONTRACTIONS: PREDICTING THE
EFFECT OF AGE ON FATIGUE**

FEBRUARY 2012

DAMIEN CALLAHAN, B.S., BOSTON UNIVERSITY

M.S., UNIVERSITY OF MASSACHUSETTS AMHERST

Ph.D., UNIVERSITY OF MASSACHUSETTS AMHERST

Directed by: Professor Jane A. Kent-Braun

Repeated or prolonged activation of skeletal muscle results in an acute decline in

the muscle's ability to produce force, which is typically referred to as fatigue. Muscle

fatigue is likely related to the by-products of cellular metabolism, alterations in neural

activation and diminished membrane excitability that have been shown to accompany

repeated contractions. However, the complicated etiology of the fatigue process makes it

difficult to understand the relative influence of these physiological responses.

Computational modeling of the skeletal muscle response to repeated activation is an

appealing means of gaining insight into the mechanisms of muscle fatigue. A reasonably

comprehensive model would include components that represent α motor neurons and

populations of muscle fibers that reflect the range of metabolic and contractile

characteristics known to exist in human skeletal muscle. Consideration of joint and

connective tissue mechanical properties will add translational value by predicting whole

joint segment behavior that can be validated by in vivo experimentation. The proposed

dissertation project involved the development of a computational model incorporating multiple components meant to represent the function of the intact neuromuscular system. The complete model combines previously-validated models of neural activation and contractile behavior with a control function that attempts to match torque output to a pre-determined task. The model uses experimentally-derived functions describing metabolic cost and force inhibition to predict the loss of force generating capacity during repeated activation. Once tested using data from a group of adult men, the parameters of this model were altered to reflect age-related changes in the human neuromuscular system. The model's ability to predict the well-established phenomenon of age-related fatigue resistance during isometric contractions was then tested. The results from this series of studies support the utility of a computational approach to the investigation of muscle fatigue, and provide useful tools for future studies.

PREFACE

Chapters 1-3 of the following document were included in the dissertation proposal document submitted to the University of Massachusetts Graduate School in March, 2011. Chapters 4, 5, and 6 correspond to hypotheses 1-3 in the proposal document, respectively while chapter 7 is a summary of the work contained therein. The focus of Chapter 4 has been altered to include aspects of hypothesis 2, after agreement between myself and the committee that this arrangement was more conducive to the logical progression of ideas proposed in this dissertation. In accordance with the wishes of the committee, chapters 4, 5, and 6 are formatted as manuscripts to expedite their submission for peer-review.

TABLE OF CONTENTS

LIST OF TABLES

LIST OF FIGURES

CHAPTER 1

INTRODUCTION

<u>**Development of the Problem**</u>

The mechanisms of skeletal muscle fatigue, or the acute loss of force-generating capacity in response to repeated or prolonged contractions, is difficult to define. Voluntary activation of skeletal muscle requires the coordination of multiple systems (Figure 1). Perturbations to the function of any one of these systems may contribute to fatigue.

Beginning in the central nervous system (Figure 1, 1), excitatory action potentials are generated in the motor cortex of the brain, and are propagated along cortico-spinal tracts to groups of α motor neurons in the spinal cord. These motor neurons are characterized by a range of recruitment thresholds and activation patterns. Activation of a given motor neuron (Figure 1, 2) causes the axon of that neuron to depolarize, thereby propagating an action potential down its length. Each axon is connected to hundreds or thousands of skeletal muscle fibers (cells). The motor neuron
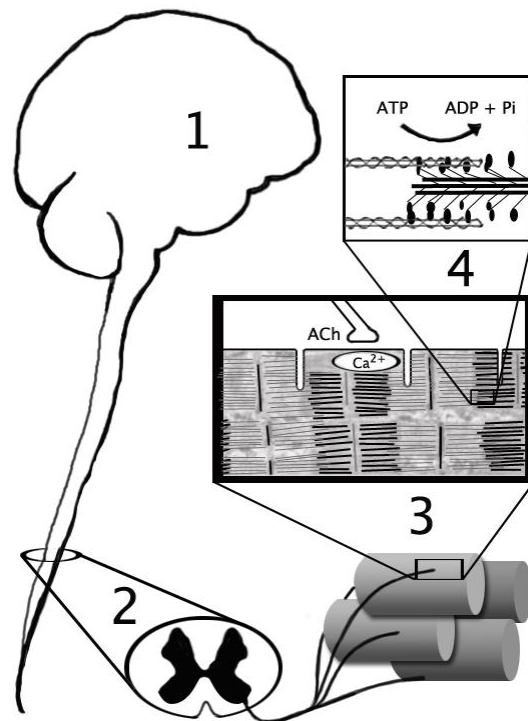
Figure 1.1
Schematic of the events leading to muscle activation. Beginning with 1. Cortical excitation, 2. Motor unit activation, 3. Depoloarization of the sarcolemma and subsequent calcium release, 4. Actin-Myosin binding, dephosphorylation of ATP and force generation.

1

and all of the muscle fibers it innervates compose a single motor unit. Voluntary force is thought to be regulated primarily by the number of motor units recruited and the rate at which activated motor units depolarize (78).

Translation of a nerve action potential to muscle contraction is initiated by the release of acetylcholine (ACh) from the terminal ends of the motor axon (Figure 1, 3) to receptors on the muscle membrane. Binding of ACh to these receptors causes depolarization of the muscle membrane. This signal is propagated to the transverse tubules, which in turn triggers release of Ca^{2+} from the sarcoplasmic reticulum. Released into the sarcoplasm, Ca^{2+} binds to troponin, which leads to tropomyosin moving on actin, and exposure of the myosin-binding site on actin (Figure 1, 4). Myonsin, once bound to actin, undergoes a conformational change that results in force generation. When adenosine triphosphate (ATP) binds to the actin-myosin complex, myosin dissociates from actin. Hydrolysis of ATP by myosin ATPase causes the myosin head to revert to its original shape. The process of actin-myosin binding, ATP hydrolysis and force generation will repeat, provided Ca^{2+} remains in the sarcoplasm to keep the myosin binding site exposed. Repeated muscle activations will cause an increase in adosine diphophate (ADP), inorganic phosphate (Pi) and proton (H^+) concentrations due to the dephosphorylation of ATP and increased metabolism required to maintain ATP supply.

Even with this simplified summary of events, it is clear that the process of force generation is complicated. Because reductions in force generating capacity can result from alterations at any point along this pathway, understanding the distinct physiological cause(s) of muscle fatigue is inherently difficult. This difficulty is illustrated by the fact that many studies focus on the outcome of neuromuscular activation (force) and, perhaps,

one or two of the many steps along the pathway of force production due to the complexity of simultaneously assessing the entire pathway in vivo.

Several studies have reported that older adults fatigue less than their younger counterparts when performing repeated isometric contractions. Although the phenomenon of age-related fatigue resistance is not always observed, the magnitude of age-related differences in fatigue tend to be more pronounced during prolonged, isometric contractions (11; 13) and attenuated or reversed during repeated dynamic contractions (5; 69; 117). Unique physiological mechanisms that might explain age-related fatigue resistance under certain conditions have been identified over the years (27; 103; 105; 110; 111; 113). However, multiple mechanisms likely contribute to fatigue simultaneously. As a result, disentangling their relative contributions to the task-specific phenomenon of age-related fatigue resistance presents a significant challenge.

A number of investigators have used computational modeling to successfully predict the net behavior of the intact neuromuscular system (15; 58; 75; 121; 187). Specific models have been constructed and tested that accurately predict behavior of individual components of the neuromuscular system. These modeled behaviors include, but are not limited to, the activation (59), discharge, and spatial distribution (58) of motor units; depolarization of the sarcolemma (54); calcium kinetics (131; 187); acto-myosin binding kinetics (70; 83; 166); and control of oxidative phosphorylation by ADP (94). Still other models have been developed that predict the response of some of these components to repeated activation (40; 41; 43; 62; 63; 74; 128; 190). However, rarely have multiple physiological components been included in the same model (63), and no

models investigating the response of skeletal muscle to repeated contraction specifically address the physiological changes that occur with old age.

Although data exist that accurately quantify age-related changes in neuromuscular physiology for a variety of experimental conditions, the task remains to combine them in a comprehensive model of neuromuscular function that accurately predicts known responses of young and aged individuals. A model that responds to excitation by simulating α motor neuron activation, intracellular Ca^{2+} dynamics, and force generation could be used to evaluate hypotheses related to altered neuromuscular function in aging humans. Extending the function of such a model to include production of, and sensitivity to, the fatigue-inducing byproducts of cellular metabolism would allow testing of novel hypotheses related to age-related fatigue resistance. Simulations designed, for example, to measure the impact of lower motor unit discharge rate, altered recruitment strategies, increased contractile economy or decreased reliance on glycolysis could be run using this single model. Most important, similar experiments would be impossible in vivo.

Statement of the Problem

The interrelated nature of physiological processes thought to influence fatigue make their relative influence on fatigue difficult to discern in vivo. Quantifying the extent to which these processes differ between younger and older individuals, and further, how they might mediate age-related differences in fatigue is an even greater challenge. While in vitro experimentation can provide explicit details about isolated systems, and in vivo studies typically describe the combined function of multiple systems, each are limited in addressing the phenomenon of age-related fatigue resistance. Model simulations on the other hand, are commonly used to predict the responses of

4

complicated systems whose interrelated components might preclude direct measurement or control. Currently, no model exists that describes neuromuscular function and the response to repeated activation while accounting for known age-related changes in neuromuscular physiology.

<u>Hypotheses</u>

A computational model of neuromuscular function will be constructed based on data from the literature and experimentally-derived values from a population of healthy young men. *Hypothesis 1:* Beginning with a maximal excitation signal, this model will accurately predict maximal ankle dorsiflexion torque within one standard deviation of the experimental data.

The same model of neuromuscular function tested for Hypothesis 1 will be modified to predict fatigue during a bout of six, 12-second maximum voluntary contractions each separated by 12 seconds of rest (111; 113). The model's accuracy will be evaluated by comparing predicted fatigue to literature values (111; 113). ***Hypothesis 2:*** With repeated maximal activation, the model will predict fatigue within one standard deviation of experimental values.

Parameters in the completed model from Hypothesis 2 will be adjusted to reflect age-related differences in neuromuscular function. These will include slowed rates of force relaxation, lowered maximal discharge rates, and lesser accumulation of $H_2PO_4^-$ during activation. ***Hypothesis 3:*** The model, run with new parameters, will predict age-related fatigue resistance during intermittent, maximum isometric contractions within one standard deviation of experimental values for older men.

If the preceding hypotheses are supported, it will afford the opportunity to gain significant insight to the mechanisms of age-related fatigue resistance. While the precise mechanisms of fatigue during repeated isometric contractions are debated, the most prominent features of current theories will be represented in the proposed model. Confirmation that the model predicts voluntary generation of torque will be provided by Hypothesis 1. If Hypothesis 2 is supported, it will improve our confidence that the model is sensitive to pertinent aspects of neuromuscular function involved in fatigue. Finally, accurate prediction of age-related fatigue resistance through modification of those parameters involved in voluntary force production will permit testing of additional hypotheses that are impossible using more traditional in vivo or in vitro experimental techniques.

Sensitivity analyses can be performed to identify those parameters that have the greatest impact on force production and fatigue. Further, individual parameters might be modified to reflect changes in neural (97) or muscular (57) function with training. Insight gained from these modifications might provide the basis for training modalities whose effectiveness could be tested using in vivo experimentation.

Significance

Mathematical models of skeletal muscle function were first described in the 1950s by the work of A.V. Hill (82) and Hugh Huxley (90). Since then, computational models have been proposed to explain the physiological behavior of skeletal muscle perfusion, neuromuscular activation and even fatigue during repeated activations. However, a comprehensive model that allows simultaneous inquiry of multiple sites in the pathway of force production has not been developed, nor has such a model been used to address questions related to the effects of old age.

The complicated etiology of age-related fatigue resistance is likely due to several differences in neuromuscular function between younger and older adults. The relative impact of each of these changes is hard to quantify, as their influence cannot be separated in the intact organism. Computational modeling affords the opportunity to independently modify each of these components to better understand their respective impact on age-related fatigue resistance. Doing so allows one to test hypotheses related to age-related changes in neuromuscular function that would be impossible using in vitro or in vivo experimental techniques.

CHAPTER 2

LITERATURE REVIEW

<u>**Introduction**</u>

Age-related declines in muscle force and power generating capacity have been reported frequently in the literature (9; 55; 56; 164). These reductions in force and power have been implicated in diminished athletic performance for the most capable individuals (47), and severe mobility disability in frail elders (65; 66). Other deleterious age-related changes in neuromuscular physiology, such as reduced maximal motor unit discharge rates and smaller muscle size (30; 98; 176) are frequently, although not always, cited in the literature. In contrast, fatigue resistance has been reported under a variety of conditions to remain unchanged or even improve with old age (21; 25; 44; 106; 111; 112; 140; 160). In fact, when fatigue is induced by prolonged or repeated isometric contractions, a majority of the literature supports the notion of age-related fatigue resistance (87; 88), although there are exceptions (34).

While age-related fatigue resistance has been examined in great detail, few studies have provided an adequate explanation for this phenomenon. This is understandable, as variations in neuromuscular function between young and older adults occur at multiple sites and likely interact with the fatigue process in myriad ways. Because neuromuscular changes with age are difficult to identify independently with in vivo human experimentation, computational modeling is a promising means of parsing their relative influence on fatigue.

Computational methodologies have their roots in studies of muscular kinetics and mechanics performed over 60 years ago (82). The relatively recent expansion of

accessible computing power has greatly increased their utility in the last 20 years. However, computational modeling has not been used to address the age-related changes in fatigue resistance, despite the existence of several validated models that characterize either muscle fatigue (62; 63; 74; 118; 120; 171) or aspects of the aging neuromuscular system (175; 185).

The recent validation of models shown to predict age-related changes in the neuromuscular system (175; 185) combined with existing models of muscle fatigue (63; 118; 190) present an opportunity to apply computational modeling to the question of age-related fatigue resistance. While a combined synthesis of existing models would contribute to our understanding of the mechanisms of age-related fatigue resistance, greater insight can be gained with the addition of components that reflect the current state of knowledge regarding age-related changes to neuromuscular physiology.

This literature review will focus on the proposed mechanisms of skeletal muscle fatigue, the age-related physiological alterations thought to mediate fatigue resistance in older adults, and the computational characterization of muscular and neural systems. Because this proposal focuses on simulating neuromuscular function at the macroscopic level, particular attention will be paid to studies that have characterized the net behavior of entire muscles or muscle groups using phenomenological models. While the literature provides many excellent examples of mechanistic models that accurately predict contractile dynamics and neural behavior at the microscopic level, a significant review of their substantial contribution is beyond the scope of this dissertation.

Mechanisms of Skeletal Muscle Fatigue

The mechanisms of fatigue are complicated (48; 186) and likely task-specific

(86). Our understanding of the fatigue process has benefited from years of in vivo and in

vitro experimentation, during which, numerous insights into both cellular and systemic

influences on force generating capacity have been attained. However, both in vitro and in

vivo (indeed all) methodologies have some inherent limitations. In vivo experiments are

typically challenged by a lack of control over interrelated processes that may be difficult

to measure. In vitro experimental conditions, while more tightly controlled, cannot

usually mimic the complexity of in vivo systems. In either case, the ability of researchers

to quantify the relative contribution of multiple mechanisms to overall fatigue is

somewhat compromised.

Central Mechanisms

The proposed mechanisms of fatigue can be referred to as either central, or

peripheral in nature. The term, "central fatigue" is used to describe a range of neural

responses to contraction that ultimately reduce the ability to voluntarily excite skeletal

muscle (173). Central fatigue may result from reduced excitability and/or increased

inhibition at the level of the motor cortex, or motor neurons (1 and 2 in Figure 1). It is

likely that both mechanisms contribute to fatigue during maximal contractions (173).

Reduced excitation of α motor neurons manifests in reduced maximal discharge rates for

active motor units, and/or derecruitment of motor units, beginning with those with the

highest activation thresholds (98). Signals from group III and IV afferent nerve fibers

likely play a role in diminished cortical excitability, as well as increased α motor neuron

inhibition (18; 172). Central mechanisms of fatigue seem to play the greatest role during

prolonged, sub maximal isometric contractions (191) and a lesser role during intermittent

maximal contractions (20; 112; 125). Central mechanisms likely contribute to some

degree in most situations involving skeletal muscle fatigue. However, under most

conditions, the magnitude of their effect is small compared with peripheral mechanisms.

Peripheral Mechanisms

Peripheral fatigue mechanisms refer to events occurring distal to the nervous

system (3 and 4 in Figure 1). These include reduced excitability of the sarcolemma (51;

61) and decreased sensitivity of troponin to Ca^{2+} (33; 50). Increased extracellular

potassium is thought to mediate differences in sarcolemmal excitability (142), while

changes in intracellular metabolite concentrations influence intracellular mechanisms for

peripheral fatigue. Repeated contractions of sufficient intensity will increase intracellular

[ADP], [Pi] and [H^+] which have been implicated in fatigue processes (106). Through
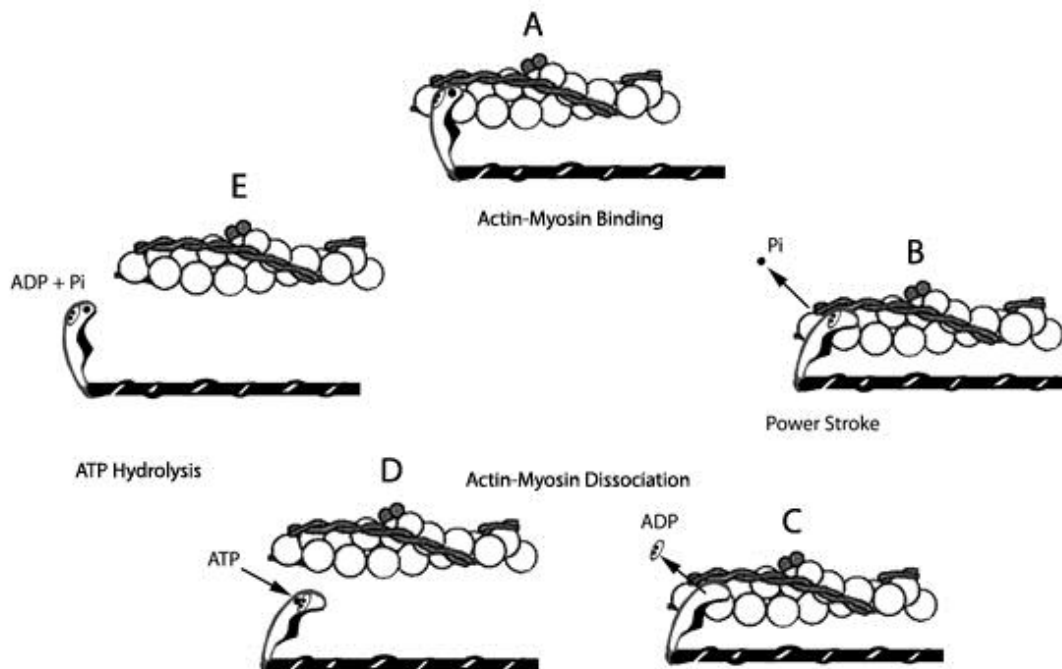
Figure 2.2 Cross Bridge Cycling: Steps in the interactions between actin, myosin, and ATP that
result in force generation and shortening of the myofiliment.

11

multiple mechanisms, each of these metabolites alter the behavior of cross-bridge binding. Their combined effect ultimately lowers force and rates of relaxation (49).

The intracellular environment is thought to mediate loss of force-generating capacity through two primary mechanisms: decreased force generated per cross-bridge and decreased number of strongly bound myosin on actin at any given instant during activation (132; 133). The chemical steps involved in actin-myosin interaction and subsequent force generation are illustrated in Figure 2. The influence of increased [Pi], [H$^+$] and [ADP] on these steps are likely different (49) and recent evidence suggests, highly dependent on temperature (36).

During activation, force generation depends on binding of the acto-myosin complex in its strongly bound configuration (Figure 2, A) and dissociation of Pi from this complex (Figure 2, B). Because these reactions occur in equilibrium within the sarcoplasm, and steps are reversible, increased cytoplasmic [Pi] may decrease its rate of dissociation from the acto-myosin complex, and thus, reduce force generation (Figure 2, B). Significantly, the effects of increased [Pi] and [H$^+$] are additive, suggesting alternate mechanisms (31; 143).

Repeated contractions result in increases in cytoplasmic [ADP] which likely slows dissociation of ADP from the acto-myosin complex (Figure 2, C). This step precedes binding of ATP to the acto-myosin complex, and subsequent dissociation of actin and myosin (Figure 2, D). As a result, increases in [ADP] likely play a role in slowed rates of cross-bridge cycling and reduced contraction velocity.

It could be postulated that increased [ADP] will tend to increase the number of bound cross bridges by reducing the rate of dissociation of myosin from actin (Figure 2,

C). However, these events are accompanied by a reduced Ca^{2+} sensitivity and reduced force per cross bridge, which seem to influence force to a greater extent than [ADP]. It appears that increased [ADP] in vivo tends to have the greatest effects on prolonged rates of force relaxation. Elevated $[H^+]$ depresses cross-bridge force in vitro, regardless of saturating levels of Ca^{2+} (132), suggesting it has independent effects on cross-bridge force generating capacity (46).

The effects of metabolite concentrations on fatigue also vary by muscle fiber-type. At temperatures close to the human physiological range (~30° C), the depressive effects of acidosis on force output are similar between slow, type I fibers and fast, type IIa fibers, but greater in type IIb (133). Similarly, the depressive effects of increased [Pi] on force production are more pronounced in type II fibers than type I (36), but only at lower temperatures. Significantly, the effects of increased [Pi] and $[H^+]$ are additive, suggesting alternate mechanisms (31; 143).

Since the mid 1970s, when its use as a tool for in vivo study of muscle physiology was pioneered (7; 17; 84), ^{31}P magnetic resonance spectroscopy (MRS) has provided significant insight into the metabolic perturbations associated with repeated contractions. By tracking the relative concentrations of phosphorus containing metabolites within contractile tissue during fatiguing contractions and subsequent recovery, investigators have been able to associate changes in these metabolites with fatigue. Repeated or prolonged contractions increase rates of glycolysis, which produces excess H^+, in addition to ATP and pyruvate. Some investigators have observed an inverse, linear relationship between $[H^+]$ and force-generating capacity (106). However, during recovery from fatigue, hysteresis is evident in this relationship, indicating that if $[H^+]$ is

directly mediating fatigue, its relationship with force-generating capacity is not constant.

It seems likely that [H^+] has an associative, rather than causal relationship with reduced

force production in vivo. This finding is in apparent conflict with results from in vitro

experimentation that dictate a strong relationship between fatigue and cellular acidosis.

However, it is important to note differences between in vitro and in vivo observations of

muscle fatigue. Several sites of force loss including sarcolemmal excitability and

reduced motor unit activation and discharge rate may be present during voluntary

activation, but lost during in vitro study. Further, human spectroscopy data represent a

signal acquired from relatively large volumes of tissue with likely heterogeneous

metabolic and fatigue characteristics. In contrast, in vitro studies typically draw from

more homogeneous samples.

Several investigators have observed associations between [$H_2PO_4^-$] and skeletal

muscle fatigue (31; 103; 106; 111; 113; 135) which seem more robust than associations

between [H^+] and fatigue alone.

Increased [$H_2PO_4^-$] during contraction

reflects increased intracellular [Pi]

and [H^+] that result from the creatine

kinase reaction and glycolysis

respectively. Multiple studies have

demonstrated a linear association

between [$H_2PO_4^-$] and fatigue (31;

106; 111; 113; 135). The correlation

between fatigue and [$H_2PO_4^-$] persists
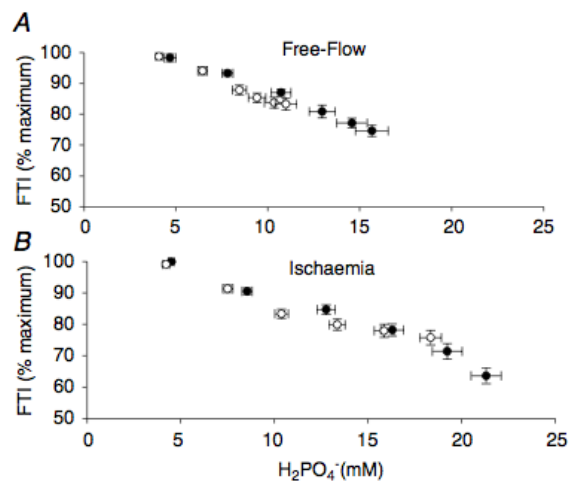
Figure 2.3 Reproduction from Lanza et al (Figure 5 (111)). Linear relationship between fatigue and [$H_2PO_4^-$] in old and young men and women during free flow (A) and ischemic (B) conditions.

14

across age groups during ischemia (Figure 3; (111)) and is consistent, whether fatigue is induced by intermittent or sustained contractions (135).

It has been suggested that the strong relationship between fatigue and [H2PO4$^-$] is lost during repeated bouts of dynamic contractions (156). In light of this observation, and given the myriad influences on voluntary force-generating capacity, it seems unlikely the entirety of the fatigue process can be ascribed to a single metabolite. However, the variety of conditions under which [$H_2PO_4^-$] correlates with losses in force highlights its utility as a strong predictor of fatigue during isometric contractions.

Age-Related Fatigue Resistance

Age-related fatigue resistance has been reported by a number of labs under a variety of experimental conditions (20; 21; 25; 44) while others have reported the opposite (10; 149). A trend in the literature suggests that age-related fatigue resistance is reported least often during dynamic contractions (112). On the other hand, age-related fatigue resistance is reported frequently during repeated isometric contractions (25; 44) and most frequently during sustained maximal and sub maximal endurance tasks (11; 88; 125). Several mechanisms have been proposed to explain age-related fatigue resistance, including greater reliance on oxidative metabolism (106), increased metabolic economy (80; 111) and reduced generation of fatigue-inducing metabolites (23; 26).

Several studies have investigated the potential role of central activation in mediating age-related fatigue resistance, but with a few exceptions (168) most investigators have found little evidence for a role of activation in this phenomenon (3; 25; 108; 112; 125). However, altered recruitment strategies have been suggested as potential mechanisms in age-related fatigue resistance. Older adults have lower maximal motor

unit discharge rates than young during non-fatigued maximal contractions (96; 147; 160).

However, these lower discharge rates are observed with slower rates of force

development and relaxation (160), potentially explaining a similar capacity for voluntary

activation.

Rubinstein and Kamen (160) showed that maximal motor unit discharge rates and

relative force declined to a greater extent in young adults than in older adults during 30-

second, intermittent isometric contractions. Age-related reductions in non-fatigued

contractile kinetics and motor unit discharge rates may impact fatigue resistance by

reducing the overall metabolic cost of contraction. Maintenance of membrane

polarization and re-uptake of Ca^{2+} following each depolarization event represents a

significant (between 20% and 80%; (182; 193)) portion of the overall metabolic cost of

contraction. Reducing the number of depolarization events necessary to fully activate a

given muscle may therefore reduce the overall metabolic cost of force maintenance. In

fact, reduced ATP per unit force production (metabolic economy) has been associated

with fatigue resistance (167). However, Russ and colleagues did not observe a

relationship between stimulation frequency and metabolic cost when using multiple,

supra-physiological electrical stimulation frequencies (161).

Under most conditions, intracellular [ATP] is maintained during contraction

despite the dramatic increase in ATP use. Synthesis of ATP occurs via PCr hydrolysis,

glycolysis, and oxidative phosphorylation. In vitro observations reveal a strong

correlation between oxidative function and mitochondrial density with fatigue resistance

(169; 180). Further, both exercise and low frequency electrical stimulation have been

shown to promote greater oxidative capacity in target muscles, which correlates with

increased fatigue resistance (52; 93; 122). Oxidative phosphorylation is a more fatigue-resistant metabolic pathway because substrate availability is not limiting in most conditions, as opposed to PCr hydrolysis, and its byproducts do not promote loss of force generation as is the case with glycolysis.

While some studies show reduced capacity for oxidative phosphorylation with old age (29; 165), others show a similar or even improved capacity in older adults (16; 26; 106; 111; 154). In vivo oxidative capacity is likely muscle-specific and at least partially dependent on habitual physical activity (64; 85; 114). These observations prohibit broad generalization about age-related changes in muscle oxidative capacity. However, recent evidence strongly suggests that intracellular metabolism plays a role in mediating age-related fatigue resistance during isometric contractions (106; 111). In these studies, a relatively greater relative reliance on oxidative phosphorylation and reduced accumulation of $[H^+]$ and $[H_2PO_4^-]$ were associated with improved fatigue resistance in the old, despite similar relative force production.

It is important to point out that the metabolic properties of muscle fibers and the characteristics of the motor units that innervate them are related. Evidence in the human and animal literature has shown that motor units with low activation thresholds and lower maximal discharge rates tend to innervate muscle fibers that express the type I myosin heavy chain (MHC) isoform. These muscle fibers tend to have relatively slow contractile characteristics and a greater number of mitochondria than muscle fibers expressing type II MHC isoforms. On the other hand, higher threshold motor units with faster maximal discharge rates tend to innervate muscle fibers expressing the type II MHC isoforms. These fibers have fast contractile characteristics, relatively few mitochondria, and rely

17

primarily on glycolytic metabolism to produce ATP. Fibers expressing type II MHC can be further sub-divided into types a and b (sometimes referred to as "x") in humans (71). In general, type IIb fibers have the fastest contractile kinetics, and rely most on anaerobic, glycolytic metabolism while type IIa fibers are intermediate between type I and IIb in terms of contractile and metabolic characteristics (71). The relationship between motor unit properties and fiber type has been demonstrated by surgical reversal of the innervation of two muscles with opposite fiber type compositions (predominantly type I or type II) in multiple animal studies (8; 68; 163).

A progressive loss of high threshold motor neurons has been proposed to occur with age (115). It is thought that some of the fibers, "orphaned" by the loss of innervation, are "adopted" by the axons of neighboring motor neurons. Thus, the surviving motor units are likely to have lower recruitment thresholds and maximal discharge rates. Subsequently, these fibers take on characteristics to match the motor neurons innervating them. This process leads to a gradual redistribution of fiber-type within the aging neuromuscular system. The theory of fiber-type redistribution is supported by a tendency for greater "grouping" of like muscle fibers in animals (6) and a greater proportion of type I fibers in most muscle groups of older adults compared with young (92; 119). It is possible that the combined effect of lower maximal discharge rates and a greater proportion of slow, type I muscle fibers contribute to age-related fatigue resistance.

While most studies have focused on peripheral mechanisms to explain age-related fatigue resistance, questions remain regarding the mechanisms of this phenomenon. The

interrelated nature of neural activation, contractile properties, and metabolic response make if difficult to identify a single mechanism for age-related fatigue resistance.

Computational Modeling

When direct measurement proves exceedingly difficult, computational modeling has been applied to reveal the mechanisms of physiological systems. It was not long after material engineers began describing the visco-elastic properties of building materials that these models were applied to biological tissues. Muscle was a particularly interesting tissue to model due to its ability to actively shorten, while simultaneously exhibiting passive spring-like and damping properties. As computing power grew along

Figure 4. Representative Hill-type muscle model. Contractile component (CC), Series elastic component (SEC), Parallel elastic component (PEC) and pennation angle (θ). (L) indicates length of the respective component

with an increased ability to characterize various aspects of physiological function, modeling became a more prominent research tool.

Modeling Contractile Dynamics and Force Generation

The pioneering work of A.V. Hill (81) was among the first to mathematically characterize the kinetics of skeletal muscle force development. His mathematical model includes several rheological elements meant to represent characteristics of contracting skeletal muscle. These typically include a contractile component (CC), capable of active shortening, a series elastic component (SEC), with non-linear spring constant characteristics in line with the CC, and a parallel elastic component (PEC) sensitive to overall changes in the combined length of the SEC and CC.

These elements are typically arranged as in Figure 4. The angle θ represents the pennation angle of fascicles, or bundles of fibers. While not strict analogues to physical structures, the combined behavior of the CC, SEC, and PEC mimic that of the observed contractile dynamics in intact skeletal muscle. While the overall behavior of the Hill model matches well with the contractile properties of whole muscle, no single component of the model is meant to represent the physiological function of individual components of actual muscle tissue. For example, the PEC in the Hill model captures the elasticity not only of structures within whole muscle such as the epimycium, but also the compliance of myosin heads during cross-bridge formation. Unless these components share identical force-length characteristics, a classic Hill model is limited in its ability to independently describe them. The strength of the Hill model however is its general accuracy, computational efficiency and reliance on relatively few assumptions. This combination of attributes makes the Hill-type model a desirable tool for predicting muscle force during musculo-skeletal simulations.

It was not until Hanson and Huxley proposed the organizational structure of skeletal muscle fibers (70) in 1953 and Huxley formalized the sliding filament theory (90) in 1957 that accurate mechanistic models could be developed. These studies were the first to accurately describe the periodic, interdigitated structure of the sarcomere as it is currently understood. Further evidence of cross-bridge formation between actin and myosin filaments (91) made it possible for scientists to understand the direct molecular mechanisms responsible for force generation in skeletal muscle. These discoveries allowed for muscle models whose components would represent specific physical structures. These models predict force by directly modeling the probabilistic interaction

of actin and myosin during excitation events. Several investigations followed Huxley's initial work to refine the understanding of skeletal muscle function. Notably, Lymn and Taylor described a kinetic model of ATP hydrolysis by actomyosin (123), which agreed with Huxley's proposed sliding filament theory and dramatically improved our understanding of the biochemical processes involved in skeletal muscle contraction.

Huxley-type models characterize force using multiple, partial differential equations. Force is predicted based on functions representing binding and un-binding rate parameters for actin-myosin interactions. Their rates of attachment and detachment are products of probability functions related to contractile velocity and the distance from the equilibrium position of the cross bridge. Terms may also be included to characterize the effect of various metabolite concentrations on actin-myosin interactions (146). The effect of contractile velocity and metabolite concentration are implicit in Huxley model formulations, which facilitates their use in testing hypotheses related to cross-bridge cycling and force production at the level of the sarcomere.

However, Huxley-type models depend on muscle length and do not consider elasticity, which limits the ability to scale the predictions they generate to whole muscle behavior. In addition, the multiple, partial differential equations used to derive force in the Huxley-model approach are far more computationally-demanding than the ordinary differential equations in a Hill-type model. A model of whole muscle forces would likely require many models, running simultaneously, to represent the range of characteristics present in a heterogeneous population of muscle fibers. This consideration is not trivial and further limits scalability.

Clearly, the Hill and Huxley approaches to muscle modeling differ greatly and neither can be universally applied. Researchers construct a model that best fits the questions they seek to answer. As such, most computational models of muscle function can be described as either phenomenological (Hill-type) or mechanistic (Huxley-type), although models exist that attempt to capture the physiological relevance of the Huxley-type model with ordinary differential equations (192).

An interesting attempt at merging the physiological accuracy of the Huxley model with the relative computational simplicity of the Hill model was proposed by Zahalak in 1981. His compromise was a "distribution moment" model that retained key features of the Huxley model, but used a set of three ordinary differential equations. The infrequent use of the distribution moment approach may be due to improvements in the capacity of personal computers in the 1980s and early 1990s, which minimized the need for mathematical simplifications.

Models of similar "type" can vary greatly in terms of their complexity. A more complicated model potentially allows the investigator to gain greater insight into the system represented by the model. However, the more components used to make the model, the more opportunity for assumptions to be incorrect, thereby reducing any insight gained by their collective behavior. Practical considerations of computational efficiency and scalability will also directly affect a model's utility, and will change from one application to another (189).

Typically, model systems begin with simple versions that rely on relatively few assumptions. If the outcome predicted by these models match well with experimental data, they may then grow in complexity, incorporating greater detail and more

assumptions as knowledge of a given system increases. It is assumed that model

expansion would rely on data from direct observation. Natural evolution of model

complexity is not always so straightforward. Hill muscle models, which typically consist

of ordinary differential equations, and Huxley-based models consisting of partial

differential equations do not lend themselves well to an evolutionary progression from

one to the other. Rather, the demands of the required application typically determines

which model is used.

The greatest detail of contractile behavior can be gleaned from Huxley-type

models, but it is exceedingly difficult to apply them to systems incorporating multiple

systems (e.g. bone, tendon, body segments). Hill-type models, on the other hand, predict

behavior of these systems but reveal less about their underlying mechanisms. While a

mechanistic approach to muscle modeling may yield greater information on the

influences of contractile kinetics at the microscopic level, phenomenological models are

more appropriate for many applications. For example, forward dynamics simulations of

human movement, which depend on computationally-efficient and accurate prediction of

force, use Hill-type models almost exclusively.

Many early models characterizing the viscous and elastic properties of muscle-

tendon units were phenomenological (95; 158; 188). An early mechanistic approach

came from Pell and Stanfield (148). They distinguished their model from more

phenomenological approaches by focusing on a microscopic basis for the model's

mathematical functions . Specifically, they developed a model of the sarcomere based on

predicted behavior of known physiological structures. By modeling the interdigitation of

actin and myosin they incorporated force-length relationships in their model without

explicit force-length terms. However, viscous dampening, in this case attributed to resistance to the flow of sarcoplasm over myofiliments during contraction, was modeled by a dashpot similar to phenomenological models. This serves as an example, repeated throughout the literature, of nomenclature playing a large role in the definition of a model as either mechanistic of phenomenological.

Computational models of muscle force are more relevant if their force output can be compared with experimental joint torque (107). Riener et al (157) used a phenomenological model to predict muscle force, which was then used to predict knee extensor kinematics in response to electrical stimulation. Umberger et al (177) used a Hill-type muscle model originally proposed by van Soest and Bobert (181) to predict energy liberation through heat and work during activation. The model was refined to derive most parameter values from mammalian data in the literature. The flexibility and ultimate utility of Umberger's refined van Soest model was demonstrated by its incorporation into musculoskeletal models of varying complexity (isolated muscle, single joint actuation, whole body movement).

Thelen et al (175) used a Hill-based muscle model to accurately model forces produced during dynamic contractions. Their model accurately predicted forces produced at various joint positions and velocities in the ankle dorsiflexor/plantar flexors. Perhaps their most significant contribution however was the accurate prediction of alterations in torque generation when they adjusted their model to predict the effect of age. Specific properties reflecting the deactivation time constant, maximum shortening velocity, passive muscle strain and the ratio of lengthening force to isometric force were modified in an effort to reflect changes in muscle function with age. Comparing their

predicted force with experimentally-derived values confirmed the accuracy of the model. These are a few of many examples demonstrating the utility of the Hill model as a component in multi-faceted, computationally-demanding simulations.

Modeling Neural Activation

While Hill and Huxley largely explained contractile dynamics, modern understanding of voluntary neural function is due primarily to the work of Henneman (78; 79). The concept of ordered recruitment for motor units was first proposed in 1957, and has formed the basis of several models used to investigate neural behavior (78). Henneman's studies described an ordered recruitment of motor neurons such that stimulation threshold correlated with neuron size. Smaller motor neurons, which tend to have slower conduction velocities and innervate fewer muscle fibers, were recruited before larger motor neurons, which tend to have faster conduction velocities and innervate a greater number of fibers.

Given the range of forces generated by different motor units, not to mention their varied rates of force development, the order in which motor units are recruited is an important consideration when modeling voluntary activation. Cogshall and Bekey (28) offered an early example of physiological activation with a stochastic model of motor unit recruitment. To this point, most models used deterministic functions predicting activation in response electrical stimulation, or simply assumed complete and simultaneous activation. In the case of supra-maximal electrical stimulation of the motor nerve, it can be assumed that all motor units are activated maximally and simultaneously. Therefore, model inputs do not consider recruitment strategy (motor unit recruitment order and rate coding). During voluntary activation however, motor unit recruitment is

more stochastic; it follows an ordered recruitment pattern, but with a probabilistic time course. Cogshall and Bekey constructed an aggregate model of motor unit recruitment that featured correlates to physiological motor control, including motor unit recruitment and rate coding. Force was modeled as the linear sum of all active motor units and motor units were activated following a poisson distribution. Contractile dynamics of these motor units, once activated, were characterized by motor unit type (high or low threshold) and a probability distribution determined their respective contribution to total force. The shape of their wave forms were based on experimentally-derived values, but did not include explicit physiological components.

A series of papers, published between 1991 and 1997, significantly advanced the field of neuromuscular modeling (58; 59; 77). The model formulation providing the basis for these publications focused on predicted recruitment of a physiologically representative sample of motor units. Their modeled output, however, extended to muscle force. This series began with the work of Heckman and Binder (77) and was continued by Fuglevand et al (59). Although the limited detail of their force model could be seen as a limitation, their model contributed significantly to the understanding of the mechanisms and utility of physiological recruitment patterns during progressive activation (58). Heckman and Binder modeled a population of motor units with a range of recruitment thresholds. Their model was limited by its reliance on several assumptions. First, the effective synaptic current to motor neurons was assumed to sum linearly and distribute uniformly across the motor neuron pool. Second, firing rate was assumed to increase linearly with effective synaptic current, a presumption that has since

been questioned (150). Nevertheless, this approach made a significant contribution to the field by proposing and validating a model of physiological motor unit recruitment.

Fuglevand et al (59) extended this simulation by adding components representing conduction of the action potential through multiple tissues and their summation at the surface of the skin. This feature added a further means of confirming model output by comparison to measured surface electromyogram (EMG). Additional model formulations, also led by Fuglevand, used their previous model to simulate the effect of spatial distribution and ordered recruitment of motor units to perfusion in the microcirculation (58). A forward dynamics approach, as opposed to simple algebraic expressions, was used to arrive at muscle force in both of these simulations. While each model motor unit had unique force-generating characteristics according to recruitment order and duration, contractile modeling was simplified, and did not consider elastic components or contractile history.

Hawkins and Hull (75) combined models of neural activation and muscle force to predict the output of voluntary activation. Experimentally-measured EMG was used to determine an activation coefficient for a model of muscle composition, architecture and force (75). "Fiber pools" available for recruitment were designated as either slow oxidative, fast oxidative, or fast glycolytic. These pools were defined by unique force and activation characteristics. While this model lacked the mechanistic approach to motor unit activation and firing rate behavior pioneered by Heckman et al, it provided more detailed information on the force response.

Modeling Muscle Fatigue

Time-sensitive models that predict the effect of repeated contractions have significantly expanded the utility of more traditional muscle models. One of the earliest mathematical representations of work capacity is from Rohmert, published in 1960 (159). It is only in the last two decades however that computational models have emerged that take into account muscle characteristics of work capacity, fatigue and recovery. Earlier attempts at modeling fatigue were directed at assessing occupational work capacity by predicting the expected number of repetitions one could perform for a given task.

One of the earliest attempts to predict fatigue at a single joint using a valid muscle model came from Hawkins and Hull (74). They adapted a previously validated model of muscle force generation (75) to predict fatigue with prolonged, consistent activation. Their model included separate functions for fatigue and endurance characteristics that were specific to three muscle "types" (fast oxidative, slow oxidative and fast glycolytic). Endurance was characterized as the predicted time a muscle could be activated before force would begin to decline. Fatigue was the linear decline in force that resulted from activation that exceeded endurance time. Model activation was based on a similar strategy employed in this groups work from 1992 (75), where EMG dictated activation of modeled fibers in a manner meant to represent physiological recruitment order. Experimental data from the diaphragm muscle (12) was used as the foundation for the relationship between endurance time, duty cycle and force output that characterized oxidative muscle types (fast and slow). Endurance time for the fast glycolytic type was based on the amount of glycogen stored in the muscle. The rate of force decline was linear after endurance time was reached and was unique for each fiber group. Despite its

rather simple composition and gross assumptions, their model successfully predicted the rate and total amount of fatigue during 60 seconds of maximal elbow extension. This significant contribution was one of the first computational models to predict voluntary fatigue and is augmented by their consideration of both activation (EMG control signal) and the differential response of multiple fiber-types (recruitment order, endurance time and fatigue rate).

Since Hawkins et al, (74) significant advances have been made in modeling the fatigue response. Most models of fatigue derive their parameters from studies of paralyzed, electrically stimulated human muscle. Because a common aim for these studies is discovery of optimal stimulation strategies for use during functional electrical stimulation (FES), voluntary activation is typically ignored. Several groups, most notably Binder-Macleod and colleagues, have devoted considerable effort to these models (40; 43).

After validating a muscle model that could predict force output in response to multiple trains of electrical stimulation (41), several new parameters were added to model declines in force with repeated stimulation (42). Although others had associated EMG with fatigue during FES (62), and declines in peak torque during FES had been characterized (153), few had proposed a model based on physiological data that could predict fatigue *a priori* during FES (62; 63; 118). The strongest feature of Ding et al's 2000 model was its flexibility. The model accurately predicted force output in response to stimulations of various frequencies and durations. This greatly enhanced the applicability of this model to FES and improved the state of modeling literature as previous models were capable only of predicting fatigue resulting from simulation

protocols similar to those used to parameterize the model. Their 2002 model (43) also accounted for variable rest periods, allowing the model to appropriately respond to changes in duty cycle.

While Ding et al, (43) used EMG as the primary source of physiological input, others have used metabolite concentration as a limiting function on force-generating capacity. This latter approach attempts to mimic the fatigue process in a way that is perhaps more representative of in vivo skeletal muscle function (62; 63; 118). Giat et al (62) were one of the first to incorporate metabolic by-products of activation in a model of muscle fatigue. Using ^{31}P MRS to measure $[H^+]$ during stimulation, they correlated decreasing pH with force loss and included it as a function of the model (62). These efforts were extended in 1996 when a recovery function was added to this model, allowing for the accurate prediction of muscle force in response to FES with varying periods of rest (63). This was one of the first models designed to not only accurately predict fatigue, but also the recovery of force-generating capacity.

Levin and Mizrahi (118) published an even more comprehensive model which used both recorded EMG and metabolic status of the muscle ($[H^+]$ and $[H_2PO_4^-]$) to predict fatigue and recovery in electrically-stimulated quadriceps muscle. Previous work had established a preliminary model of fatigue based on altered concentrations of phosphorus-containing metabolites, pH and force generating capacity (137). However, EMG was included in this model to better predict multiple bouts of fatiguing contractions. The behavior of their model seemed to suggest that metabolic factors (reflected by pH in the model) mediated fatigue acutely, while excitation-contraction

30

coupling failure (captured by EMG) during electrical stimulation dictated a more chronic loss in response to electrical stimulation.

Since these ground-breaking studies were published, others have expanded the scope of muscle fatigue modeling. Marion et al (128) recently advanced the models of Ding et al (40; 41) to predict fatigue during electrically stimulated dynamic contractions. Long term adaptation to training in terms of force and fatigue has been modeled by Gacesa et al (60), while Shorten et al, (166) have published one of the most comprehensive models to date investigating skeletal muscle fatigue in response to repeated stimulations. The mechanistic model by Shorten et al, (166) described muscle sarcolemma and t-tubule action potentials, Ca^{2+} release and cross bridge dynamics. Fatigue was modeled by linking [Pi] with both slowed cross bridge cycling and Ca^{2+} precipitation, thereby reducing the potential sites for strongly bound cross bridges and the forward rate constant for attachment. Others have taken an alternate approach and prioritized computational efficiency (190). The rapid advances in this area led to a range of validated models with myriad applications. Despite these advances, researchers have yet to create a model that predicts the disparate fatigue responses of healthy young and older adults. Such a model would permit the testing of hypotheses that would be impossible using in vivo or in vitro experimental methods.

Summary

The precise mechanisms of skeletal muscle fatigue are not well understood. Central mechanisms play a role in fatigue during voluntary contractions, although their role appears limited compared with peripheral mechanisms under most conditions. The byproducts of intracellular, metabolic processes that maintain [ATP] in the face of

changing energetic demands have been implicated in fatigue. While in vitro evidence suggest roles for several metabolites in the reduction of force-generating capacity, the extent to which these in vitro findings reflect the behavior of the intact neuromuscular system is not always clear. Data from in vivo studies finds inconsistent effects of metabolites such as H^+ and ADP. However, most in vivo studies support a strong association between $[H_2PO_4^-]$ and fatigue that persists under a variety of conditions. While there is logical support from in vitro experimentation for mechanisms by which $[H_2PO_4^-]$ may influence force generating capacity, a single, or even most prominent mechanism remains elusive.

Evidence in the literature strongly suggests that during both prolonged, and intermittent isometric contractions, older individuals tend to fatigue relatively less than their younger counterparts. While conclusions are mixed when dynamic contractions are used to induce fatigue, age-related fatigue resistance has been observed by multiple investigators testing fatigue in response to a variety of voluntary contraction protocols in multiple muscle groups (20; 21; 25; 88; 130). However, due to the many differences in neuromuscular function between young and older humans, it is difficult to ascertain the physiologic mechanisms of age-related fatigue resistance. Reduced maximal motor unit discharge rates, a relatively greater abundance of type I muscle fibers, and increased metabolic economy may all contribute to the phenomenon. A clear understanding of how each of these features of the aging neuromuscular system might contribute to fatigue resistance is difficult to determine in vivo.

Human skeletal muscle has been described mathematically in many applications using multiple methods. From intracellular events to the forces generated during

maximum jumping, computational modeling has emerged as an attractive means of combining what is known about isolated systems and what can be predicted about their combined behavior. Models have been developed that successfully predict the function of musculo-skeletal interactions, nervous tissue and even individual sarcomeres within skeletal muscle. Although models have been proposed that predict fatigue in response to repeated activation, and others have been designed to predict altered function with old age, no model has been designed to examine age-related changes of the neuromuscular system in the context of fatigue. Given the questions that remain regarding the phenomenon of age-related fatigue resistance, we are presented with a great opportunity to apply existing methods to a computational model that might predict the relative influence of age-related changes to neuromuscular function on the ability to resist fatigue.

CHAPTER 3

METHODS

Experimental Design

A combination of published model formulations and experimentally-derived functions will be used to construct a multi-component computational model of neuromuscular function. Matlab software (MathWorks, Natick MA; Matlab 7.0 with appropriate toolboxes) will be used throughout for model formulation and testing. The components responsible for predicting motor unit recruitment, calcium release and reuptake, force generation, and subsequent torque values will be combined to predict maximal voluntary ankle dorsiflexion torque in healthy young and older men.

Initial validation will be attempted by comparing the modeled torque response to 5 seconds of maximal activation with the maximal torque production during a 5-second
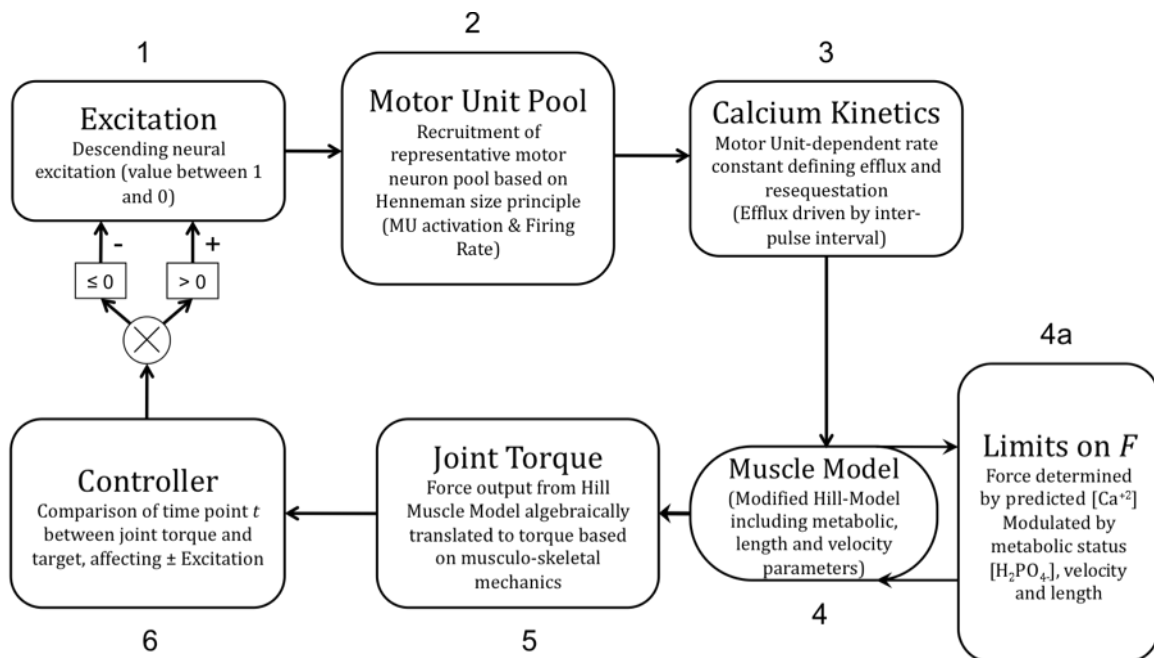
Figure 3. 5 Computational model scheme. The model will be run using a forward integration routine to calculate each model step (1-6) at each time point for the duration of the simulation.

maximal voluntary isometric contraction MVIC in healthy young men (Hypothesis 1).

The model will then be modified to account for the production of $H_2PO_4^-$ and subsequent

fatigue associated with repeated activations (Hypothesis 2). This additional component

will be tested by comparing the relative decline in modeled force output during 6

repeated, 12-second contractions with data from an identical protocol performed by

healthy young men (111). Finally, metabolic, motor unit, and contractile parameters will

be adjusted to reflect reported differences in the aged neuromuscular system. The

adjusted model will again be tested for its ability to predict the relative decline in force

output during six, 12-second MVICs (Hypothesis 3) by comparing the modeled

simulation to literature values of healthy older men performing the same task (111).

Each component of the proposed model will be derived from existing

computational models, listed in the following section. In most cases these components

will be parameterized using data from the literature. However, the musculoskeletal and

metabolic cost portions of the model will draw from an available dataset (See Source

Data, below).

Computational Model

Overview

The proposed model will follow the general scheme outlined in Figure 5.

Because the model will incorporate the output from multiple components meant to

represent stages in the pathway to force production, they will be introduced (and

computed in the forward dynamics simulation) sequentially.

Briefly, a single parameter meant to represent voluntary excitation (E, Step 1) to

the spinal cord will initiate the forward dynamics model by serving as the input for a

modeled pool of motor units (step 2). If activated, modeled motor unit output will drive the model of calcium kinetics (step 3). Modeled calcium concentration will be normalized and input to a Hill-type model of force production (step 4). The linear sum of the muscle model's force will comprise part of a musculo-skeletal model to predict a resultant joint torque (JT) at the ankle (step 5). Finally, comparison between a target torque (T_t) and T_c (step 6) will cause an adjustment of E such that the difference between JT and MT is minimized. The next time step will be associated with a new T_t, and the procedure will repeat for the duration of the simulation. An advantage of this control structure, as opposed to binary control (0 or 1), is the ability to model sub maximal activations. In the case of repeated sub-maximal activation, modeled fatigue may be characterized by an increase in E to achieve the same target torque, or a failure to achieve target torque despite maximal E.

Step 1. Excitation

The initial step for the model represents excitation which begins at the motor cortex and descends through corticospinal tracts to α motor neurons in the spinal cord. Input from the central nervous system to pools of α motor neurons is physiologically complex and dictates many aspects of coordinated, voluntary muscle activation. However, several studies suggest that central mechanisms do not play a critical role in age-related differences in fatigue (88; 125). Because of its complicated nature and incomplete definition in the literature, no attempt is made for the computation of E to reflect physical events in the process of motor unit excitation.

Step 2. Motor Unit Pool

Modeling of the motor unit pool will closely follow procedures described by Fuglevand et al, (59). A pool of 120 individual motor units (single units responsible for the activation of populations of contractile function models, MU) will be activated in an orderly fashion in response to E. The recruitment threshold (RT) for various MUs will be distributed such that many MUs have low RT while relatively few have high RT. This approach can be described mathematically by the function:

$$RT(i) = e^{a*i} \qquad\qquad (1)$$

Where i is an index indicating MU number, and a is the coefficient indicating a range of threshold values. Broad variation in recruitment thresholds has been observed experimentally (178) and will be reflected in the model. Similar to Fuglevand et al (59), the range of RT values will be 30-fold. Once activated, MU(i) will have a minimum firing rate (MFR) of 8 Hz (30; 178). Although it is possible that MFR could vary between motor units in direct proportion to RT (67), empirical studies performed in humans during voluntary contractions suggest MFR is constant across MUs (35; 136).

Once the threshold for excitation has been surpassed for a given motor unit, a single linear function will describe the relationship between excitation and motor unit firing rate. The relationship between increased E and increasing FR will be similar for all modeled MUs. Mathematically, this will follow the form:

$$FR(i) = g*[E(i) - RT(i)] + MFR(i) \qquad\qquad (2)$$

where g is a gain function affecting the magnitude of increasing FR, E(i) is the current excitation and RT(i) and MFR(i) are the threshold of recruitment and the minimum firing rate for the indexed MU respectively. The FR will increase according to this function

until the ith motor unit achieves its peak firing rate (PFR). The PFR for a given motor

unit will be assigned such that PFR is directly proportional to RT (145) within a narrow

range (10 Hz). The fastest MUs will fire at 45 Hz (30). Each pulse delivered by a given

MU model will initiate modeled release of calcium, as described in the next section.

Step 3. Calcium Kinetics

Delivery of an action potential from the motor unit model will result in the release

of calcium from the sarcoplasmic reticulum. Physiologically, this event is mediated by a

complicated series of events. Binding of neurotransmitters released at the neuromuscular

junction, depolarization of the sarcolemma and transverse tubules, activation of voltage-

sensing dihydropyridine receptors, and activation of ryanodine receptors all precede

release of Ca^{2+} from the sarcoplasmic reticulum. However, it is not entirely clear how

these events change during fatigue *in vivo*, and there is little evidence to suggest the time

course for membrane depolarization would be different between old and young human

skeletal muscle *in vivo*. In addition, the kinetics of the Ca^{2+} transient are slower than

those of the depolarization event (45; 129). Because of these considerations, the time

course of the depolarization event will be ignored as an individual component in this

model. Release and resequestration of Ca^{2+} will be calculated similarly to Ding et al

(43). Muscle activation will be modeled using the following ordinary differential

equation:

$$\frac{dC_N}{dt} = \frac{1}{\tau_c} \sum_{i=1}^{n} R_i \exp\left(-\frac{t-t_i}{\tau_c}\right) - \frac{C_N}{\tau_c} \qquad (3)$$

where C_N represents the normalized amount of Ca^{2+} troponin complexed, R_i accounts for

the nonlinear summation of the Ca^{2+} transients and τ_c is a time constant controlling the

rise and decay of C_N. Coefficients tested in Ding et al (42; 43) will be used to

parameterize the current model. An important difference between the proposed model

and that of Ding et al (42; 43) is that modeled motor unit excitation will replace modeled

electrical stimulation.

Step 4. Muscle Model

A Hill-type muscle model will

be used to characterize the force and

energetic responses to activation. Input

for 120 independent muscle models

will be derived from the modeled Ca^{2+}

release from the previous step. Each

muscle model will include a contractile

component to mimic the active force

generating properties of skeletal

Figure 3.6 Plot of force-length relationships for contractile component (CC) and series elastic components (SEC) of the hill type muscle mode.

muscle. Force output will be sensitive to length (Figure 6) and velocity. Parallel and

series elastic elements will mimic passive force-length properties of the tibialis anterior

(175). Series elastic component (SEC) force-length relationship is represented

graphically in Figure 6. Parameters dictating activation and force for the contractile

component will be adjusted such that their behavior will match experimental measures of

motor unit force in the tibialis anterior muscle (178). Total force predicted by the

summed activation of all muscle models will be input to a musculo-skeletal model of the

ankle, and torque values will be derived as described in step 5.

To test hypotheses 2 and 3, a metabolic cost function, which predicts the increased $[H^+]$ and $[Pi]$ as a consequence of force generation, will be added to the model. These values will be used to calculate diprotonated phosphate ($H_2PO_4^-$) concentration based on $[Pi]$, $[H^+]$ and the pK of phosphoric acid (6.75).

$$[H_2PO_4^-] = [Pi]/1 + 10^{pH-6.75} \qquad (4)$$

The $[H_2PO_4^-]$ will be directly related to a limit on the maximum force-generating capacity of the contractile element (F) based on relationships established in the literature for human muscle (14; 106; 111; 135). The data from Lanza et al (91) will be used for initial attempts at predicting changes in F with increasing $[H_2PO_4^-]$ and forms the basis for the following equation:

$$F\% = 1.12 - 0.0215 \cdot [H_2PO_4^-] \qquad (5)$$

Additional functions will describe alterations to the force-velocity relationship and Ca^{2+} sensitivity with repeated activation, based on values derived from in vitro research (2). The association between muscle work and change in $[H^+]$ will be modeled in a similar fashion to Giat et al (62; 63). While their experimental data in electrically-stimulated quadriceps will be used as a starting point, parameter values will be modified to better represent our population and muscle group. Our own data will be used to model rates of glycolysis, PCr breakdown and H^+ buffering capacity (see Source Data, below) to derive modeled rates of intracellular Pi and H^+ formation. During periods with no stimulation, modeled rates of restoration of $[H^+]$ and $[Pi]$ to resting values will dictate $[H_2PO_4^-]$ and, as a result, recovery from fatigue.

The distribution of muscle fiber types reported in the human tibialis anterior will be mimicked by adjusting parameters related to metabolic cost and contractile dynamics.

The tibialis anterior muscle is composed primarily of type I fibers, especially in older adults (92). Muscle models will be parameterized such that 64.5% of the models represent the behavior of type I fibers and 35.5% are type II (92). When the model is adjusted for age to test Hypothesis 3, these relative populations will be adjusted to 81.1% and 18.9% for fiber types I and II, respectively (92). Because there are 120 motor units, there will be 97 type one muscle models representing type I characteristics and 23 representing type II. They will be assigned to like-numbered motor units so that a discharge of the ith motor unit corresponds to the ith muscle model. "Type I" muscle models will be assigned lower numbers than all "type II" muscle models, following the association between motor neuron properties and contractile characteristics observed in vivo. Contractile dynamics and metabolic cost characteristics will be invariant between muscle models of the same type. However, the force generating capacity of each muscle model will reflect the up to 100 fold range of force per motor unit observed in human muscle (136). This range will be reflected across the 120 muscle models using an approach similar to Fugelvand et al (59):

$$F(i) = e^{b*I} \qquad\qquad (6)$$

Where F refers to the peak force generating capacity of the *ith* muscle model and

$$b = (ln\ 100)/120 \qquad\qquad (7)$$

This will lead to model forces with the desired range (100 fold) across the desired number of models (120) expressed in terms relative to the first muscle model.

Step 5. Joint Torque

A simplified musculo-skeletal model of the ankle joint will be added to the model computation to allow for translation of muscle force to joint torque. The linear sum of forces generated by muscle models in step 4 will be scaled to the physiological cross sectional area of the tibialis anterior muscle to arrive at tendon force. Physiological cross sectional area (PCSA) refers to the average cross section of anterior compartment (CSA) muscle area multiplied by the cosine of its fascicle pennation angle. This step is taken to account for the angle of applied force of fascicles with respect to the line of action of their summed forces at the apponeurosis.

$$PCSA = CSA \bullet \cos(\theta) \tag{8}$$

Tendon force will be multiplied by a calculated moment arm to determine joint torque. The moment arm length itself will depend on tendon force. This relationship will be based on data available in the literature (127). The correlation between force and moment arm length is meant to represent the elasticity of the extensor retinaculum, which binds the tendons of the muscles in the anterior compartment at the ankle, constraining their force path.

Step 6. Controller

A bounded, proportional controller will determine the E that minimizes error between MT and TT. The controller will have kinetics at least one order of magnitude faster than the contractile kinetics of the
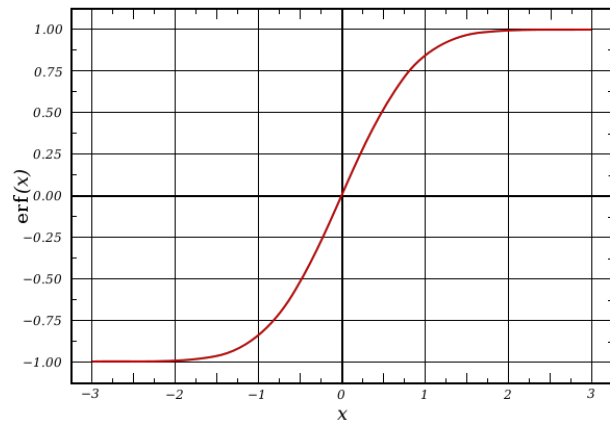
Figure 7. Plot of a typical error function with Gaussian distribution. The error function is bound between 1 and -1.

muscle model in order to minimize its effects on temporal prediction of force. Its final form will be determined after other components of the model are complete. The E controller will follow either a traditional root mean square error function or a state-dependent function where a single rate constant dictates step size for E control (190).

A Gaus error function will follow the form shown in Figure 7. Solving for this function (bound between -1 and 1) will serve as a coefficient to be multiplied by the difference in E_i and E_o.

Alternately, a state-dependent control function, similar to Xia et al, (2008) will be devised. Briefly, if:

$$MT < TT, \Delta E = L_d \bullet (E_o - E_i) \tag{9}$$

$$MT \geq TT, \Delta E = L_R \bullet (E_o - E_i) \tag{10}$$

Where L_d and L_R represent rate constants describing the development and reduction of E.

In addition to the preceding methods, E will be determined by optimizing an error-tracking function of the task to be performed. A forward dynamics optimization will be applied, with the task of minimizing the difference between MT and TT by varying E. Once complete, this time history for E will be used to numerically integrate the deterministic equations, which dictate subsequent model behavior.

Determination of the control strategy will follow completion of testing for Hypothesis 1. All proposed controller functions will be used to model a 5-second contraction, where TT is equal to 90% of the output for Hypothesis 1. The control strategy that yields the fastest computation speed will be used for subsequent analysis. In the case that the fastest control method yields unrealistic results (E, and consequently MT, wavering about TT, for example) the next fastest method will be selected.

Source Data

The model will draw on published and unpublished data sets available from multiple projects conducted in the Muscle Physiology and Biomechanics Laboratories at the University of Massachusetts, Amherst. When necessary, as outlined in the preceding section, model components and parameters will be drawn from the literature. Figure 8 lists published muscle models and source data that correspond to each step of the proposed model, similar to Figure 5.

Subject Characteristics

Young men (21 – 35 years, n = 8) were healthy by self report, non-smokers, and at least recreationally active. Participants were familiar with torque measurement using a Biodex dynamometer (Biodex Medical Systems, Shirley, NY) and refrained from exercise on all testing days. Data for the same measures are also available in a sample of older men (65 – 80 years, n = 19). However, data from older men are from two separate
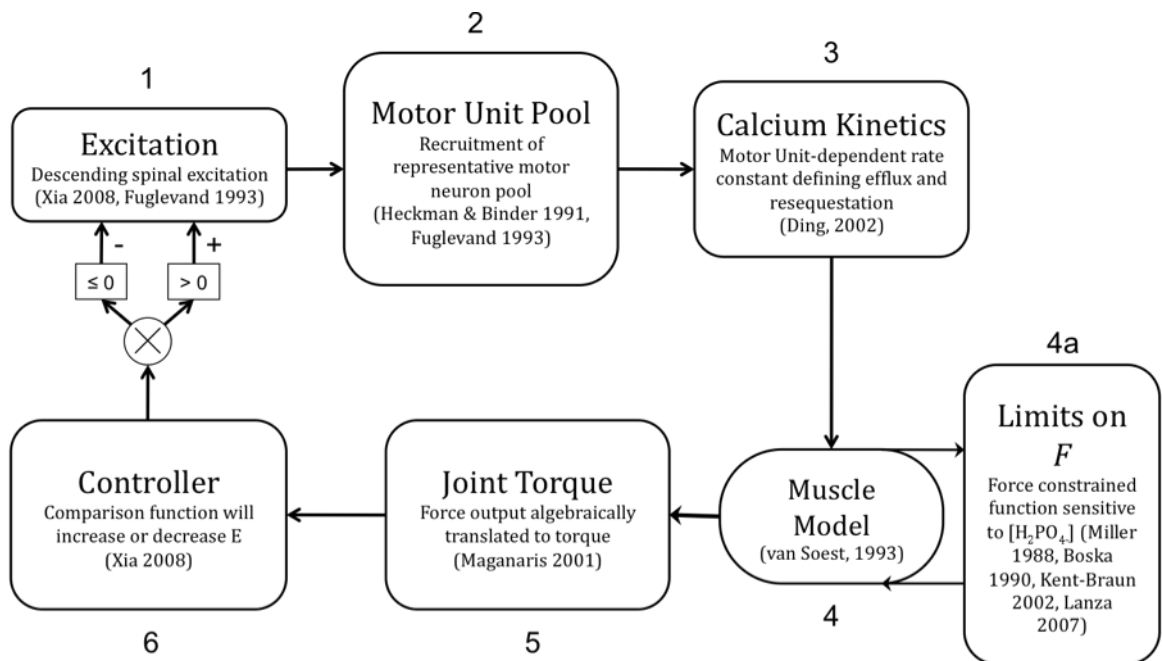
Figure 8. Source data scheme for computational model components. The source for data that will parameterize each model component is listed in the appropriate cell.

studies. The biomechanical data were collected from a group of 11 older men, while the

energetic data were collected in a separate sample of 8 older men. All 19 older men in

the combined data set were healthy by self report and non-smokers. Experimentally-

derived values will be used in step 4a to formulate metabolic cost functions that predict

generation of H^+ and Pi ($H_2PO_4^-$). These values will ultimately limit F in a Hill-based

muscle model. Tendon stiffness and pennation angle, measured in the tibialis anterior

muscle will be used to parameterize the musculo-skeletal model that predicts joint torque

in steps 5.

Limits on F

Force generation in the model will be associated with changes in the predicted

concentration of $H_2PO_4^-$ which will, in turn, limit F in the muscle model as described

previously. The metabolic perturbations associated with dorsiflexion (metabolic cost)

were calculated as described elsewhere (Lanza et al (111)). Briefly, ^{31}P MRS was used to

measure the concentrations of phosphate-containing metabolites, phosphocreatine (PCr),

inorganic phosphate (Pi), adenosine triphosphate (ATP), and phosphomonoesters (PME)

in the ankle dorsiflexors using a 4.0 tesla superconducting magnet (Bruker Biospin,
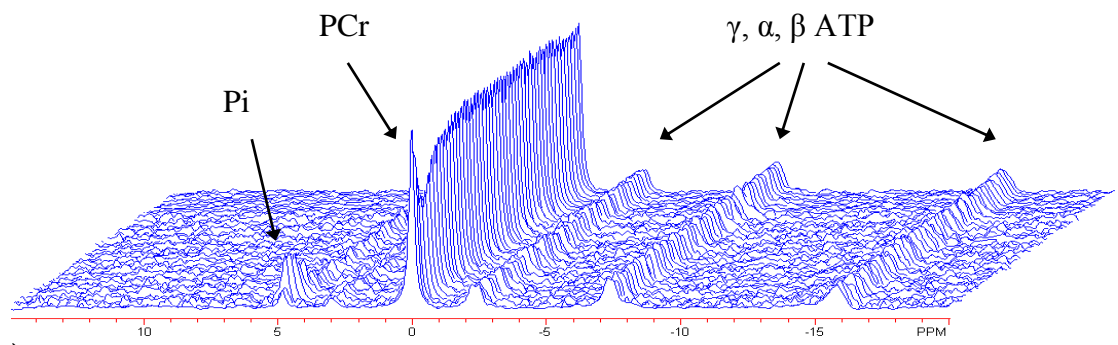
Figure 3.9 Stack plot of ^{31}P MRS (magnetic resonance spectroscopy) data. Peaks correspond to
Pi, PCr, and the three phosphate groups on ATP (γ, α, β)

Rheinstetten, Germany). A stack-plot of spectra acquired from a typical study are presented in Figure 9. The recovery of PCr following a 12-second MVIC was used to calculate the in vivo capacity for oxidative phosphorylation (110; 134). By measuring the changes in metabolite concentrations, and calculating pH, based on the chemical shift between Pi and PCr (138), the metabolic cost of contraction was calculated in mM ATP•s^{-1}. Metabolic cost was calculated for contractions at a range of intensities (20%, 50%, and 100% MVC) to better characterize the relationship between force and metabolic cost. Oxidative flux, glycolytic flux, and ATP synthesis through the creatine kinase reaction were measured during contractions at each intensity by spectral analysis using NUTS software (Acorn NMR, Livermore CA). Based on these data, model functions will be created to reflect the cost of force production and the subsequent change in pH across a range of activation levels.

Muscle Architecture

Muscle architecture measures were performed at the University of Massachusetts Amherst and Cooley Dickinson Hospital Imaging Facility in Amherst MA respectively. Muscle architecture and volume was measured using ultrasound and MRI techniques. Ultrasound imaging was used to measure the tibialis anterior muscle and tendon while a subject was seated in a Biodex isokinetic dynamometer. With the ankle fixed at 120° relative to the tibia, subjects performed a
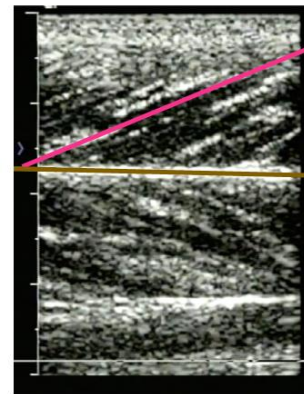
Figure 3.10 Ultrasound image of the anterior compartment of the lower limb. The horizontal line matches the orientation of the apponeurosis of the tibialis anterior muscle, and the angled line matches the pennation angle of visible fascicles under the ultrasound probe.

46

torque-tracking task by matching their effort to visual feedback. When performed

correctly, they steadily increased dorsiflexion torque from rest, to 100% MVIC over a

period of 10 seconds. During this time, fascicle pennation angle (Figure 10) and stretch

of the tibialis anterior tendon was recorded on videocassette for subsequent analysis using

custom written Matlab software (Hasson, unpublished communication).

To measure muscle volume, serial sections of MRI (T1 weighted spin echo axial

images; 4 mm slice thickness, 210 mm field of view, 512x512 matrix) were collected for

the total shank length. Custom written Matlab software

was used to first identify a region of interest (ROI)

representing the tibialis anterior muscle, and then

decompose the pixels populating this ROI into

contractile and non-contractile tissue based on signal

intensity. A sample MRI slice with defined ROI is

Figure 3.11 Magnetic resonance image (MRI) in the axial plane of the shank. The dotted line represents the region of interest (ROI) for subsequent analysis of muscle size.

shown in Figure 11. Total muscle volume was

determined from measured cross sectional area

combined with the thickness of each slice.

Hypothesis Evaluation

Each component of the complete model will be tested by comparing the

respective output to experimentally measured data. When agreement is reached between

model parameters and measured behavior for Hypothesis 1, the model will be adjusted to

examine fatigue, and then adjusted to mimic age-related changes to the neuromuscular

system. The values used to validate model predictions, and sources for parameter

modification are summarized in the Appendix.

Hypotheses 1 will be tested by comparing predicted values for peak torque to the measured values in young men. A step input will be used to compute the model's response to a 4-second MVC running at 2000 Hz during a 5-second simulation. The E control signal will be equal to zero for 0.5 seconds (1000 data steps), at which point it will increase to 1. At 4.5 seconds, the E will again be set to zero, where it will remain until the end of the simulation. The peak torque calculated during this simulation will be compared to the average peak torque generated by young men recruited for experimental data collection. The model will be considered valid if it predicts torque output within one standard deviation (6.9 Nm) of the mean (45.0 Nm).

Hypothesis 2 will be tested by comparing modeled prediction to literature values of fatigue from Lanza et al (111). Fatigue will be defined by expressing the time-torque integral (TTI) produced by the last of 6, 12-second contractions relative to an un-fatigued 12-second contraction. The TTI for an un-fatigued contraction was calculated by multiplying peak torque achieved at baseline by 12 seconds. The model will be considered valid if its prediction is within one standard deviation (8.3%) of the mean fatigue (73.6%) in young men reported by Lanza et al (111).

Hypothesis 3 will be evaluated in a manner similar to Hypotheses 1 and 2. Once parameters within steps 2, 4, and 5 are adjusted to reflect age-related changes in the neuromuscular system, a step input will be used to predict MVC torque for older men. This value will be compared to experimentally-measured torque in the men from whom biomechanical data were derived. The model will be considered valid if predicted torque is within one standard deviation (7.9 Nm) of the average value recorded in 8 older men (39.7 Nm). Modeled age-related fatigue resistance will be tested by running a simulation

similar to Hypothesis 2, with age- adjusted parameters. The model will again be considered valid if the predicted fatigue is within one standard deviation (6.9%) of the mean fatigue in older men (84.6%) reported by Lanza et al (111).

Provided the completed model supports the three stated hypotheses, exploratory modification of model parameters will be undertaken to answer additional questions. An important consideration when attempting to understand the mechanisms of age-related fatigue resistance is the potential role of improved metabolic economy that has been observed in older adults (174). This may be due to slowed contractile characteristics due to a generally greater proportion of type I fibers in the muscles of older individuals. Reduced metabolic costs of activation due to decreased firing rates may also play a role in improved economy.

The proposed model might be modified to associate metabolic cost to activation (based on Ca^{2+} transients) in addition to force generation. The relative dependence of metabolic cost on force and activation can be modified to reflect the wide range reported in the literature to better understand its potential role in fatigue resistance.

Additional testing might include modification of model parameters to reflect age-related changes in muscle fiber type. If muscle fiber type plays a strong role in fatigue resistance, it would be interesting to alter muscle fiber populations within the proposed model to reflect the range of phenotypes expressed within human skeletal muscle. Results from these modifications will address hypotheses related to the role of fiber-type in varying fatigue characteristics observed across different muscle groups.

CHAPTER 4

AN INTEGRATED MODEL OF NEURAL ACTIVATION, MUSCLE FORCE DEVELOPMENT, METABOLIC PERTURBATION AND TORQUE GENERATION DURING VOLUNTARY CONTRACTION

<u>Abstract</u>

Development of joint torque through the voluntary activation of skeletal muscle is the result of a complicated series of events, beginning with the generation of excitatory action potentials in the motor cortex. A theoretical pathway of voluntary joint torque production includes motor neuron recruitment and rate-coding, sarcolemmal depolarization and calcium release by the sarcoplasmic reticulum, and force generation by the contractile proteins. The direct source of energetic support for this process is ATP hydrolysis. Although it is possible to examine portions of this physiologic pathway using various in vivo and in vitro techniques, none provide a complete view of the multiple ways in which features of the pathway interact and ultimately impact joint torque. Computational modeling provides a means to simulate these interactions and their net outcome, and thereby make inferences about key variables of interest. We present a novel, comprehensive computational model of the activated neuromuscular system. Components representing excitatory drive, calcium release, force generation, metabolic perturbations, and torque generated during human voluntary dorsiflexion were constructed from a combination of literature values and experimentally-derived data. Simulations were validated by comparing model output to voluntary and stimulated torque generation conditions in vivo. The model successfully predicted peak torque output, approximated submaximal torque, and the metabolic perturbations associated

with those levels of muscular contraction. The comprehensive model of neuromuscular

function presented here provides a powerful tool for developing hypotheses related to

voluntary torque generation.

Introduction

Although muscle size is the single largest determinant of maximal voluntary joint torque in humans (104), only roughly two-thirds of maximal torque is accounted for by muscle size, and there are examples in the literature of considerable variation in specific strength (voluntary torque generated per muscle size) (141). The generation of voluntary torque begins with neural excitation in the motor cortex that produces propagation of excitatory potentials down cortico-spinal tracks to the α motor neurons that synapse with the muscle cells and cause depolarization of the sarcolemma. This is followed by release of Ca^{2+} from the sarcoplasmic reticulum, thereby activating cross-bridge cycling and the development of force. Clearly, any variation in the processes along this pathway may result in alterations in muscle force and consequently joint torque. Such variations could include those due to differences in motor unit, muscle fiber, muscle-tendon, or metabolic properties, or the interactions between these systems.

The interrelated nature of the physiological processes involved in the generation of voluntary joint torque is difficult to discern in vivo. While in vitro experimentation can provide explicit details about isolated systems, and in vivo studies typically describe the combined function of multiple systems, each are limited in addressing the coordinated events that lead to the development of voluntary joint torque. Model simulations on the other hand, are commonly used to predict the responses of complicated systems whose interrelated components might preclude direct measurement or control.

Recently developed models have provided valuable insights that would have not been possible using standard in vivo or in vitro approaches. Since the first mathematical models of skeletal muscle function, first described in the 1950s by A.V. Hill (82) and Hugh Huxley (90), computational models have been proposed to explain the physiological behavior of skeletal muscle perfusion, neuromuscular activation and even fatigue during repeated activations. However each of these examples focus on a single portion of a system whose combined function is highly interrelated.

While a unitary approach to modeling complicated systems is justified, a comprehensive model that allows simultaneous inquiry of multiple physiological events associated with the voluntary production of joint torque would be a useful tool to investigators interested in neuromuscular function. Currently available simulations have been developed which simulate the behavior of activation (59), discharge, and spatial distribution (58) of motor units; depolarization of the sarcolemma (54); calcium kinetics (131; 187); acto-myosin binding kinetics (70; 83; 166); and control of oxidative phosphorylation by ADP (94). However, rarely have multiple physiological components been included in the same model (63).

The goal of the present study was to construct a comprehensive model of neural activation, contractile dynamics, and metabolic perturbation. The approach combines previously-validated simulations of voluntary activation (59; 75), force development (76; 177; 181) and torque generation (126) with a novel set of model components that regulated neural activation and predicted metabolic perturbation as a consequence of muscle activation. Ours is the first to incorporate features of voluntary activation, force generation, metabolic perturbation and joint torque, along with predictions of multiple

intracellular metabolites. Here, we present a model capable of predicting the kinetics and

magnitude of voluntary torque generation, along with the neural excitation necessary to

evoke such a response, and the intracellular metabolic consequences that follow.

Methods

Approach

Our approach to an integrated, comprehensive model of neuromuscular function

followed the general scheme outlined in Figure 1. Considerable effort was made to base

model parameters on human literature values and experimental measures available from

recent, ongoing studies in the Department of Kinesiology at the University of

Massachusetts Amherst.

Source Data and Subject Characteristics

The model drew on published and unpublished data, available from two available

projects conducted in the Muscle Physiology, Biomechanics and Locomotion

Laboratories at the University of Massachusetts, Amherst. A musculoskeletal model was

developed based on experimentally-obtained anatomical data in a group of healthy young

men. The same individuals were also underwent metabolic testing using non-invasive,

^{31}P magnetic resonance spectroscopy (MRS). When necessary, model components and

parameters were drawn from the literature. The young men ($21 - 35$ years, $n = 8$) who

comprised the cohort in each available data-set, were healthy by self-report and non-

smokers. All participants were recreationally active, engaging in endurance exercise

multiple times per week. Participants were familiar with the torque measurement

procedures using a Biodex dynamometer (Biodex Medical Systems, Shirley, NY) and

refrained from exercise on all testing days.
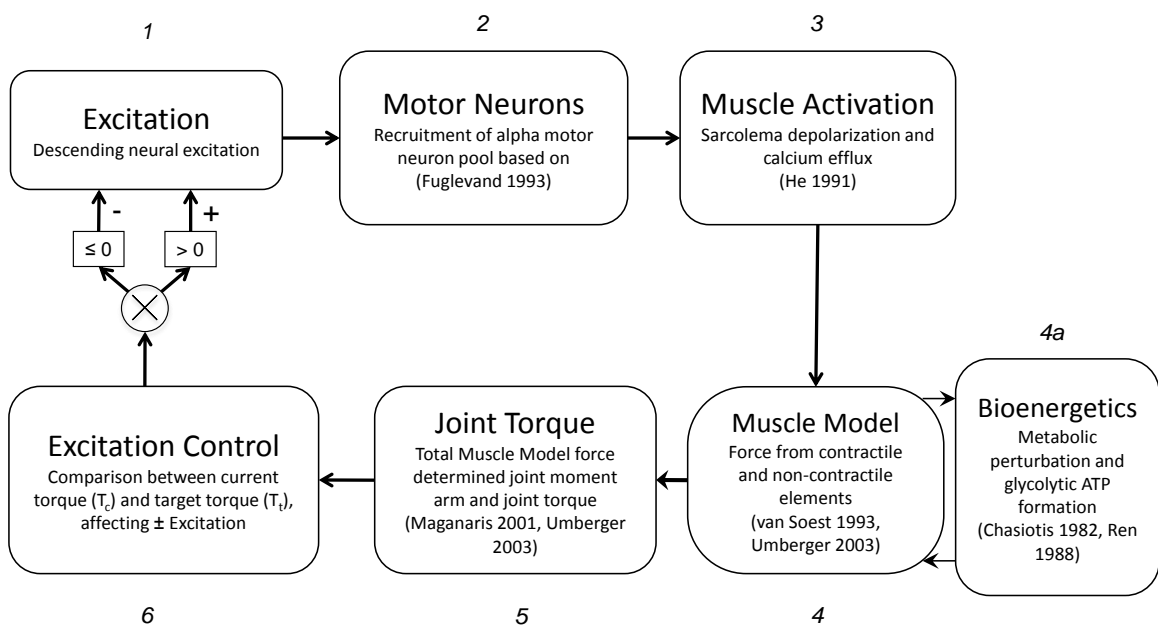
Figure 4.1 Computational approach. The model will be run using a forward integration routine to calculate each model step (1-6) at each time point for the duration of the simulation. Primary literature sources pertinent to model functions are listed with each step

Figure 1 lists published muscle models and source data that correspond to each step of the proposed model.

Computational Overview

Because the model incorporates the output from multiple components meant to represent stages in the pathway to torque production, they are presented here sequentially, as they were computed in the forward dynamics simulation using Matlab software (MathWorks, Natick MA) throughout for model formulation and testing. The steps are illustrated along with points corresponding to source data in Figure 1.

Briefly, a single parameter representing voluntary excitation (Step 1) of the spinal cord initiated the forward dynamics model by serving as the input for a modeled pool of motor neurons (MN). This simulated pool of 120 α motor neurons largely followed a recruitment scheme originally proposed by Fuglevand et al (59). This pool responded to excitation by calculating firing rates (FR) for each modeled motor neuron (Step 2). A model of activation (sarcolemal depolarization and intracellular calcium release) followed (Step 3) for a Hill-type muscle model (Step 4). Because the output of each MN acts on a corresponding muscle model, this effectively simulates the organization and behavior of a motor unit (MU) in vivo. The linear sum of forces produced by all muscle models was then used as the input for a musculo-skeletal model of the ankle joint to predict current joint torque (T_c) at the ankle (Step 5). Finally, T_c was compared with a pre-defined timeline of a torque task (T_t) which allowed for adjustment to excitation (S, Step 1) such that the difference between T_c and T_t was minimized. In this forward integration model, functions received no input beyond initial conditions and T_t.

Calculations were performed for time steps of 0.001s and repeated for each MU before advancing the time step. Data for each time step were calculated using the 'ode45' solver function within Matlab. Three primary functions were used in the forward integration process. First, a calling function initialized variables used in subsequent functions and adjusted the excitation signal meant to represent voluntary effort. A second function predicted the motor unit discharge rates for all motor units in response to the current level of excitation. Finally, a system of equations that determined force and bioenergetic variables determined the response to input from the motor unit function. Additional detail regarding the output of these steps and formulation of these functions is provided below, and in Appendix D.

Step 1. Excitation

The initial step for the model represents excitation which begins at the motor cortex and descends through corticospinal tracts to α motor neurons in the spinal cord. Input from the central nervous system to pools of α motor neurons is physiologically complex and dictates many aspects of coordinated, voluntary muscle activation. Because of its complicated nature and incomplete definition in the literature, no attempt is made for the computation of the excitation signal (S) to directly reflect physical events in the process of cortical excitation.

Once initiated, the model adjusts S at each time step to minimize the difference between current modeled torque (T_c) and target torque (T_t) with respect to peak torque generating capacity:

$$T_{diff} = T_c - T_t \tag{1}$$

in the case where T_{diff} is < 0,

$$\uparrow S = S + (T_{diff} \cdot (1 - S)) \qquad (2)$$

and in the case where T_{diff} is > 0,

$$\downarrow S = S - (T_{diff})^R \cdot S \qquad (3)$$

This simple control algorithm uses the value $R = 0.7$ to minimize unintended relaxation

characteristics while maintaining predictions for activation and relaxation that were

consistent with in vivo observation. Specifically, R was set below 1 to allow for

sufficiently rapid de-activation rates that eliminated persistent, low-level activation

observed in simulations using lower rates of deactivation. An estimate of peak torque

generating capacity was established by multiplying the sum of peak force generating

capacity for each muscle model by the maximum possible moment arm. This estimate is

not necessarily the same as actual peak torque generating capacity, which is also subject

to other model elements (firing rate, activation, contractile element length and velocity).

Step 2. Motor Neuron Pool

The pool of 120 motor neurons responded to the level of excitation (S) according

to procedures described by Fuglevand et al, (59). The recruitment thresholds (RT) for the

pool of MNs were distributed such that many MNs had low RT while relatively few had

high RT. The distribution of recruitment thresholds is described mathematically by the

equation:

$$muRT_m = \exp(a) \qquad (4)$$

where $muRT_m$ is the (RT) of MN (m) and $a = \log(A_r)/m$, $A_r = 30$ is the desired range

(fold difference) for $muRT_m$. A 30-fold range of RT is consistent with the broad variation

in recruitment thresholds observed experimentally (178). Each MN is assigned a

minimum firing rate (MFR) of 8 Hz (30; 178). Although it is possible that MFR could vary between motor neurons in direct proportion to RT (67), empirical studies performed in humans during voluntary contractions suggest that MFR is constant across MNs (35; 136).

Once a MN's threshold for excitation was surpassed, a single linear function described the relationship between excitation and FR:

$$FR = G \cdot (S - (muRT_m)) + MFR \tag{5}$$

where G is a gain function affecting the magnitude of increasing FR, S is the current excitation. FR increased according to this function until the given motor neurons achieved its peak firing rate (PFR). The PFR(m) is directly proportional to RT(m) within the relatively narrow range of 10 Hz (145). The fastest MNs fired at 56 Hz (30). Each "pulse" delivered by a given MN model initiated a model of muscle activation, described in the next section.

Step 3. Muscle Activation

Because the kinetics of the Ca^{2+} transient are significantly slower than those of the depolarization event (45; 129) and precise measurement of the calcium transient are exceedingly difficult in vivo, no effort is made to distinguish the two events in the present model. The combined steps of post-synaptic muscle activation were modeled similarly to the approach used by He et al (76):

$$\dot{act} = (Stim - act) \cdot (rc_1 \cdot Stim + rc_2) \tag{6}$$

$$rc_2 = 1/t_{deact} \tag{7}$$

$$rc_1 = 1/t_{act} - rc_2 \tag{8}$$

where t_{act} has values between 0.060 - 0.039 depending on MN assignment (m) and represents the activation time constant. Deactivation time constants are defined by t_{deact}

and have values between 0.092 - 0.064. These values were based on Umberger and

colleagues (177) and modified slightly for this application. Specifically, values were

altered to allow for a range of activation and deactivation kinetics within the MN pool,

and optimized along with contractile kinetics (detailed later) to produced rates of force

development and relaxation that were physiologically realistic. *Stim* has a value of either

"1" or "0" depending on whether a counter, initiated once a MN is recruited, is less than

0.023. The counter continues for the duration of the current interpulse interval (IPI) and

Stim = 0 until it is reset (detailed description of this process can be found in Appendix D).

This procedure is followed to mimic the duration and kinetics of the calcium transient.

Accordingly, this activation strategy yields activation kinetics consistent with the time

course of experimentally observed (151) calcium transients (20-30 ms) and complete

summation of the calcium transient for the MN with the lowest maximal discharge rate

during full stimulation.

Step 4. Muscle Models

A detailed list of equations describing the behavior of the muscle and metabolic

perturbation model can be found in Appendix D. The text that follows is a general

description of the model formulation procedures.

The activation signal from step 3 was input to a standard Hill muscle model that

included contractile (CE) and series elastic (SEE) elements (181). In keeping with the

control structure of the model overall, 120 independent muscle models responded to the

output of 120 MNs. This coordination was intended to reproduce the physiological

recruitment of motor units. Peak force-generating capacity of each muscle model (*fmax*)

was coordinated with *muRT* such that the unit with the lowest recruitment threshold had

the lowest force. Forces were distributed across 120 MNs through a 100-fold range (see Appendix D). The sum of *fmax* from all muscle models was adjusted to match a value derived from an optimization routine that determined specific tension from the study population (Umberger, XIII International Symposium on Computer Simulation in Biomechanics, June 30th - July 2nd 2011, Leuven, Belgium). Total myotendonus muscle length was held constant as all modeled contractions where isometric, but CE and SEE length were free to change and behaved according to the equations in Appendix D. All muscle models included components for eccentric and concentric force development, pennation angle, velocity and length.

The modeled change in CE and SEE length, along with resulting changes in pennation angle were based on in vivo ultrasound measures performed at the University of Massachusetts. Briefly, ultrasound imaging was used to measure the tibialis anterior muscle and tendon while subjects were seated in a Biodex isokinetic dynamometer. The ankle was fixed with the foot at 120° relative to the tibia, and subjects performed a torque-tracking task by matching their effort to visual feedback. When performed correctly, they steadily increased dorsiflexion torque from rest, to 100% MVC over a period of 10 seconds. During this time, fascicle pennation angle (Figure 2) and stretch of the tibialis anterior tendon was recorded on videocassette for subsequent analysis using custom written Matlab software (72).

Step 4a. Metabolic Perturbation

The model used current activation level to predict changes in the concentration of intracellular metabolites related to the production of adenosine triphosphate (ATP). The metabolic perturbations associated with dorsiflexion were modeled after measures of

phosphorus-containing metabolites, as described elsewhere (100; 110). Briefly, ^{31}P MRS

was used to measure the concentrations of phosphate-containing metabolites,

phosphocreatine (PCr) and inorganic phosphate (Pi), in the ankle dorsiflexors using a 4.0

tesla superconducting magnet (Bruker Biospin, Rheinstetten, Germany). The recovery of

PCr following a 12-second maximum voluntary contraction (MVC) was used to calculate

the in vivo capacity for oxidative phosphorylation (110; 134) while the distance between

Pi and PCr spectral peaks were used to estimate intracellular pH (101). ATP synthesis

through creatine kinase, anaerobic glycolysis and oxidative phosphorylation was

estimated by tracking changes in [PCr], [Pi], and pH during contractions at a range of

intensities (20%, 50%, and 100% MVC).

Tracking of intracellular concentration of phosphorus containing metabolites was

accomplished by line fitting of time-averaged spectra, using NUTS software (Acorn

NMR, Livermore CA). Based on these data, model functions were created to reflect the

cost of force production and the subsequent change in pH across a range of activation

levels (See Appendix D). The initial rate of PCr break down during contractions of

varying intensity was used to predict rate constants for the appearance of Pi during

contractions that were intensity-dependent (equations 21 and 22 in Appendix D). This

procedure is possible because a constant phosphate pool ([Pi] + [PCr] = 42.5 mM) and

ATP concentration ([ATP] = 8.2 mM) can be assumed under these experimental

conditions. A three-parameter exponential decay line fit was performed using SigmaPlot

software (Systat Software Inc. San Jose, CA) to derive coefficients used to formulate

rates of Pi accumulation during activation (equation 1, Appendix E).

Intracellular pH was calculated for each muscle model, based on rates of change in [Pi], buffering capacity, and protons produced from glycolysis (H^+). Glycolytic rates were estimated from the Michaelis-Menten kinetic relationship between Pi and glycogen phosphorylase, where K_m was assumed to be 18.94 mM (22; 155), and the maximum rate of anaerobic glycolysis was a range between 0.48 and 1.92 mM s^{-1}. This range was chosen to reflect rates of glycolysis observed in vivo (113; 183) and resulted in an average across muscle models, weighted to *fmax* (a direct correlate to muscle volume), of 1.5 mM ATP·s^{-1} through glycolysis. The rate of H^+ produced by non-oxidative glycolysis was equal to the rate of glycolysis/1.5. Glycolytic production of H^+ was offset by the protons consumed in the creatine kinase reaction (net breakdown of PCr), which was calculated from the product of a proton stoichiometry coefficient (θ) and the rate of Pi accumulation (equivalent to PCr breakdown). The net total of H^+ production and consumption was divided by the current buffering capacity to calculate the pH at each time point (equation 34, Appendix D). Finally, [$H_2PO_4^-$] was calculated based on current pH and [Pi] (equation 36, Appendix D).

Step 5. Musculoskeletal Model

The musculoskeletal model, as mentioned, was parameterized with data from a group of healthy young men. Muscle architecture measures were performed using ultrasound and magnetic resonance imaging (MRI) at the University of Massachusetts Amherst and Cooley Dickinson Hospital Imaging Facility in Amherst MA respectively.

To measure muscle volume, serial sections of MRI (T1 weighted spin echo axial images; 4 mm slice thickness, 210 mm field of view, 512x512 matrix) were collected for the total shank length. Custom-written Matlab software was used to first identify a

region of interest (ROI) representing the tibialis anterior muscle, and then decompose the

pixels populating this ROI into contractile and non-contractile tissue based on signal

intensity. A sample MRI slice with defined ROI is shown in Figure 3. Total muscle

volume was determined from measured cross sectional area combined with the thickness

of each slice.

The forces generated by all motor units were summed linearly to predict force at

the tendon (F_t).

$$F_t = \sum_{m=1}^{MU_{num}} fsee_{(m)} \tag{9}$$

Current moment arm length (L_{ma}) was dependent on force F_t such that greater F_t resulted

in a larger L_{ma}.

$$L_{ma} = L_{ma0} + ((L_{ma0} \cdot L_{maR})/(F_{max}/F_t)) \tag{10}$$

where L_{ma0} is maximum moment arm length, L_{maR} is resting moment arm length and F_{max}

is the highest possible isometric F_t. T_c was calculated at the last step and compared with

T_t (equation 1).

$$T_c = F_t \cdot L_{ma} \tag{11}$$
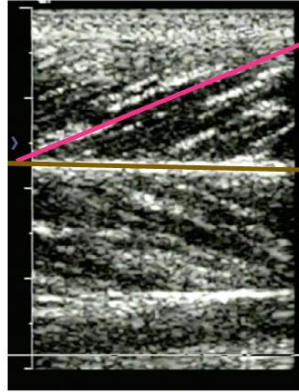
Figure 4.2 Ultrasound image of the anterior compartment of the lower limb. The horizontal line matches the orientation of the apponeurosis of the tibialis anterior muscle, and the angled line matches the pennation angle of visible fascicles under the ultrasound probe
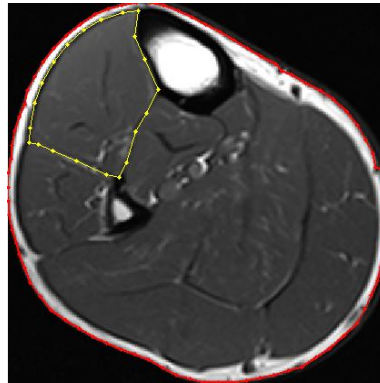
Figure 4.3 Magnetic Resonance Image (MRI) in the Axial Plane. The dotted line represents the region of interest (ROI) for subsequent analysis of anterior compartment muscle size

Simulation and Evaluation Procedures

Equations describing the behavior of each modeled component were run for each MU at each time step (t), for a range of simulated conditions. As an initial test of the validity of model predictions concerning excitation and contractile dynamics, a simulation routine was formulated to generate a torque-frequency curve. Briefly, a train of "stimuli" delivered at a constant frequency was simulated by setting $S = 1$ for the first 0.023 s of a simulated IPI. For a given simulation, IPI was constant and depended on stimulation frequency. This procedure was performed across a range of simulated stimulation frequencies, where IPI was calculated as the reciprocal of the desired stimulation frequency (1/Hz) in each simulation. Simulated torque traces and peak torque achieved were compared with literature values (174).

Next, a range of "voluntary" contraction intensities were simulated, for comparison with the experimental data used to parameterize the model as well as literature values. Under these conditions, T_t was set to increase 1s into the simulation and remain at 110%, 50%, and 20% of predicted maximal T_c until second 13 of the simulation, thus simulating a 12s contraction. The T_t value for the maximal stimulation condition was set in excess of 100% to ensure muscle activation was maximal. Model performance was controlled by auto-regulation of S according to equations 1 and 2. Simulated torque, [Pi], [pH] and [$H_2PO_4^-$] were compared with experimental and literature values for validation.

Results

Torque – Frequency

The recruitment and activation schemes used in the present model agreed well with experimental data. Figure 4A shows model results for neuromuscular stimulation at 20 Hz. The model exhibited pulsatile activation kinetics and wave-summation behavior of torque similar to that observed in vivo. Figure 4B illustrates the simulated torque response to a range of stimulation frequencies between 10 and 50 Hz. The peak torque from each simulation is plotted against its corresponding frequency in Figure 4C along with experimental data from the literature (174). Again, the model agreed well with in vivo torque production at all frequencies. The mean squared difference between simulated and observed torque was 5.3% (between 10 and 45 Hz) with a maximal difference of 7.1% at 30 Hz.

Maximum Voluntary Contraction

During a simulated maximum voluntary contraction (MVC), T_t was set to 110% of expected peak torque output to promote full excitation in the model (grey line, Figure 5A). The model (Figure 5A) predicted peak torque within 5.0% of measured torque in our study group of young men. Similar to in vivo measure, the model achieved ~97% of peak torque within 250ms.

Changes in intracellular [Pi], pH, and [$H_2PO_4^-$] during a 12s maximum voluntary contraction are compared with in vivo data in Figure 5B-D. The model's predicted output, in each case, was within one standard deviation of in vivo measures for all but one time point (pH, 8s).

Submaximal Contractions

To investigate the model's precision when attempting to match T_c with T_t during submaximal activations, T_t was set to 50% and 20% of predicted maximum torque capacity. All other aspects of submaximal simulations were identical to MVC simulations. Results from these simulations are shown in Figures 6A and 7A for contractions at 50% and 20% of MVC respectively. The model's approximation resulted in torque within 2.1% for the middle 90% of contraction time in both simulations. The wavering of T_c about T_t, which was a result of the excitation function's degree of precision and kinetics that were faster than the response of T_t, were consistent with torque variability observed in experimental conditions.

Predicted [Pi], pH, and [$H_2PO_4^-$] are shown with in vivo measures during a 12s contraction at 50% of MVC in Figure 6 B, C, and D respectively. Figure 7 illustrates the same variables during a 12s contraction at 20% of MVC. For [Pi], (Figures 6B and 7B) agreement with experimental data was good, and within the expected physiologic range. Note that the alkalosis typically seen during the onset of contraction was slightly under-predicted (Figures 7C and 8C). Overall, predictions for [$H_2PO_4^-$], which is calculated from the predictions for [Pi] and pH, were excellent at 20% MVC (Figure 7D), but slightly above those at the end of the 12s 50% contraction (Figure 6D).
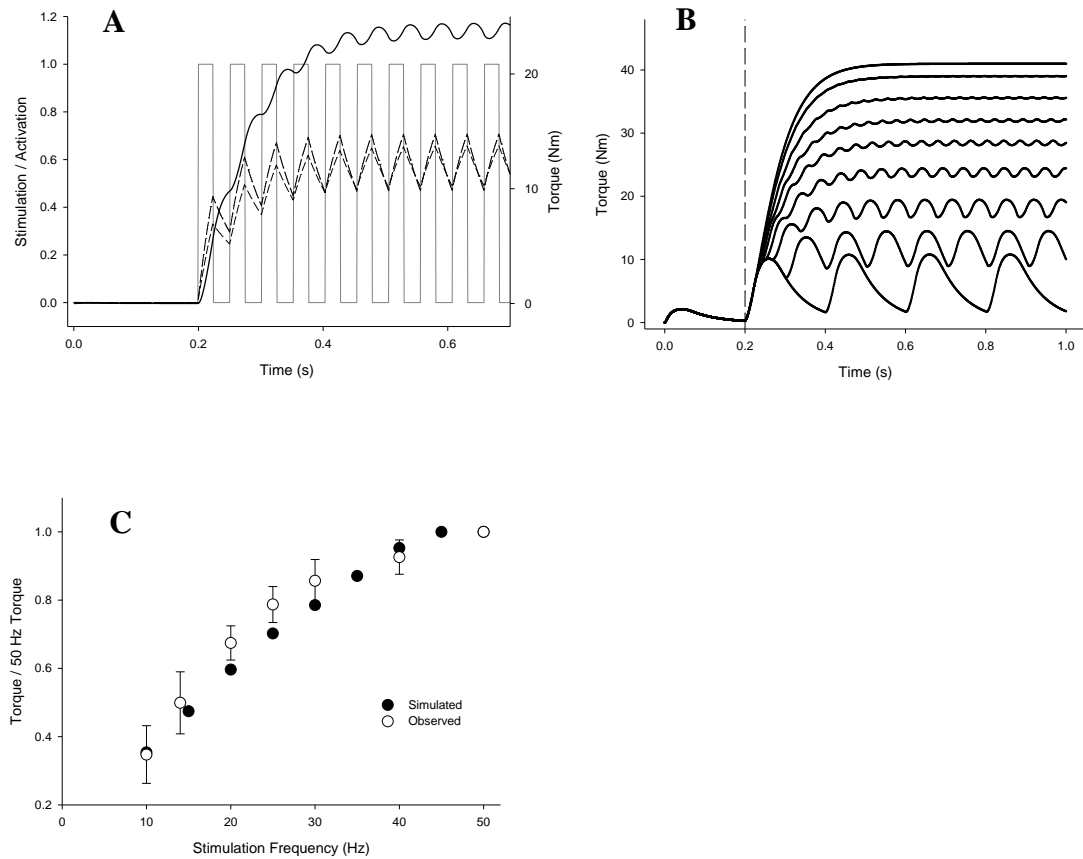
Figure 4.4 Simulated torque-frequency relationship. A: Simulated stimulation protocol was a square wave with pre-determined frequency (20 Hz). Simulated activation responses for the 1st and 60th motor unit are plotted in grey and black respectively. Total simulated torque for the combined model is plotted in blue. **B:** Simulated torque traces in response to stimulation at a range of frequencies (10, 15, 20, 25, 30, 35, 40, and 45 Hz). Stimulation for each simulation began at 0.2s, indicated by the vertical red line. **C:** Comparison between simulated and experimental torque output in response to stimulation at frequencies between 10 and 50 Hz. Simulated torque values (closed symbols) were typically within one standard deviation of mean experimental values (open symbols ± SD)
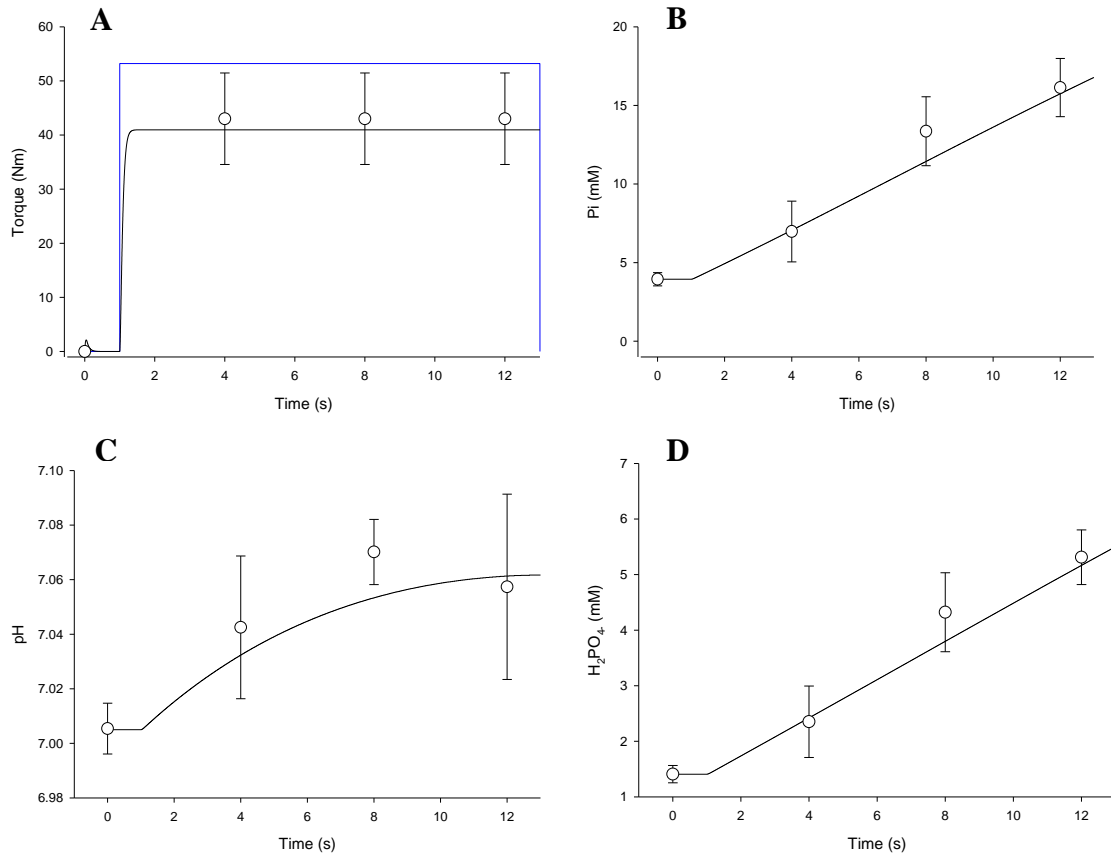
Figure 4.5 Simulated maximum voluntary contraction. A: Simulated torque during 12s MVC in thin black line with experimental data (open symbols ± SD). Blue line is the target torque (T_t) for the model to approximate. It was set to increase from zero to 110% of expected peak torque output to ensure full activation at t=1s. **B:** Simulated (black line) and experimental (open symbols ± SD) inorganic phosphate concentration (mM) during 12s maximum voluntary contraction. **C:** Simulated (black line) and experimental (open symbols ± SD) pH during 12s maximum voluntary contraction. **D:** Simulated (black line) and experimental (open symbols ± SD) H_2PO_{4-} during 12s maximum voluntary contraction
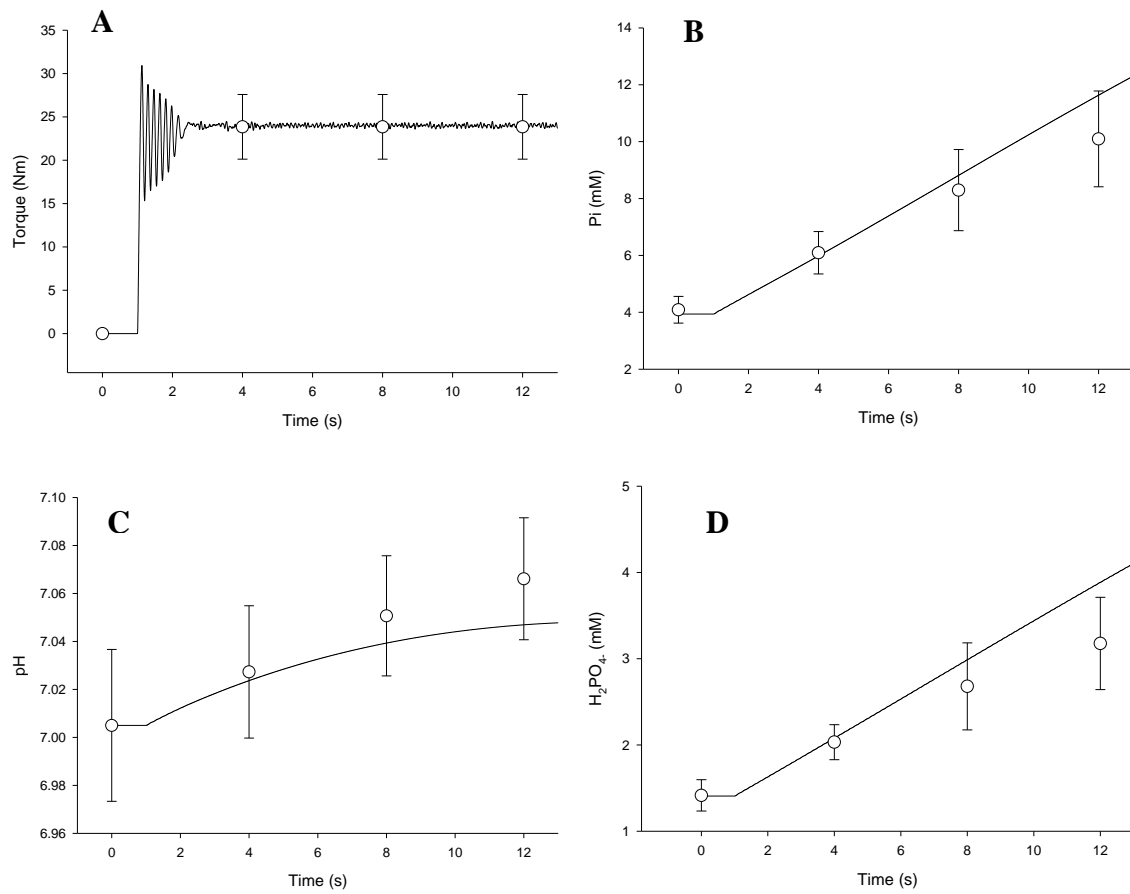
Figure 4.6 Simulated submaximal voluntary contraction at 50% MVC.
Simulated response of Torque (**A**) inorganic phosphate (**B**), pH (**C**), and H_2PO_{4-}
(**D**) during 12s contraction (black line). In vivo data (open symbols ± SD) are
shown for comparison
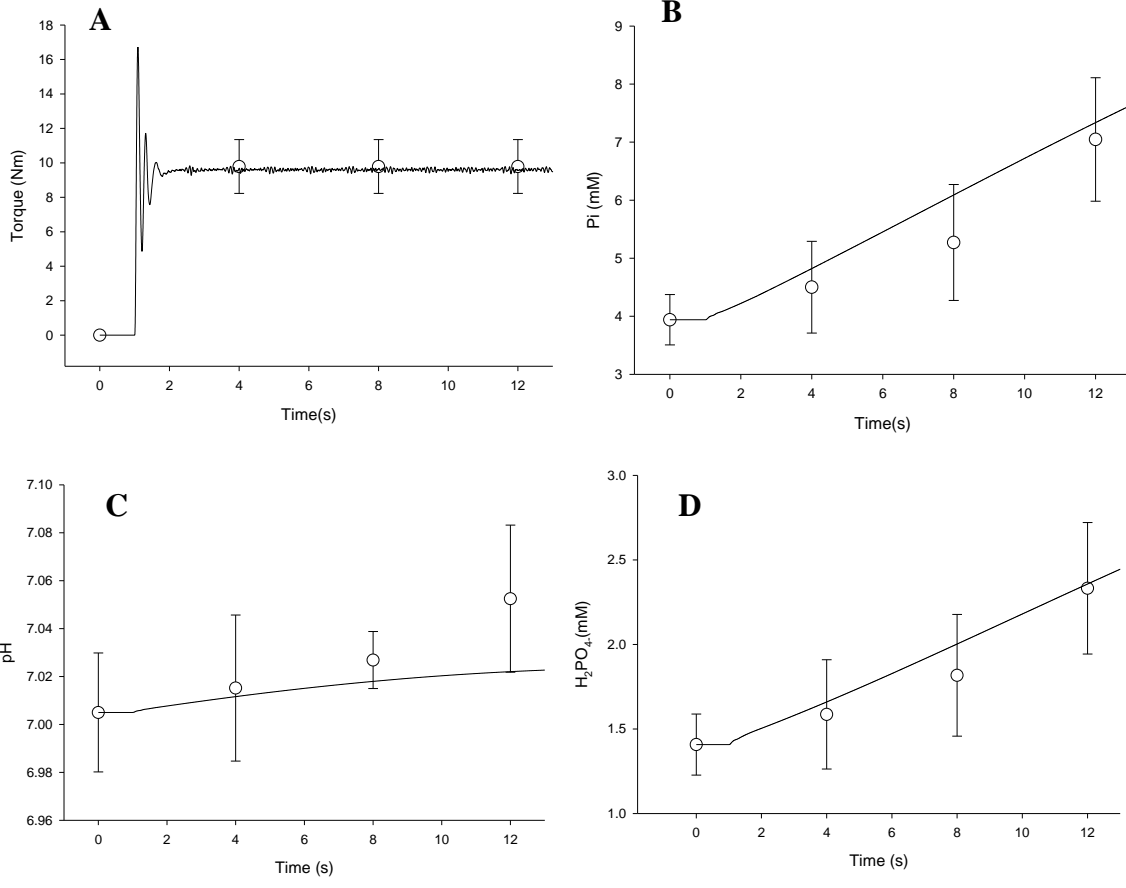
Figure 4.7 Simulated submaximal voluntary contraction at 20% MVC.
Simulated response of torque (A) inorganic phosphate (**B**), pH (**C**), and H_2PO_{4-} (**D**) during 12s contraction (black line). In vivo data (open symbols ± SD) are shown for comparison

Discussion

By synthesizing previously published models for neural activation and force development with an adaptable approach to control of central motor drive and intracellular energetics, the present model is a novel contribution to the field of biophysical modeling. The validation of current model predictions with in vivo data encourages the use of this adaptable control architecture to multiple model simulations.

Compared with previously validated models, some of which serve as bases for components in the present formulation, the model presented here represents a significant advancement in our ability to estimate the neuromuscular response to voluntary activation due to its high level of integration. Several models provide simulations of individual components of neuromuscular function, but few incorporate the range of physiological function with corresponding levels of accuracy. This level of integration is necessary to more completely represent the necessary physiological events involved in voluntary torque generation. As a result, this validated model can be used for a range of simulation conditions to predict the relative effect of failure or enhancements at multiple points in the pathway to voluntary torque production.

A particularly useful feature of the present model is its modular structure, and the manner in which each module produces estimates that can be compared with relevant in vivo data. Overall model behavior depends on the input of each module, and each can be substituted and modified without adjustment of other parameters. In this way, manipulation of a single feature within the model allows for exploration of that component's impact on overall behavior. Further, the ability to mimic voluntary attempts

at achieving target torque allow for a potentially more realistic approximation of physiologic responses to submaximal effort.

Valuable information was gleaned from the formulation and informal optimization of functions used to create the modules presented here. While parameters describing physiological behavior were based on literature values and our own experimental observations, it is important to note that most model inputs were adjusted to ensure realistic predictions by each module. In particular, bioenergetic functions received a large amount of attention to ensure accurate predictions of pH and phosphate metabolites during voluntary activation. Although within the range of values observed experimentally, it was necessary to elevate the value θ by 40% relative to the values reported by Walter et al (183). The value θ is a coefficient that relates to the amount of H^+ produced or consumed during the creatine kinase reaction and varies with cytosolic pH. Using values reported by Walter et al (183) caused an underestimate of alkalosis during contraction. It was found that buffering capacity and the value assigned to θ had the greatest impact on overall predictions of pH during contraction. This was surprising considering the current dogma suggesting glycolysis and resulting acidosis are the primary features of the changing intramyocellular environment during high-intensity muscle contractions. The model, however, suggests inherent buffering capacity and the breakdown of PCr likely have the greatest impact on intracellular pH during brief, isometric contractions.

The present model formulation lacks any consideration for recovery of intracellular metabolites. While the model does an excellent job of predicting neural, contractile, and metabolic responses to torque generation for a range of activation levels,

74

it does not contain functions to predict proton efflux from the cytosol, recovery of resting [PCr], or alterations to buffering capacity that might accompany these responses.

In its present state, the model may be limited by a number of assumptions that were necessary to arrive at the present results. While the range of glycolytic potential for the simulated motor units, and the levels of activation achieved in the simulation yielded values for glycolysis similar to the literature (113) evidence for an absolute limit to peak glycolytic rates in vivo is difficult to ascertain. Further, our model of glycolysis depends on activation kinetics that were characteristically similar to, but relatively slower than our model of Ca^{2+} transients. This is theoretically accurate based on the need for Ca^{2+} in the cytosol to promote glycolysis (152) and reports of slowed onset and offset of glycolysis relative to force generation and relaxation (53). However, this function, like many aspects of the present model, is purely phenomenological and its formulation has little to do with the myriad reactions in the cytosol that likely have dramatic effects on glycolytic rates in vivo.

Finally, the model contains functions that describe the main contributions to $[H_2PO_4^-]$ concentration during muscle contraction. However, it does not include a function to describe the kinetics of oxidative phosphorylation, or the role it plays in cellular homeostasis during contraction. The generation of H^+ from oxidative phosphorylation is negligible when compared with the amounts produced or consumed through glycolysis or the creatine-kinase reaction, but it plays a large role in synthesizing PCr and ATP, especially during prolonged contractions. Its absence for the present application seems to have limited impact, but may limit the models utility in some applications.

Future efforts might be directed to including oxidative metabolism as a model component. A model of oxidative ATP production would allow for simulation of intermittent contraction protocols and recovery of intracellular metabolite concentrations to resting levels. Such a model would be useful in addressing questions related to cellular energetics and the maintenance of cellular homeostasis.

Overall, the model presented here provides simultaneous, accurate predictions of the contractile and metabolic responses to voluntary activation. The novel contributions of the work presented here are twofold: a single, comprehensive model that employs a unique forward integration routine that predicts the neuromuscular response to a variety of contractile tasks; and the integrated components within the model that allow for prediction of multiple physiological responses using a computationally-efficient approach. The model's agreement with experimentally-derived, in vivo data, across a range of contraction intensities, highlights its utility for use as a comprehensive, adaptable simulation tool.

Acknowledgements

CHAPTER 5

PREDICTING MUSCLE FATIGUE DURING INTERMITTENT, MAXIMUM VOLUNTARY CONTRACTIONS: A COMPUTATIONAL MODEL OF ACTIVATION, FORCE GENERATION, AND INTRACELLULAR BIOENERGETICS

<u>Abstract</u>

Muscle fatigue, an acute decrease in force generating capacity, is a process whose mechanisms remain difficult to discern, despite the many studies designed to better understand them. This difficulty is due, in part, to the complicated nature of voluntary muscular force development in vivo. Voluntary skeletal muscle force production is the result of a complicated, interrelated series of physiological events. Reductions in force-generating capacity can be due to alterations in any of these events, limiting our ability to discern their relative impact on force-generating capacity. This limitation is illustrated by the fact that essentially all studies to date have focused on the ultimate outcome of neuromuscular activation (i.e. torque), plus a subset of the many physiological events involved, due to the complexity of assessing their impact simultaneously. Computational modeling has been used as a means to gain insight into systems whose complexity limits direct observation or controlled experimentation. The neuromuscular response to repeated voluntary activation is an attractive target for this approach Due to the fact that joint torque, the common outcome measure of many studies of neuromeuscular function is itself the result of a series of interrelated physiologic processes. Here, we present a

comprehensive model of neuromuscular activation, torque generation, bioenergetics, and fatigue in order to provide a means to study the relative impact of several of the physiological processes thought to underlie the fatigue process. Forward integration was used to calculate the output of a series of modular components, each meant to represent a component of neuromuscular function. The models output was compared with in vivo data from the literature.

This approach to modeling activation, torque generation, and metabolic response provides a novel means of investigating the mechanisms of fatigue during repeated voluntary contractions. Specifically, this model predicts the neural, contractile and bioenergetic responses to voluntary activation during repeated, brief (12s) contractions. The model's strength and potential to provide insight is due to the fact that none of its components operate independently. The process of model formulation and subsequent validation provide valuable information regarding the relative impact of these multiple components to overall fatigue, and the mechanism(s) regulating human neuromuscular fatigue.

Introduction

The mechanisms of skeletal muscle fatigue involve multiple physiological systems (48; 186) and are task-specific (86). Our understanding of the fatigue process has benefited from years of in vivo and in vitro experimentation, during which numerous insights into both cellular and systemic influences on force-generating capacity have been attained. However, both in vitro and in vivo methodologies have some inherent limitations. In vivo experiments are typically challenged by a lack of control over interrelated processes that may be difficult to measure. In vitro experimental conditions, while more tightly controlled, cannot mimic the complexity of in vivo systems. In either case, the ability of researchers to simultaneously quantify the multiple mechanisms that contribute to a loss of force-generating capacity is somewhat compromised.

The mechanisms of fatigue often are referred to as either central or peripheral in nature. The term "central fatigue" is used to describe a range of neural responses to contraction that ultimately reduce the ability to excite skeletal muscle voluntarily (173). Reduced excitation of α motor neurons results in reduced maximal discharge rates for active motor units, and/or derecruitment of motor units, beginning with those with the highest activation thresholds (98). Peripheral fatigue mechanisms refer to those events occurring distal to the central nervous system. These include reduced excitability of the sarcolemma (51; 61), slowed Ca^{2+} kinetics, and decreased sensitivity of thin filament proteins (Troponin C, T, I, and, Tropomyosin) to Ca^{2+} (33; 50). It is likely that both central and peripheral mechanisms contribute to fatigue during maximal contractions in vivo (173).

The byproducts of intracellular, metabolic processes that maintain [ATP] in the face of changing energetic demands have been implicated in the development of fatigue during repeated or prolonged contractions. Repeated contractions of sufficient intensity will increase intracellular [ADP], [Pi] and [H$^+$] which have been implicated in fatigue processes (106). Through multiple mechanisms, each of these metabolites alter the behavior of the cross-bridge. Their combined effect ultimately lowers force, rates of relaxation, and possibly shortening velocity (49). While in vitro evidence also suggest roles for these metabolites in the reduction of force-generating capacity, the extent to which these in vitro findings reflect the behavior of the intact neuromuscular system is not always clear. Data from in vivo studies finds inconsistent effects of metabolites such as H$^+$ and ADP (106; 156). However, most in vivo studies support a strong association between [H$_2$PO$_4$$^-$] and fatigue that persists under a variety of conditions (31; 103; 106; 111; 113; 135).

Direct, simultaneous measurement of intracellular metabolites, neural activation, and contractile mechanisms is difficult, particularly with sufficient temporal fidelity to make inferences regarding the mechanisms of fatigue. Computational modeling of muscle fatigue is appealing due to the inherent complexity of the physiological events involved in voluntary torque development and the dynamic relationships that exist between them. One of the earliest attempts to predict fatigue at a single joint using a valid muscle model came from Hawkins and Hull (74). They adapted a previously validated model of muscle force generation (75) to predict fatigue during prolonged activation. Despite a large number of assumptions and formulation that might be considered basic by more current standards, their model successfully predicted the rate

and total amount of fatigue during 60 seconds of maximal elbow extension. This significant contribution was one of the first computational models to predict voluntary fatigue and is augmented by their consideration of both activation and the differential response of multiple fiber-types (recruitment order, endurance time and fatigue rate).

Since Hawkins et al, (74) significant advances have been made in modeling the fatigue response. Several groups have used models to predict fatigue during functional electric simulation for clinical application in paralysis (42; 43; 62; 63; 118). Significant advances have been achieved under this paradigm, but most use electromyography, and its decrement during repeated activation, as an input signal to predict fatigue (40; 42; 118). Others have used metabolite concentration as a limiting function on force-generating capacity (62; 63; 118). This latter approach attempts to mimic the fatigue process in a way that is perhaps more representative of in vivo skeletal muscle function (62; 63; 118).

The present model combines a previously-validated, forward-dynamics model of neuromuscular function (Callahan et al, unpublished) with a recently developed model of metabolic perturbation, homeostasis and fatigue. By using a series of ordinary differential equations, the forward-dynamics model predicts neural, bioenergetic, and contractile responses to voluntary activation. A single stimulation signal served as the input for a number of independent models of motor neuron function, each corresponding to a Hill-type muscle model, complete with force-length, force-velocity, and bioenergetic parameters. The linear sum of forces predicted from each muscle model was input to a musculo-skeletal model of the ankle dorsiflexors, used to predict torque. The model was formulated primarily with metabolic and musculoskeletal data from the ankle dorsiflexor

muscles in a group of young adult males. The output from the model was then validated

by comparison with separate data from the literature (110; 134). The purpose of this

study was to adapt a previously-validated model (Callahan et al, unpublished) of

neuromuscular function and bioenergetics to respond to repeated activations, recover

metabolic homeostasis, and predict fatigue. To achieve our goal, we designed a system

of equations representing the neural excitation, muscle activation contractile kinetics, and

metabolic costs associated with the development of contractile force.

Methods

Computational Approach

The current modular approach is similar to the earlier model, with several

significant advancements, which represent neuromuscular function and bioenergetic

response to repeated activations, maintenance of metabolic homeostasis, and ultimately,

fatigue. The system of equations that dictate neural excitation, muscle activation,

contractile kinetics and metabolic costs associated with the development of contractile

force is similar to the previously validated model. However, the present model contains

the addition of functions describing efflux of H^+ in acidic conditions, the synthesis of

phosphocreatine (PCr) following contraction and a mechanism whereby $H_2PO_4^-$ limits

force-generating capacity. Model formulation and simulations were run using Matlab

software (MathWorks, Natick MA).

A forward integration routine with 0.001 s time resolution is used to predict the

output of each sequential step of the model. Each step is meant to represent a

physiological event in the pathway from cortical excitation to torque generation at the

ankle joint. These steps include central excitation, motor unit recruitment, muscle fiber

activation (sarcolemma depolarization and calcium release from the sarcoplasmic reticulum), muscle cell contraction, force summation, and, torque generation. These modeled steps are illustrated in Figure 1.

To summarize the steps of forward integration for the model, a single parameter meant to represent voluntary excitation (S, Step 1) to the spinal cord served as the input for a modeled pool of 60 motor units (Step 2). This simulated pool of α motor neurons largely followed a recruitment scheme originally proposed by Fuglevand et al (59). Excitation input was used to calculate the firing rate (FR) for each modeled motor neuron. An activation transient model follows (Step 3) and serves as the input for a Hill-type muscle model (Step 4). Periods of muscle activity and recovery following activation initiated further steps to model metabolic perturbation and restoration of homeostasis respectively (Step 4a: this step, unique to the current model, is described in greater detail below). The linear sum of forces produced by all muscle models was then used as the input for a musculo-skeletal model of the ankle joint to predict current joint torque (T_c) at the ankle (Step 5). Finally, T_c was compared with the a priori defined timeline of a torque task (T_t), which caused an adjustment of S such that the difference between T_c and T_t was minimized (Step 6). In this forward integration model, functions received no input beyond initial conditions and T_t. A detailed description of the equations for of each step can be found in Appendix D. The following is a general description of our approach to model parameterization and formulation, with emphasis placed on novel contributions of the current model to the previous iteration; namely the calculations related bioenergetics, intracellular metabolic homeostasis and fatigue (Step 4a).

Simulation Procedures

Multiple simulations were run to validate modeled predictions for the variables of interest ([Pi], [PCr], [$H_2PO_4^-$], pH, Torque). In order validate intermediate steps in the prediction of fatigue, contractions of 12s duration were simulated at 20%, 50% and 100% of maximum voluntary effort and compared with in vivo observations of the same. These simulations were run by setting T_t to 20%, 50%, and 110% of predicted maximum torque, and allowing the control function in step 1 of the model to moderate excitation. Simulations predicted a 300-s response in the case of the MVC, and 145s in the case of submaximal contractions, to allow for testing of recovery dynamics in the model. All simulations predicted data with 0.001s time-resolution. The model was run at varying levels of activation to ensure predictions for metabolic perturbation were accurate when activation was submaximal. This was especially important given the activation variable was the site targeted for manipulation during fatigue simulation trials.

To test fatigue prediction by the model, a simulation was run consisting of six 12-s contractions with 12s rest between them. This protocol was selected to match that of a recent study for comparison (113). The simulation ran for a total of 144s with 0.001s time resolution.

Source Data

Extensive effort was made to parameterize the model with experimentally-collected data from the same set of subjects for each variable. The model drew on published (110; 134) and unpublished data available from studies conducted in the Muscle Physiology and Biomechanics Laboratories at the University of Massachusetts,

Amherst. When necessary, model components and parameters were drawn from the literature, with a preference toward human studies when available.

Subject Characteristics

Young men (21 – 35 years, n = 8) were healthy by self-report, non-smokers, and at least recreationally active. Participants were familiar with torque measurement using a Biodex dynamometer (Biodex Medical Systems, Shirley, NY) and refrained from exercise on all testing days. Data collection from these participants included measures of muscle architecture from ultrasound (Siemens Munich, Germany), anterior compartment muscle volume and moment arm measures from magnetic resonance imaging (MRI; Siemens Munich, Germany) and metabolic flux through ^{31}P magnetic resonance spectroscopy (MRS) using a 4.0 tesla superconducting magnet (Bruker Biospin, Rheinstettn, Germany).   These methods have been described elsewhere (102).

Muscle Architecture

Measures of tendon stiffness, moment arm length, pennation angle and muscle volume were performed at the University of Massachusetts Amherst and Cooley Dickinson Hospital Imaging Facility in Amherst MA. Ultrasound imaging was used to measure the distortion of tibialis anterior muscle fascicles and tendon during progressive contractions to maximum voluntary effort while a subject was seated in the Biodex isokinetic dynamometer (72; 73; 175).

To measure muscle volume, serial sections of MRI were collected for the length of the lower leg (T1 weighted spin echo axial images; 4 mm slice thickness, 210 mm field of view, 512x512 matrix). Custom written Matlab software was used to separate the anterior compartment in each slice into contractile and non-contractile tissue based on

signal intensity. Total muscle volume was determined from measured cross sectional

area combined with the thickness of each slice.

Metabolic Perturbation and Homeostasis

As described previously (110; 134), ^{31}P MRS was used to observe the relative

concentration of metabolites during contraction and recovery with 4s time resolution.

Phosphocreatine (PCr) and inorganic phosphate (Pi) were measured in the dorsiflexors

using a 4.0 tesla superconducting magnet. The depletion of PCr, accumulation of Pi and

rate of ATP production through anaerobic glycolysis were measured during contractions

performed at a range of intensities (110; 134) in order to establish a relationship between

voluntary activation level and metabolic perturbation. Quantitation of phosphorus

containing metabolites was accomplished by line fitting of time-averaged spectra, using

NUTS software (Acorn NMR, Livermore CA). A stepwise approach to the formulation

of the functions that dictate metabolic perturbation were similar to those used in the

previous model formulation (Callahan et al, unpublished) and detailed in Appendix D.

Modeling Fatigue and Recovery

The present model augments previous simulations of neural activation and

metabolic perturbation by the inclusion of functions that predict the restoration of

homeostasis, allowing for the prediction of intracellular metabolic status during

intermittent contractions. Fatigue was dependent on the predicted accumulation of

$H_2PO_4^-$ through a negative, linear association between $[H_2PO_4^-]$ and activation (Step 3).

This is meant to reflect the relationship between $[H_2PO_4^-]$ and Ca^{2+} mediated force

generation observed in vitro (143). The model predictions for [Pi] and $[H^+]$ were based

on the activation dependent accumulation of Pi (equations 1 and 2, Appendix E) and

glycolysis (equations 25-32, Appendix D). Briefly, muscle activation level (Step 3, Figure 1) dictated coefficients that determined the rates of Pi accumulation during contraction. This rate was limited by the square root of the percent of PCr remaining during contraction:

$$(PCr/PCr_{rest})^{0.5} \qquad\qquad (1)$$

The model of glycolysis was based on the Michaelis-Menten relationship between [Pi] and glycogen phosphorylase (22), and predicted the rate of proton generation from this metabolic pathway. The K_m of the relationship was assumed to be 18.94 mM (22; 155). Protons were produced from non-oxidative glycolysis, consumed by the creatine-kinase reaction (rate of Pi accumulation) and buffered by several intracellular processes (see Appendix D).

Following contraction in which intracellular pH was more acidic than baseline values (pH = 7.05), [H$^+$] returned to baseline through a model of efflux. This calculation was based on measured values of proton efflux (179) and was expressed mathematically by the equation:

$$Efflux = E_{rate} \cdot^- pH^2 \qquad\qquad (2)$$

where E_{rate} was the linear rate constant for proton efflux (102) and $–pH$ was the difference between pH and baseline pH.

In vivo, ^{31}P MRS was used to monitor the recovery to baseline levels of [Pi] and [PCr] following contractions at each intensity level. Observed recovery rates of [Pi] and [PCr] were fit with a 3rd order exponential decay, or rise to maximum respectively. The first derivatives of these equations were used to calculate rates of change for [Pi] in the present model (equation 22b, Appendix D).

Experimental observation revealed that the recovery kinetics of [Pi] depended on the extent of [PCr] depletion, which contradicts previous reports (184). These effects were reflected in the model by adding a function that related the coefficients of post-contraction Pi recovery with the level of depletion (Equations 23 and 24, Appendix D). For a more complete explanation of these functions, and their derivation, see Appendix E. During recovery, [$H_2PO_4^-$] was calculated from [Pi] and pH at each time point according to the equation:

$$H_2PO_{4-} = Pi/(1+10^{(pH-6.75)})$$

(3)

Fatigue was modeled by using current [$H_2PO_4^-$] to limit activation (*act*) in the vector equations in the muscle model (see Appendix D). The limit on *act* (ActLim) was based on literature values (111) and expressed mathematically by the equation:

$$ActLim = -0.0175 \cdot (H_2PO_{4-} + 1.09275)$$

(4)

The quality of model predictions was evaluated principally by comparing the output of each simulation to our experimental contractile and bioenergetic data in the case of maximal and submaximal 12s contractions. Fatigue simulations were compared with literature values (113) for measures of fatigue.
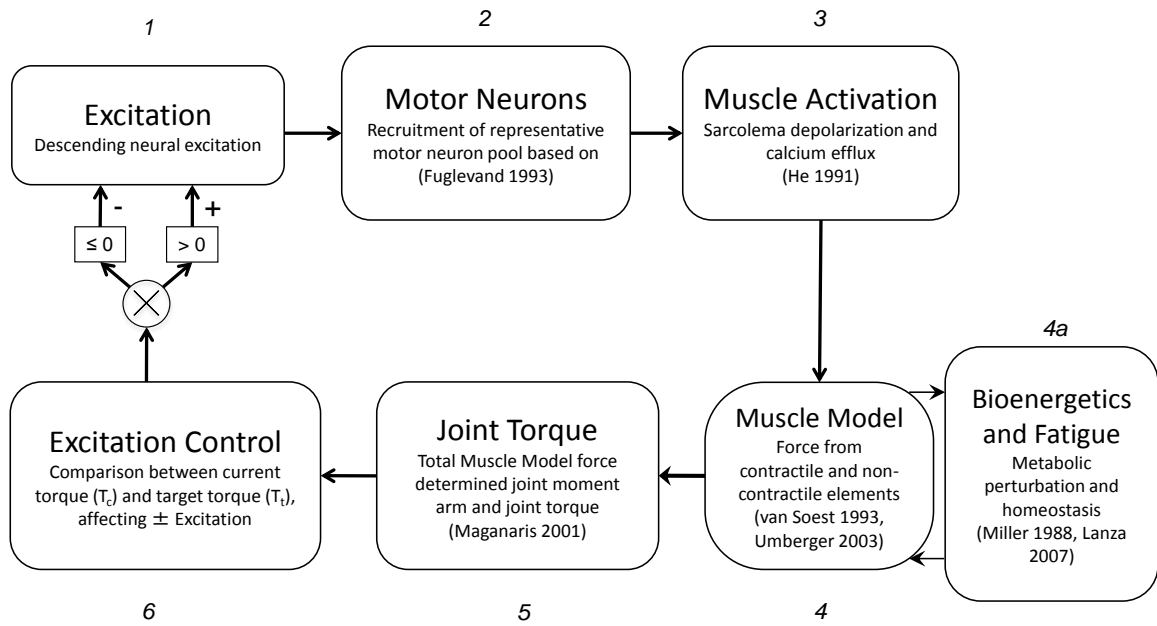
Figure 5.1. Computational approach. A block diagram is presented of each in the neuromuscular model, and the physiological events they are meant to represent. Source data used in each step are included in the appropriate block

Results

Results for a single maximal, 12s contractions and the 287s recovery period are illustrated in Figure 2. In all figures, modeled data are continuous (0.001 time resolution) but are sampled at 4s intervals for ease of comparison with in vivo data. Model predictions for the decrease in [PCr] and increase in [Pi] during the 12s contraction were accurate and well within the standard deviations of the experimental data. Similarly accurate predictions were made for intracellular pH and [$H_2PO_4^-$] during contraction. Following the contraction, modeled recovery rates of these metabolites matched well with the experimental data. Compared with in vivo measures, the model slightly under-predicted acidosis during the recovery period, and the kinetics of alkalosis and acidosis were slightly delayed. However, these differences were minor and the characteristic behavior of the intracellular metabolites was highly consistent with in vivo observations. Finally, predictions of [$H_2PO_4^-$] were similar to in vivo measures.

Results for single, submaximal contractions at 50% and 20% MVC are illustrated in Figures 3 and 4 respectively. Modeled metabolite concentrations were generally in good agreement with experimental data at 50% MVC (Figure 3). The exception was the prediction of pH following contraction. Although the model predicted contraction-induced alkalosis within the standard deviations of experimental values at this torque level, the model slightly over-predicted acidosis. Given the relatively minor change to pH in both modeled, and experimental data during recovery, this deviation from experimental values was not sufficient to alter predictions for [$H_2PO_4^-$], which compared

91

well with the experimental measures of this metabolite for the duration of both contraction and recovery periods.

At the lowest torque level, 20% MVC, model predictions for [PCr] and [Pi] were consistent with experimental data. The estimate of pH, while characteristically similar to the in vivo time-course, over-predicted acidosis during recovery. In fact, the experimental data revealed little to no net acidosis following contraction at this lowest force level. However, because the degree of predicted acidosis was minimal, it did little to upset predictions of [$H_2PO_4^-$], which aligned well with experimental data.

Overall, the changes in metabolites predicted by the model were well-approximated during and following single, 12s contractions. This result is critically important to the application of the model to simulations of repeated intermittent contractions, and the study of fatigue.

Simulation of the contractile and bioenergetic response of 60 MUs to 6 repeated, 12-s MVCs (Figure 5) was consistent with an independent dataset from the literature. Torque and pH ultimately fell, and [Pi] increased, as expected, and the magnitude of these changes were similar to those reported by Lanza et al (113). Torque was reduced to 79.1% of baseline, which compares well with the value of 74.2% reported in Lanza et al in vivo (113). The root mean squared difference (RMSD) of fatigue prediction was therefore 6.6%. The time-course and magnitude of changes in intracellular metabolites compared reasonably well with the experimental data reported by Lanza et al (113), (Figure 5). At the end of the repeated contractions, model simulations predicted [Pi] = 33.9 mM as compared with 32.6 ± 0.9 mM, a RMSD of 4.0%. End-exercise pH was somewhat less consistent with values in the literature. Lanza et al reported pH of 6.70 ±

0.03 at end exercise, while the model predicted pH = 6.81. When converted to absolute proton concentration (1.99 ± 0.14 and 1.55 mM, respectively) this reveals a 22.4% RMSD. Similar to the prediction of pH during a single contraction, acidosis was under-predicted by the model. However, the degree to which acidosis is under-predicted seems exacerbated during repeated simulated contractions.
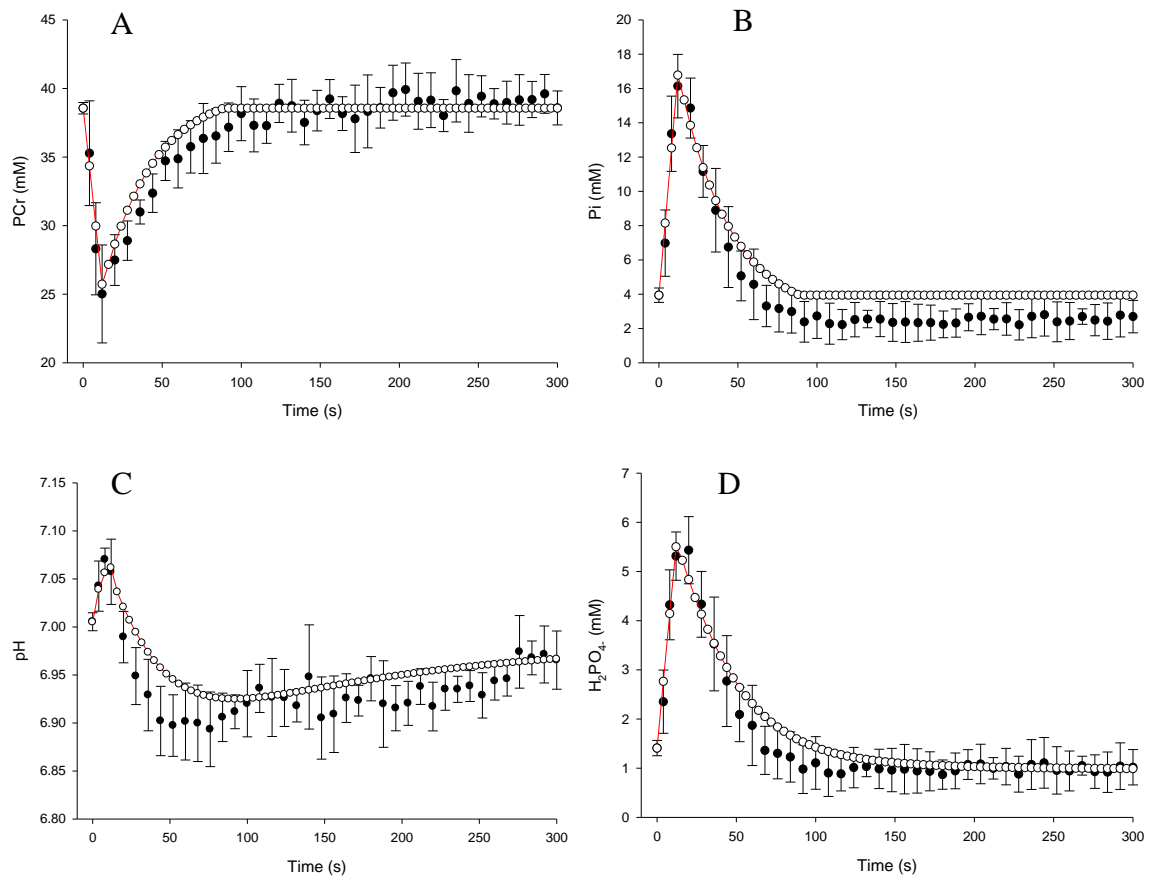
Figure 5.2 Maximum voluntary contraction and recovery. Simulated (open circles, grey line) and in vivo (closed circles ± SD) data corresponding to phosphocreatine (PCr, A), inorganic phosphate (Pi, B), pH (C), and $H_2PO_4^-$ during a 12s maximum voluntary contraction and subsequent return to homeostasis
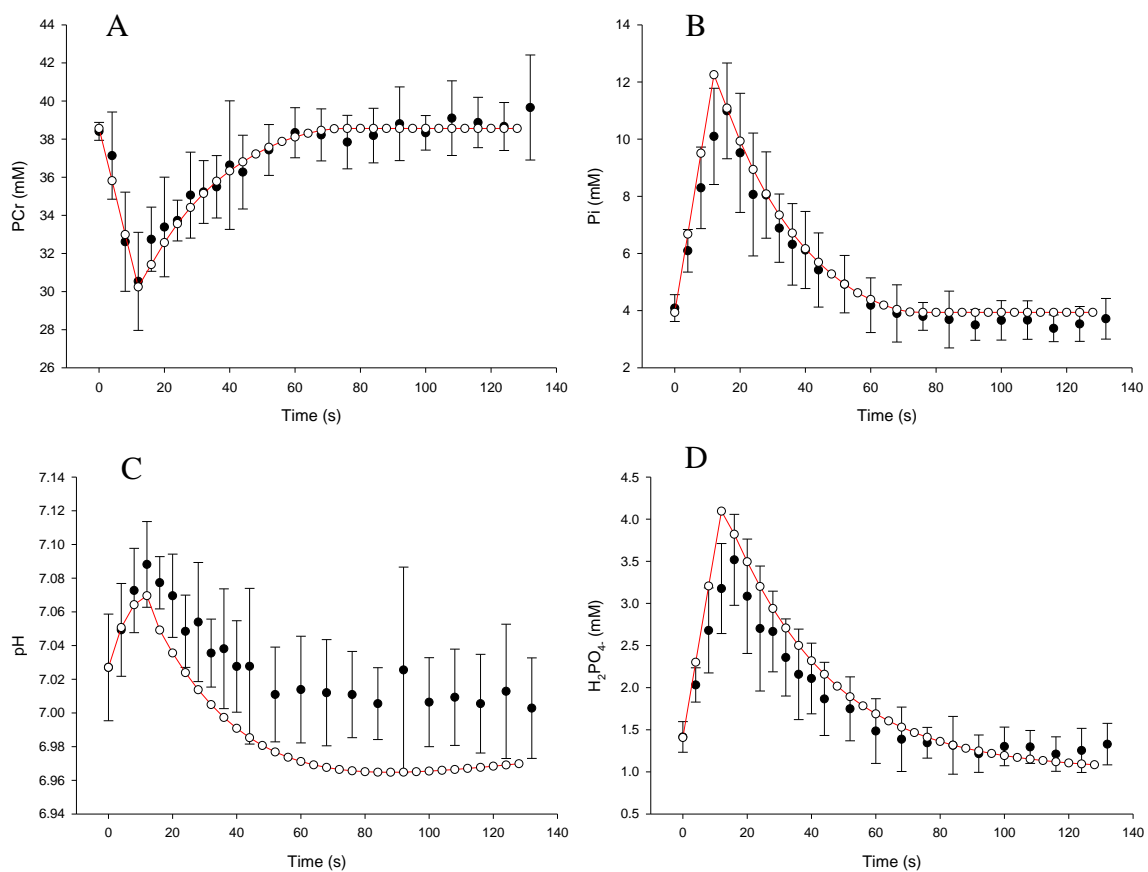
Figure 5.3 50% Maximum voluntary contraction and recovery. Simulated (open circles, grey line) and in vivo (closed circles ± SD) data corresponding to phosphocreatine (PCr, A), inorganic phosphate (Pi, B), pH (C), and $H_2PO_4^-$ during a 12s contraction (50% MVC) and subsequent return to homeostasis
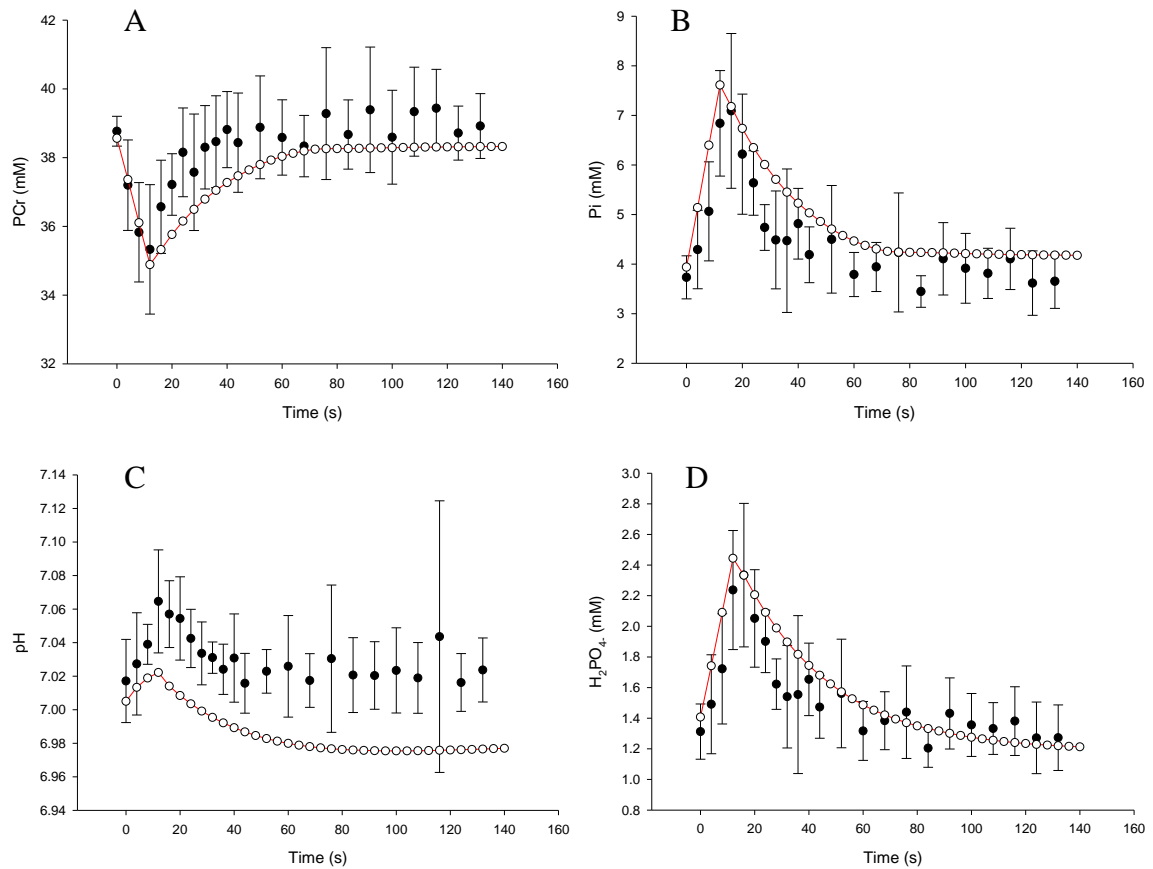
Figure 5.4 20% Maximum voluntary contraction and recovery. Simulated (open circles, grey line) and in vivo (closed circles ± SD) data corresponding to phosphocreatine (PCr, A), inorganic phosphate (Pi, B), pH (C), and $H_2PO_4^-$ during a 12s contraction (20% MVC) and subsequent return to homeostasis
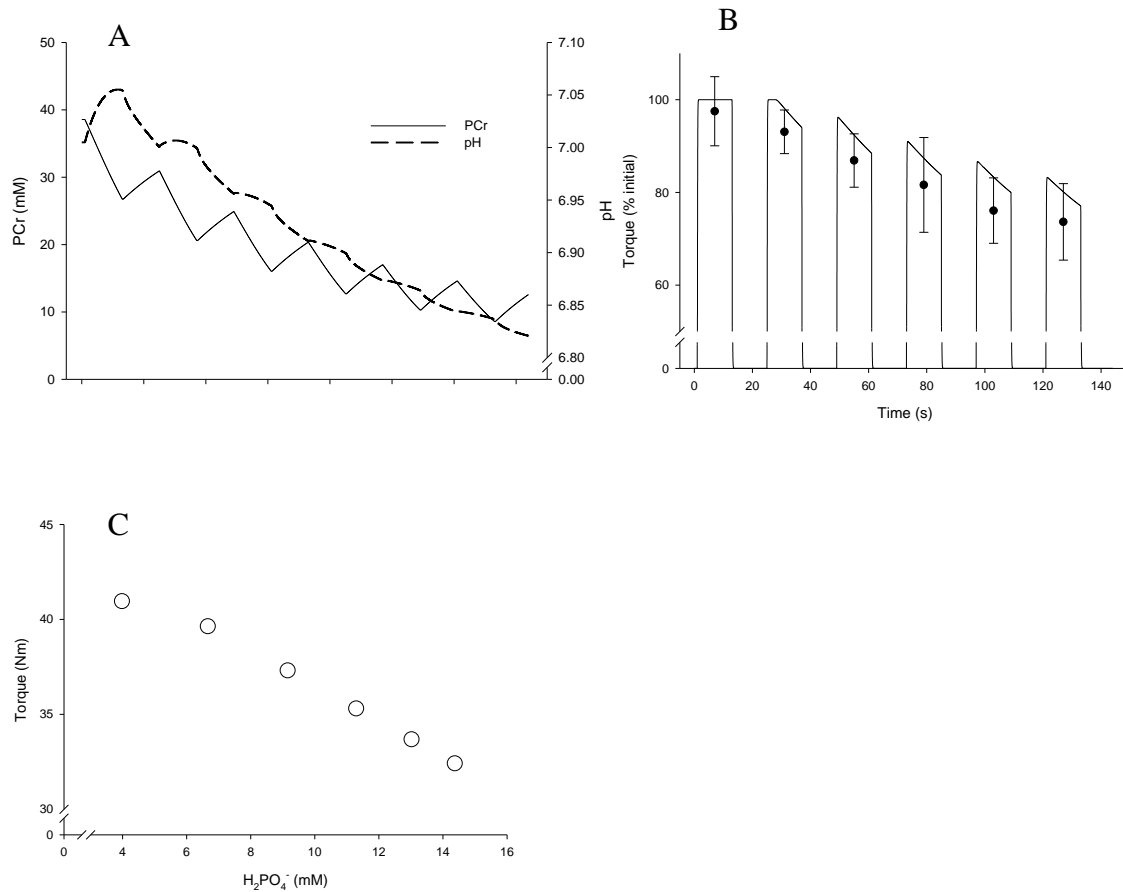
Figure 5.5 Simulated repeated 12s contractions. Simulated intracellular [PCr] and pH during 6 repeated 12s MVC (A). Continuous (0.001s) simulated relative torque (solid black line) and in vivo relative torque (time tension integral) from young men (closed circles ± SD) from Lanza et al (111; 113) (B). Average torque

Discussion

Model Predictions

The model presented here accurately predicts voluntary activation, torque production, metabolic perturbation, and return to homeostasis during single and repeated contractions in the ankle dorsiflexor muscles. These results have been confirmed by comparison with experimental data. Both overall (fatigue) and intermediate (intracellular metabolic status) model predictions (Figures 2, 3 and 4) were found to be consistent with results in the literature (Figure 5). A novel feature of this model is the capacity to predict metabolic recovery and thereby allow investigation of fatigue during repeated contractions. By associating $[H_2PO_4^-]$ with limitations in the molecular basis of muscle force generation (36) the model predicts changes in torque and intracellular metabolites during repeated activation that are characteristically similar to those measured in vivo. This was accomplished computationally by limiting the capacity for calcium-mediated activation (equation 3), (143). The model therefor provides a novel tool for testing hypotheses related to fatigue resistance and intracellular bioenergetics.

Overall fatigue in our model was less than that observed by Lanza et al (113) using the same contraction protocol. However, it should be noted that the subjects whose data were used to parameterize the present model were more active, and potentially more fit than the cohort of Lanza et al (113). Indeed, kPCr, an indication of the in vivo oxidative capacity of voluntary contracting muscle, was reported as 0.036 in Lanza et al, markedly lower than the value predicted from the modeled data (0.044). This greater capacity to synthesize PCr following MVC would result in predictions of less Pi accumulation, lower glycolytic rates, and overall lesser $[H_2PO_4^-]$ and fatigue.

The prediction of less acidosis and fatigue during repeated contractions compared with in vivo data, despite similar depletion of PCr, highlights a potential limitation in the present model. Faster PCr recovery kinetics in the model compared with in vivo data will affect pH predictions by limiting the overall load of Pi, and thus calculated rates of glycolysis. However, the control of glycolysis in vivo is influenced by a number of factors (32; 109) not expressed in the present model. While our predictions for glycolytic flux match well with experimental data, our phenomenological model of glycolysis is admittedly simplified, and may contribute to inaccuracies in model estimates.

Mechanisms of Fatigue

In the present application, fatigue was simulated by limiting the activation signal in step 3 of the model based on [$H_2PO_4^-$]. This approach was used as it relied on the least number of assumptions and was supported by substantial evidence in the literature (143) (2). During activation, force generation depends on binding of the acto-myosin complex in its strongly bound configuration, which is preceded by the dissociation of Pi. Because these reactions occur in equilibrium within the sarcoplasm, increased cytoplasmic [Pi] may decrease its rate of dissociation from the acto-myosin complex, and thus, reduce the number of cross-bridges linked in a strongly-bound configuration.

Elevated [H^+] depresses cross-bridge force in vitro, regardless of saturating levels of Ca^{2+} (132), suggesting it has independent effects on cross-bridge force generating capacity (46). Some investigators have observed an inverse, linear relationship between [H^+] and force-generating capacity (106). However, during recovery from fatigue, hysteresis is evident in this relationship, indicating that if [H^+] is directly mediating fatigue, its relationship with force-generating capacity is not constant. It seems likely

that $[H^+]$ has an associative, rather than causal relationship with reduced force production in vivo.

Several investigators have observed associations between $[H_2PO_4^-]$ and skeletal muscle fatigue (31; 103; 106; 111; 113; 135) which seem more robust than associations between $[H^+]$ and fatigue alone. Increased $[H_2PO_4^-]$ during contraction reflects increased intracellular $[Pi]$ and $[H^+]$ that result from the creatine kinase reaction and glycolysis, respectively. Multiple studies have demonstrated a linear association between $[H_2PO_4^-]$ and fatigue (31; 106; 111; 113; 135). The correlation between fatigue and $[H_2PO_4^-]$ persists during ischemia and is consistent, whether fatigue is induced by intermittent or sustained contractions (135).

It has been suggested that the strong relationship between fatigue and $[H_2PO_4^-]$ is lost during repeated bouts of dynamic contractions (156). In light of this observation, and given the myriad influences on voluntary force-generating capacity, it seems unlikely the entirety of the fatigue process can be ascribed to a single metabolite. However, the variety of conditions under which $[H_2PO_4^-]$ correlates with losses in force highlights its utility as a strong predictor of fatigue during isometric contractions.

In vivo, skeletal muscle fatigue during intermittent contractions is likely due to both peripheral and centrally-mediated changes in neuromuscular function. Signals from group III and IV afferent nerve fibers, sensitive to the accumulation of intracellular metabolites, contribute to diminished cortical excitability, as well as increased α motor neuron inhibition (18; 172). However, central mechanisms of fatigue seem to play the greatest role during prolonged, submaximal, and maximal isometric contractions (31; 103; 106; 111; 113; 135; 191), and a lesser role during intermittent maximal contractions

(20; 112; 125). The present model relied on a purely peripheral mechanism (limits to activation at step 3) to predict fatigue. This mechanism was chosen based on the greatest volume of experimental in vivo evidence supporting this mechanism, including recent investigations using rat (124) and murine models (1). Future applications of the present model might investigate the relative impact of varying the contribution of central (Step 2) and peripheral (Step 3, Step 4) mechanisms. However, the focus of the current application was to validate the model's initial predictions. As such, further manipulations were deemed beyond the scope of this project.

Current Insights and Future Directions

Our accurate prediction of bioenergetic and fatigue responses to repeated voluntary activations provides some encouragement for the use of the present model in future applications that might answer questions related to the mechanisms of skeletal muscle fatigue in vivo. While additional studies are needed, the data presented here provide some insight as to the mechanisms of fatigue, and the nature of the assumptions related to the energetic response to voluntary activation and torque production.

The range of glycolytic potential assigned to muscle models within our 60-motor unit pool, and how these might respond to varying activation levels, provides a modifiable variable related to the mechanisms of fatigue. The ranges expressed by the present model are within those reported in vivo (113; 183) and were selected specifically to reflect the overall average glycolytic potential observed during maximal voluntary activation (113). It should be noted however, that other combinations of values could be used to arrive at the same average for the total pool. Evidence in the literature supports a fairly narrow range of glycolytic potential across human muscle fibers (162), similar to

the 4-fold range described in the model. In the low-intensity (20% MVC), experimental contractions used as the basis of our model formulation, little post-contraction acidosis was observed, suggesting limited glycolytic flux during activation of low-threshold motor units. This might be explained by a pool of motor units with a low capacity for non-oxidative glycolysis. However, such a pool would contradict the narrow range of glycolytic potential typically reported in human muscle.

Glycolytic flux is one of several variables used to calculate pH at each time point in the model. As such, much can be gleaned from interpretation of model variations necessary to approximate observed values for pH. While our estimates of glycolysis, PCr depletion, Pi accumulation, and buffering capacity were within the standard deviation of our experimental means during single, 12-s contractions, subtle differences in each variable might impact our prediction of pH significantly. This is especially relevant during simulation of prolonged, repeated contractions. The kinetics of recovery of homeostasis are generally slower than those for depletion during activation. As a result, the first in a series of contractions is the only instance during these simulations where metabolite concentrations were equal to resting values obtained experimentally. Any prediction error will potentiate as periods of activation are repeated. Further, the interrelated nature of equations used to predict intracellular status of the muscle model permits an inaccuracy in one function to cause inaccuracy in others (Pi impacting glycolysis and pH, for example).

The dynamic range of buffering capacity used during the simulation, which depended on current [Pi], pH, and inherent buffering capacity was a physiologically relevant prediction provided by the model. Values for inherent buffering in skeletal

muscle vary widely in the literature (99; 110; 183). Here, inherent buffering in was set to

5 mM/pH unit after optimizing for the most accurate pH response to contraction across

contraction intensities. A similar routine was performed for the calculation of buffering

from Pi and the proton stoichiometry coefficient θ, a coefficient that determines protons

consumed or produced via the creatine kinase reaction (equation 30, Appendix D).

Although these values are within the range reported in the literature (99), further analysis

could be performed to determine the relative impact of each variable on overall

predictions of intracellular pH. In the present application, these variables were optimized

to increase predicted variation in pH to more closely match in vivo measures. Reducing

inherent buffering capacity, while increasing the buffering due to Pi, effectively increased

the drop in pH observed following contraction, while allowing for accurate predictions

during activation. These adjustments may be used to provide insight to many

assumptions made during calculations of intracellular metabolic status from ^{31}P MRS

data.

   Overall, our model approximated the torque and metabolic responses to repeated

maximal contractions as reported in the literature (113). These predictions were based on

a model whose functions were derived from in vivo measures of musculoskeletal

architecture, torque, and metabolic perturbation during relatively brief, single

contractions at varying torque levels in a young, male cohort, and validated by

comparison with an independent data set from the literature. This model represents a

significant step forward for the field of computational modeling, based on its high level

of integration, simplified control structure, and accuracy in predicting a wide range of

variables.

The current formulation and simulation results suggest an important role for peak oxidative capacity in fatigue resistance. This assumption is based on the sensitivity of fatigue predictions to variation in the recovery kinetics of PCr and Pi. Informal sensitivity analysis indicated that these kinetics had a greater impact on fatigue than other potential factors, like glycolytic rate and buffering capacity. Although in-depth analysis of these assumptions were beyond the scope of present work, future applications will include formal sensitivity analysis to determine the relative impact of different indices of neuromuscular function on fatigue.

In addition, the interaction of modules in the present model might be manipulated to test hypotheses related to identifying the physiological sites of fatigue development. For example, multiple computational strategies might be used to reduce force-generating capacity in the model. Future iterations of the present model might use intracellular metabolic status to inhibit MN recruitment, and thus effectively emulate central activation failure. Similar reductions to each muscle model *fmax* would characterize in vitro evidence for a direct inhibition of actin-myosin binding and subsequent force generation. Further, ample in vivo evidence would support a slowing of activation and contractile kinetics during repeated contractions, and the present model is a unique platform to investigate their impact on fatigue during voluntary activation. Indeed, several components of the present model, now validated, provide excellent targets for future evaluation.

Acknowledgements

CHAPTER 6

EFFECTS OF AGE ON NEUROMUSCULAR FUNCTION: MODELING AGE-RELATED FATIGUE RESISTANCE

Abstract

Strong evidence exists to suggest that the muscles of older individuals fatigue relatively less than their younger counterparts during either prolonged or intermittent isometric contractions. However, due to the many differences in neuromuscular function between young and older humans, it is difficult to ascertain the physiological mechanisms of age-related fatigue resistance in vivo. Reduced maximal motor unit discharge rates, a relatively greater abundance of slow, type I muscle fibers, and differences in bioenergetic properties all may contribute to the phenomenon of age-related fatigue resistance. Although models have been developed that predict fatigue in response to repeated activations, and others have been designed to predict altered function with old age, no model has been designed to examine age-related changes of the neuromuscular system in the context of fatigue. We present a comprehensive computational model of neuromuscular function that significantly extends previous efforts to emulate multiple facets of neuromuscular function during repeated voluntary contractions. In our present application, we test the validity of a model of neuromuscular function specifically tuned to highlight age-related differences in neuromuscular function that may play a role in the relative fatigue-resistance demonstrated by older adults compared with young adults. By simulating repeated maximum voluntary contractions, similar to protocols used to test fatigue in the literature, we demonstrate the sensitivity of

the model to age-related differences in neuromuscular function. The model predicted

fatigue responses similar to those observed in vivo, and importantly, lesser in magnitude

than those predicted by a model parameterized with data collected in a group of young

individuals. These findings validate the present model as a unique and powerful tool for

testing hypotheses related to the phenomenon of age-related fatigue resistance.

Introduction

Evidence in the literature suggests that skeletal muscle fatigue, the acute decline in force-generating capacity that accompanies repeated or prolonged contraction, occurs to a lesser extent in the muscles of older adults than in young adults (24; 174). Age-related fatigue resistance has been reported by a number of labs under a variety of experimental conditions (20; 21; 25; 44). However, others have reported the opposite (10; 149) and there is some controversy regarding the extent and prevalence of this phenomenon. Recent analyses suggest that age-related fatigue resistance least often observed during dynamic contractions, and most frequently observed during sustained (11; 88; 125) or intermittent (25; 44) isometric contractions (24; 174). Several mechanisms have been proposed to explain age-related fatigue resistance, including alterations in motor neuron behavior (4; 174), greater reliance on oxidative metabolism (106), increased metabolic economy (80; 111) and reduced generation of fatigue-inducing metabolites (23; 26).

The interrelated nature of the physiological processes thought to influence fatigue makes their influence difficult to discern in vivo. Quantifying the extent to which these processes differ between younger and older individuals and further, how they might mediate age-related differences in fatigue is an even greater challenge. While in vitro experimentation can provide explicit details about isolated systems, and in vivo studies typically describe the combined function of multiple systems, each are limited in addressing the phenomenon of age-related fatigue resistance. Model simulations, on the

other hand, can be used to predict the responses of complicated systems whose interrelated components preclude direct measurement or control.

Computational modeling has emerged as an attractive means of using what is known about isolated systems to predict their behavior when combined. Models have been developed that successfully predict the function of multiple bio-physical systems, ranging in focus from nervous tissue (77) to individual sarcomeres within skeletal muscle (91). Although models have been developed that predict fatigue in response to repeated activation (62), and others have been designed to predict altered function with old age (175), no model has been designed to examine age-related changes of the neuromuscular system in the context of fatigue. Previously, we have presented a comprehensive model of neural activation, contractile dynamics, bioenergetics and fatigue (Callahan et al, unpublished). Adapting this model to reflect what is known about age-related changes to the neuromuscular system would allow for testing of hypotheses related to age-related fatigue resistance that are impossible to evaluate in vivo. Our approach was to focus on those aspects of neuromuscular function that are 1) known to differ between young and older adults, and 2) thought to play a role in the loss of force-generating capacity that is the hallmark of neuromuscular fatigue. The goal of the present study was to adapt a model of neural activation, contractile properties and bioenergetics (Callahan et al, unpublished), to make valid predictions regarding age-related fatigue resistance and the attendant physiological responses observed during repeated voluntary contractions in vivo. To accomplish this goal, variables related to contractile kinetics, activation, motor-neuron discharge behavior and bioenergetics were altered from our previously-validated model of neuromuscular function. The combined outputs of these functions were tuned

109

to ensure accurate prediction of neuromuscular function obtained experimentally in the ankle dorsiflexors of older men. The overall prediction of fatigue in older adult men was validated by comparison with an independent data-set available in the literature.

Methods

Computational Approach

A comprehensive model of neuromuscular function, formulated using literature values and in vivo experimental data collected from healthy young men was adapted for application to the study of aging. Adaptations to the original model (Callahan et al, unpublished), referred to here as "Young model", was accomplished by synthesizing results from the literature and a locally available data-set concerning intracellular metabolic data from the muscles of a group of older, healthy men. The modified model is referred to as "Old model" in this document. The overall computational approach is identical to that proposed previously with significant adjustments made to the computation of metabolic perturbation and return to homeostasis, glycolytic capacity, motor neuron recruitment and discharge properties, and contractile characteristics. These alterations were made for the model to emulate age-related changes in the neuromuscular system thought to contribute to the phenomenon of age-related fatigue resistance (24; 174). Steps in the forward integration model are identical to previous iterations. These steps are illustrated in Figure 1. Those steps altered to reflect age-related changes in neuromuscular function, are highlighted with dashed lines.

Briefly, the steps of forward integration began with a single parameter meant to represent voluntary excitation (S, Step 1). This value serves as the input for a modeled

pool of 60 motor neurons (Step 2) which closely follows a model by Fuglevand et al (59) and predicts a firing rate (FR) for each simulated neuron. A calcium transient model of activation followed (Step 3) and provides input into a standard Hill muscle model (Step 4). Integrated with the muscle model were calculations related to metabolic perturbation and return to homeostasis (Step 4a). At each stage, this cellular metabolism model interacted with the muscle model by affecting activation from step 3. The linear sum of forces produced by all muscle models was then used as the input for a musculo-skeletal model of the ankle joint which predicted current joint torque (T_c) at the ankle (Step 5). Finally, T_c was compared with a priori defined timeline of a torque task (T_t) which caused an adjustment of S such that the difference between T_c and T_t was minimized (Step 6). In this forward integration model, functions received no input beyond initial conditions and T_t. A detailed description of the equations that dictate the outcome of each step can be found in Appendix D.

Model Characteristics

Our previously validated Young model was parameterized using intracellular metabolic, and musculoskeletal data from a group of healthy young men (21 – 35 years, n = 8). Physical activity habits ranged from recreationally, to competitively athletic within this group. A complete description of data collection has been outlined previously (Callahan et al, unpublished).

Data similar to those obtained in this single cohort for the Young Model were available in a sample of older men (65 – 80 years, n = 9). These data were collected as part of a larger study of age-related changes in cellular metabolism and did not participate in measures of tendon stiffness. Participants where healthy by self-report, relatively

sedentary and did not smoke. Consent from older participant's primary care physician was obtained prior to participation. A schematic of modeled steps they used to formulate simulated output is shown in Figure 1. Those steps that were modified from the previously validated model are indicated by dashed lines in the Figure. The following sections describe the steps that have been modified in the present application in greater detail.
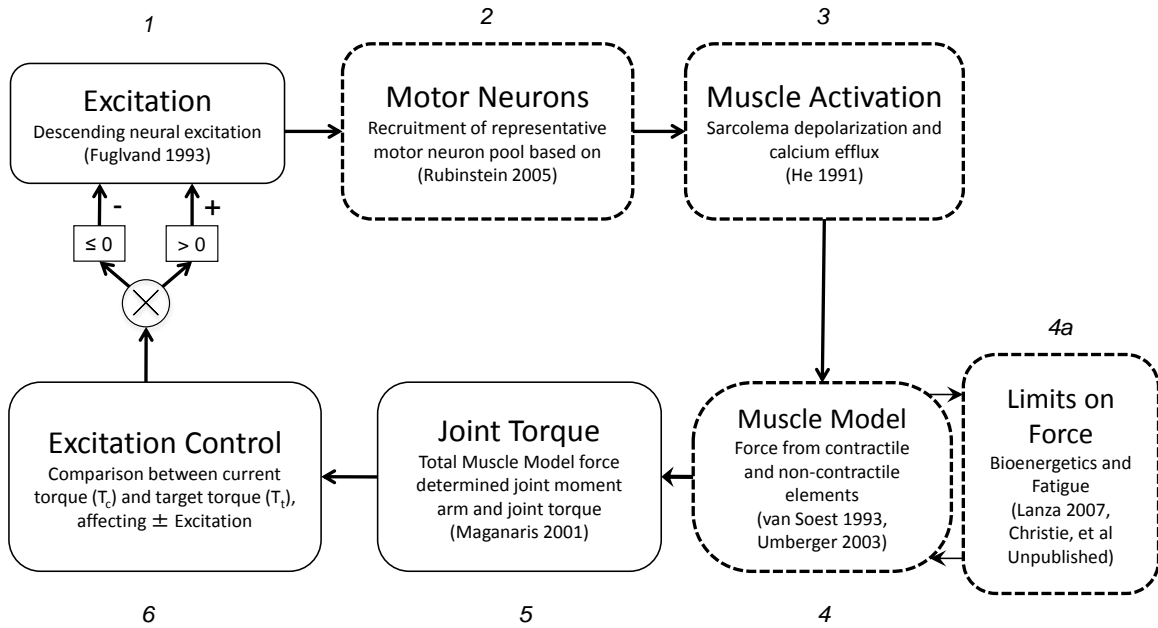
Figure 6.1. Computational approach and literature sources for model components. Components with dashed lines (2, 3, 4, and 4a) were modified from a previously validated version of the model (Callahan et al, unpublished) to reflect age-related changes in those aspects of neuromuscular function

Model Parameters

Model steps related to the forward integration of pertinent variables are outlined in Appendix D. Detailed description of the derivation of modeled steps related to bioenergetics is described in Appendix E. The focus of the present analysis is on those parameters that were altered to reflect age-related changes in neuromuscular function. While the characteristic behavior of functions described in Appendices D and E are consistent between the Young model and Old model, coefficients defining their range and kinetics were altered to ensure model predictions for their respective output matched in vivo observations. Portions of the model that were adapted to differentiate the Old model from the Young model included the motor neuron pool, contractile kinetics, metabolic perturbation and the musculoskeletal model. A more detailed discussion of model alterations follows.

Motor Neuron Pool

The modeled pool of motor neurons (MN), was adjusted to reflect changes in discharge properties of alpha motor neurons of older adults. Peak discharge rates for recruited motor neurons were reduced from 56 in YM, to 45 (160). The range of peak firing rates across 60 simulated MN was also limited from 10 to 8 (160). Minimum firing rate was set to 8 Hz, gain for activation (gain = 2) and activation thresholds (equations 9-11, Appendix D) were identical to the Young model.

Activation Kinetics

The equations defining activation and deactivation kinetics were altered slightly from those previously based on He et al (76). Evidence for age-related changes in

activation kinetics are largely inconclusive. It is possible that muscle fiber type

dependent rates of calcium efflux (19) may lead to an overall slowing of activation in

older adults based on a relatively greater population of type I muscle fibers. To reflect

this, the average time constant for activation (60 ms) was not changed, but the range of

activation time constants was reduced from 35% to 25%. In contrast to the limited

evidence for age-related changes in activation kinetics, ample evidence supports the

notion of prolonged deactivation. Slowed calcium uptake from the cytosol varies by

muscle fiber type (170) but is thought to be high as 35% (89) in humans and higher in

rats (139). This slowing of deactivation was described mathematically by Thelen at el

(175) and has been accomplished here by a similar increase in the average deactivation

time constant from 92 ms (Young model) to 120 ms (Old model). Further revision of the

model included a subtle increase in the "on" transient period of the Ca^{2+} signal (see II,

Appendix D). This was done primarily to ensure the model was capable of achieving

complete activation, despite lower motor neuron firing rates.

Contractile Kinetics

Several variables were altered in OM to reflect age-related changes in contractile

characteristics when compared to YM. These alterations are listed in Table 1.

Contractile slowing is frequently observed in vivo (4; 174). Often, this slowed rate of

force development during isometric contractions, as well as in dynamic tasks, is

attributed to altered fiber type distribution (116) and age-related contractile slowing that

occurs within fibers of the same type (144). In our approach, this contractile slowing was

expressed across the population of muscle models (MM), each of which corresponds to,

and receives its activation signal from one of 60 MNs. These were coordinated such that

115

the earliest recruited, MN corresponded to the slowest, least force-fully contracting MM_1.

While MM_1 had similar maximum shortening velocities (Vmax) to MM_1 in YM, Vmax in

the muscle model associated with the highest threshold motor neuron (MM_{60}) was

reduced by 12.5% compared with MM_{60} in YM. Because the distribution of forces

generated by these models was not linear, the overall Vmax of all muscle models was not

equal to the average of the range. The average of Vmax, weighted according to muscle

force-generating capacity (expressed in terms of optimum contractile element lengths

[L_{ce}^{o}] per second) was 16.43 L_{ce}^{o} in YM and 14.84 L_{ce}^{o} in OM. This reduction in Vmax

was somewhat less than the 20% reduction modeled by Thelen et al (175), but yielded

appropriate torque-frequency relationships when compared to our experimental data

(Figure 2).

Table 6.1. Age-Related Changes to Contractile and Activation Kinetics

		MM_1	MM_{60}	*Weighted Average*
Fmax	*Young*	0.57	54.51	28.06
(N)	*Old*	0.53	50.73	26.11
Vmax	*Young*	12.00	18.00	16.43
(L_{ce}^{0})	*Old*	12.00	15.75	14.84
***t*deact (ms)**	*Young*	92	64.6	70.2
	Old	120	84.3	91.6
***T*act (ms)**	*Young*	60	39	43.4
	Old	60	45	48.2

Contractile element (CE) parameters: Maximum force-generating capacity of (Fmax); maximum shortening velocity (Vmax); deactivation time constant (*t*deact); activation time constant (*T*act). Data are presented for the Young and Old parameters of the muscle model. To illustrate the range within each variable across the range of muscle models (MM), values are shown for the 1st (MM_1) and last (MM_{60}) individual muscle models within the overall model.

In addition to alterations made to the range of Vmax within the contractile element of the model, maximum force generating capacity (*fmax*) was reduced by 4.55%. This alteration was based on a similar reduction in anterior compartment muscle cross sectional area observed experimentally (unpublished observations).

Bioenergetics

Several alterations were made to the model of metabolic perturbation and return to homeostasis. The changes were made based on a combination of literature values and experimental observations using ^{31}P MRS.

Changes to phosphocreatine (PCr) and inorganic phosphate (Pi) kinetics were based on experimental data from older males, described above. Functions related to the kinetics of metabolic perturbation and returns to homeostasis were formulated in a procedure similar to that used in the Young model, and outlined in Appendix F. Important distinctions between the Young and Old model are also reviewed in Appendix F. Briefly, ^{31}P MRS was used to observe the relative concentration of phosphorus containing metabolites during contraction and recovery with 4s time resolution. PCr and Pi were measured in the dorsiflexors using a 4.0 tesla superconducting magnet (Bruker Biospin, Rheinstetten, Germany). The recovery of PCr following a 12-second maximum voluntary isometric contraction (MVC) was used to calculate the in vivo capacity for oxidative phosphorylation; kPCr (110; 134). The rate of ATP production through the creatine kinase pathway and anaerobic glycolysis were calculated for contractions at a range of intensities (20%, 50%, and 100% MVC) to better characterize the relationship between force, activation, and metabolic perturbation. Quantitation of phosphorus containing metabolites was accomplished by line fitting of time-averaged spectra, using

117

NUTS software (Acorn NMR, Livermore CA). Based on these data, model functions were created to reflect the cost of force production and the subsequent change in pH across a range of activation levels (See Appendix C).

As with the Young model, glycolytic rates were based on the Michaelis-Menten relationship between Pi and glycogen phosphorylase. The K_m of this reaction was set to 18.94 mM (22) in both the Young and Old model. While a similar, 4 fold range in capacity was modeled in both the Young and Old model, the weighted average of peak glycolytic rates of ATP synthesis were reduced from 1.50 ATP·s^{-1} to 0.74 ATP·s^{-1} in the Old model. This magnitude of age-related reduction in glycolytic flux during voluntary isometric contractions is consistent with values reported in the literature (111).

Simulation Procedures

To test the validity of model predictions concerning excitation and contractile dynamics in an aged neuromuscular system, a simulation routine was run meant to emulate traditional force-frequency analysis in vivo. Briefly, a train of "stimuli" were simulated by setting $S = 1$ for the first 0.029 s of the simulated period between motor neuron firings. For a given simulation, this duration was constant and depended on stimulation frequency. The results of these simulations were compared with in vivo measures, and previous model output.

To test the model's ability to predict torque, activation, and metabolic response to voluntary activation, contractions of 12s duration were simulated at 20%, 50% and 100% of maximum voluntary effort. These simulations were run by setting T_t to 20%, 50%, and 110% of predicted maximum torque, and allowing the control function in step 1 of the model to moderate excitation. In the simulation of MVC, T_t was set to 110% to

ensure T_c was always $< T_t$, thus ensuring maximal stimulation to the model. Simulations

ran for a total of 300s in the case of MVIC, and 145s for submaximal contractions to

allow for testing of recovery dynamics in the model. The output from these simulations

was then compared with in vivo data from older men to test the validity of the newly

formulated model.

In order to test fatigue prediction in the model, a simulation was run using both

YM and OM, consisting of 6, 12s contractions, each separated by 12s rest. This protocol

was designed to match recently published data from our lab, which were selected for their

provision of data related to fatigue and intracellular metabolites for comparison (111).

The simulation ran for a total of 144s with 0.001s time resolution.

Results

Age related changes in to activation and contractile characteristics were evaluated

for accuracy with in vivo data, effective differentiation from the Young model. This was

accomplished by simulating a stimulation pattern meant to emulate neuromuscular

stimulation at a range of frequencies. The results are illustrated in Figure 2. Compared

with in vivo results, the Old model predicted peak torque values in response to a range of

stimulation frequencies that were, in some cases, slightly below observed torque, but

largely within the standard deviation of measured values. Further, the Old model

demonstrated a significant leftward shift in the torque-frequency relationship compared

with the Young model (dotted line for reference).

Results from the simulation of a single voluntary, 12s MVC in the Old model are

illustrated in Figure 3. Simulated depletion and recovery of [PCr] matched well with in

vivo measures in both rate and amplitude (Figure 3A). Similar results were seen in the

prediction of pH through the contraction and recovery cycle. A slight over-prediction of

Pi and $H_2PO_4^-$ concentrations is observed following the contraction, although this may be

an artifact of the spectroscopy measure itself (see discussion).

Simulations of submaximal voluntary contractions (Figures 4 and 5) yielded

accurate predictions of metabolites thought to be related to fatigue in vivo. For the

duration of the simulated 12s contraction and 118s recovery period, simulated data were

well within the standard deviation of in vivo observations of PCr, Pi, pH, and $H_2PO_4^-$.

Fatigue predicted by the Old model was consistent with in vivo measures (111)

and is illustrated in Figure 6A. A comparison between identical simulation protocols,

illustrated in Figure 6B, revealed less fatigue in the Old model than that predicted by the

Young model (79.1%). The degree of fatigue resistance demonstrated by the Old model

(84.4%) was similar to that reported for similar contraction protocols in vivo (25; 111;

112).

Overall, the Old model was capable of predicting contractile and intracellular

metabolic kinetics during single contractions. The Old model successfully emulated in

vivo data and demonstrated relevant shifts in these variables with respect to the Young

model that were consistent with in vivo observations. Simulation of repeated MVC

resulted in fatigue that was consistent with that observed in a separate cohort of older

men. Importantly, fatigue in the present model formulation was less than that predicted

by the Young model, confirming those features modified in the present model contributed

to the prediction of age-related fatigue resistance.
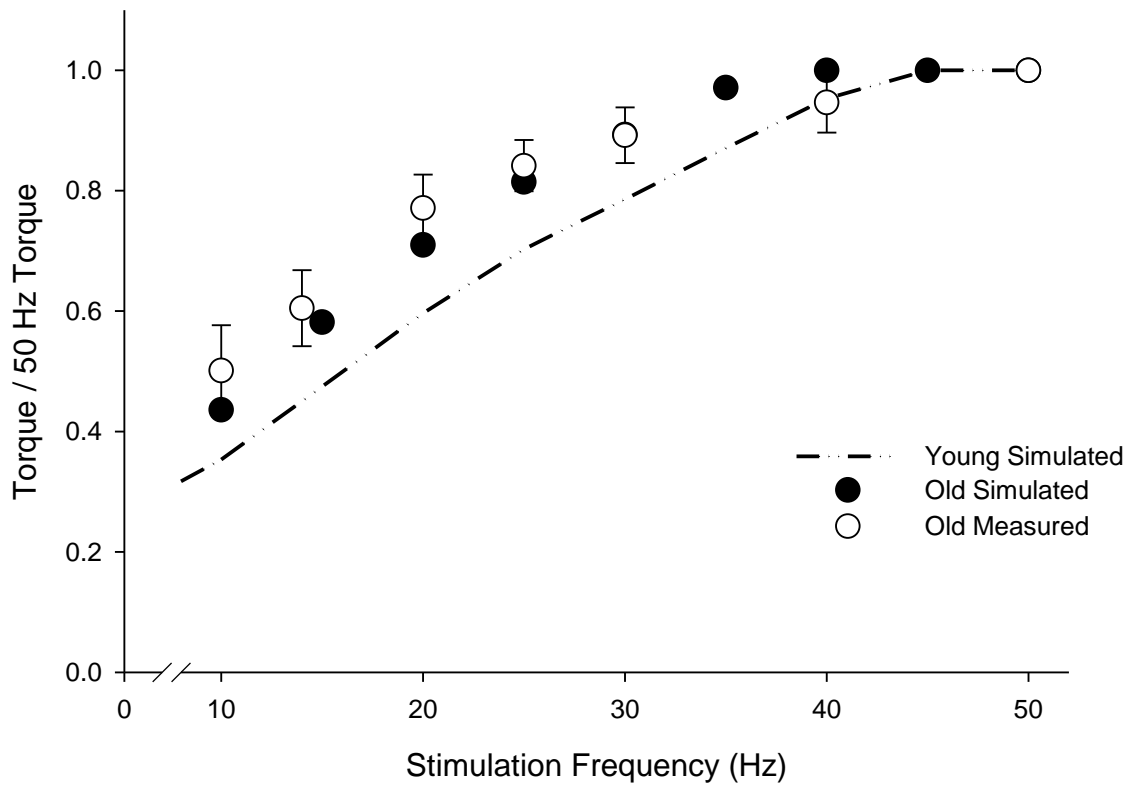
Figure 6.2 Simulated and in vivo torque-frequency relationships in older adults.
Simulated (open circles) and in vivo (closed circles ± SE) observations of the torque
response to stimulation at a range of frequencies (10-50 Hz). The dotted line
represents the output of the same simulation run on a similar model representing the
neuromuscular system of young men (Young model)
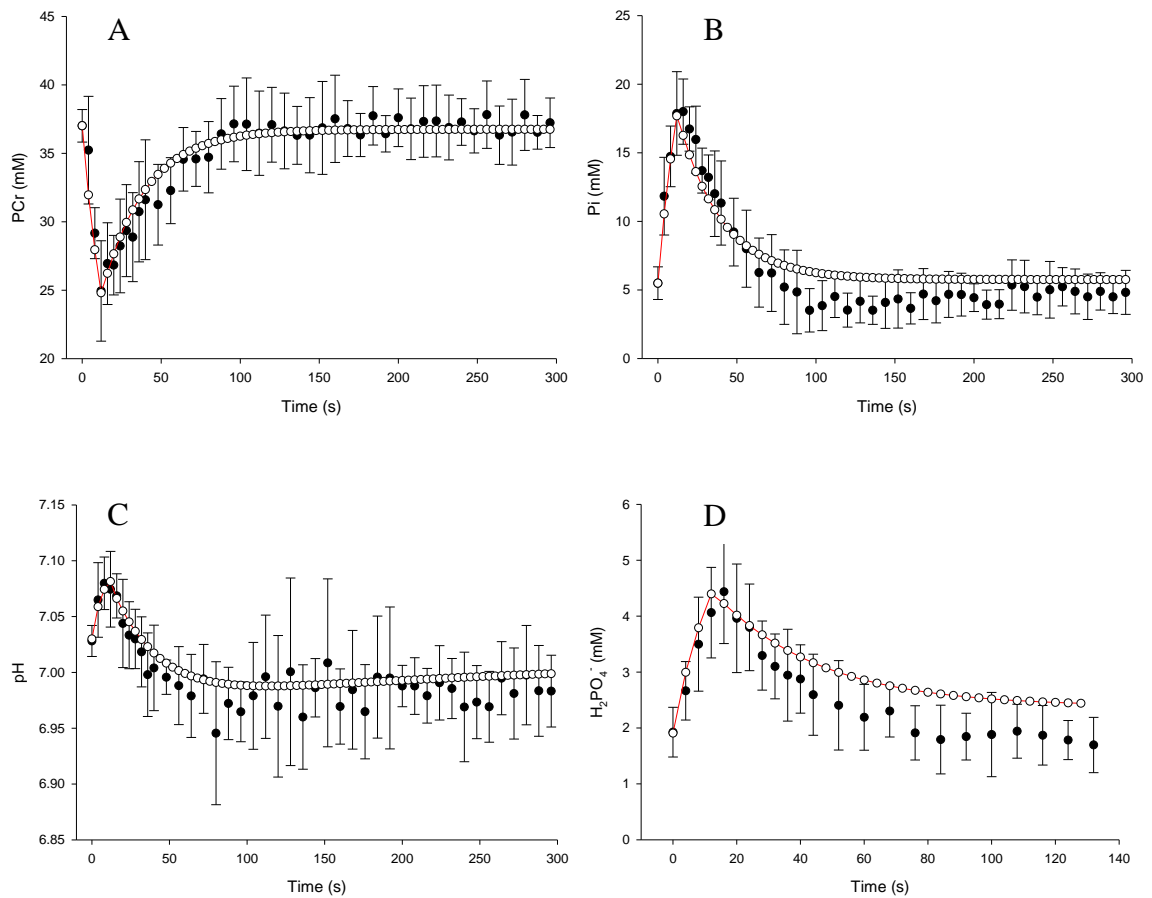
Figure 6.3 (A, B, C and D) **Simulated metabolic response to 12s contraction at 100% MVC.** Results from the simulation of voluntary, 12s MVC are illustrated in Figure 3. Simulated (open circles) depletion and recovery of phosphocreatine (PCr) concentration (A), inorganic phosphate (Pi, B), pH level (C) and di-protonated phosphate ($H_2PO_4^-$; D) correspond well with in vivo measures (closed circles $\pm$ SD) for both rate and amplitude
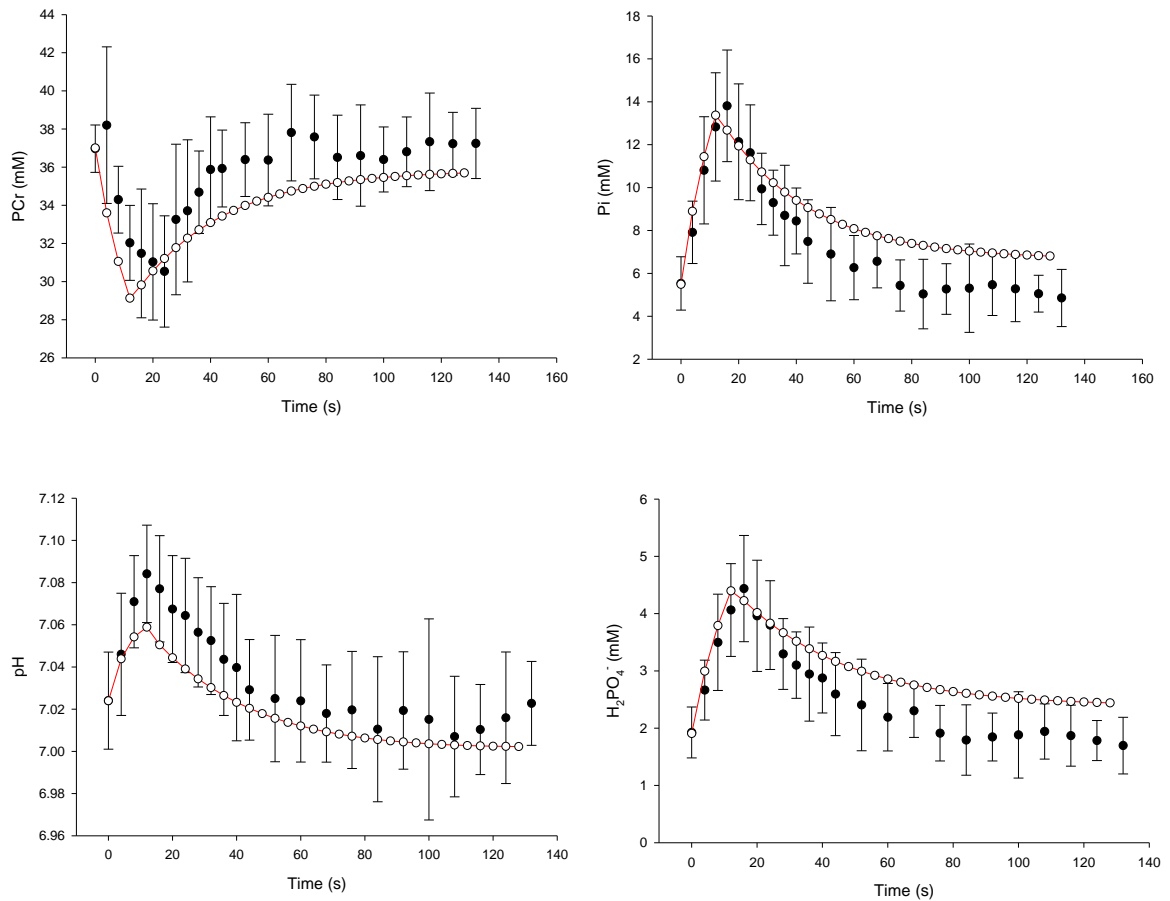
Figure 6.4 (A, B, C and D) Simulated metabolic response to 12s contraction at 50% MVC. Simulated responses of intracellular metabolites during a 12s voluntary contraction at 50% MVC. Simulated (open circles) depletion and recovery of phosphocreatine (PCr) concentration (A), inorganic phosphate (Pi, B), pH level (C) and di-protonated phosphate ($H_2PO_4^-$; D) correspond well with in vivo measures (closed circles $\pm$ SD) for both rate and amplitude. During the latter stages of simulated $H_2PO_4^-$ recovery, predictions were slightly elevated compared with in vivo measures

123

A

B

C

D
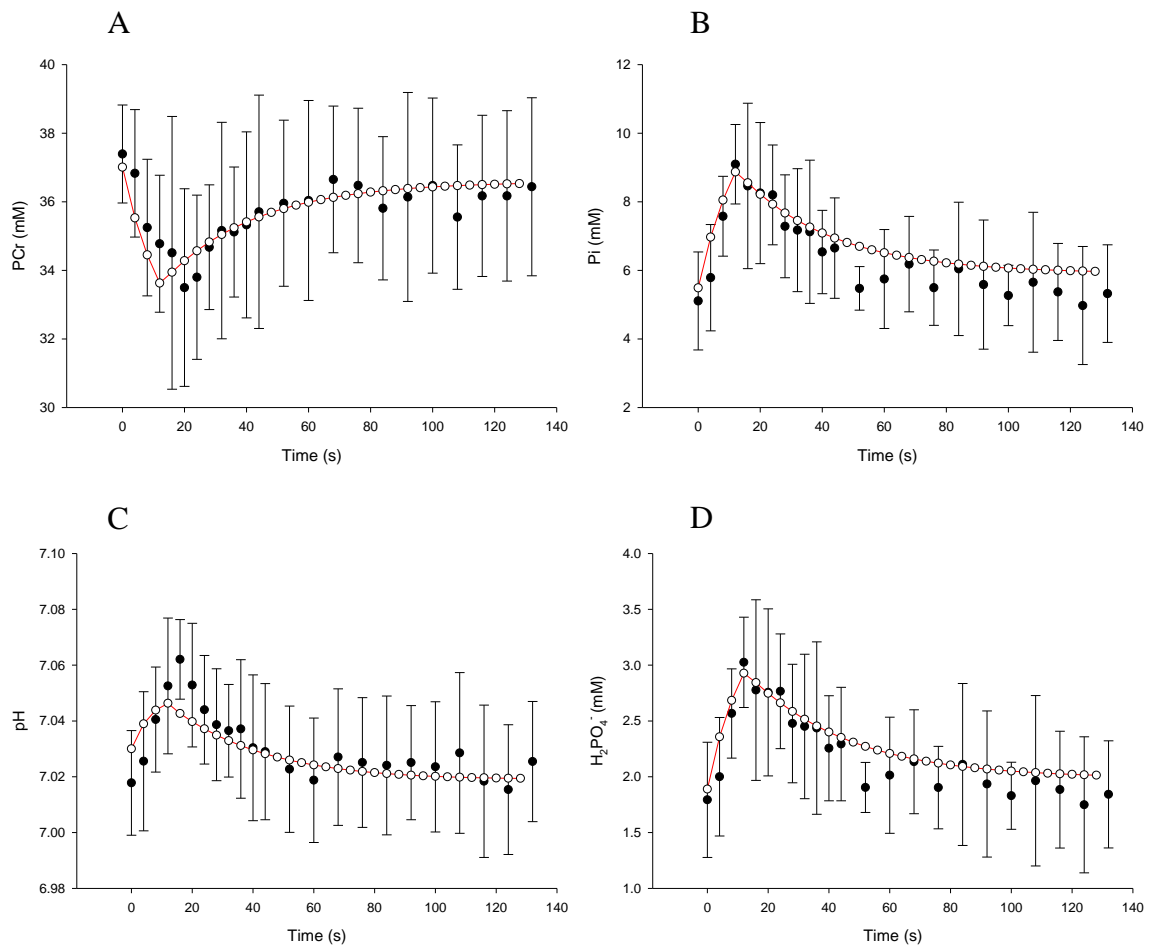
Figure 6.5 (A, B, C and D) Simulated metabolic response to 12s contraction at 20% MVC. Simulated responses (open circles) of intracellular metabolites (A: PCr, B: Pi, C: pH, D: $H_2PO_4^-$) are compared with in vivo measures (closed circles ± SD) during a 12s voluntary contraction at 20% MVC. Model predictions matched very well with in vivo data for all metabolites for the period of contraction and recovery
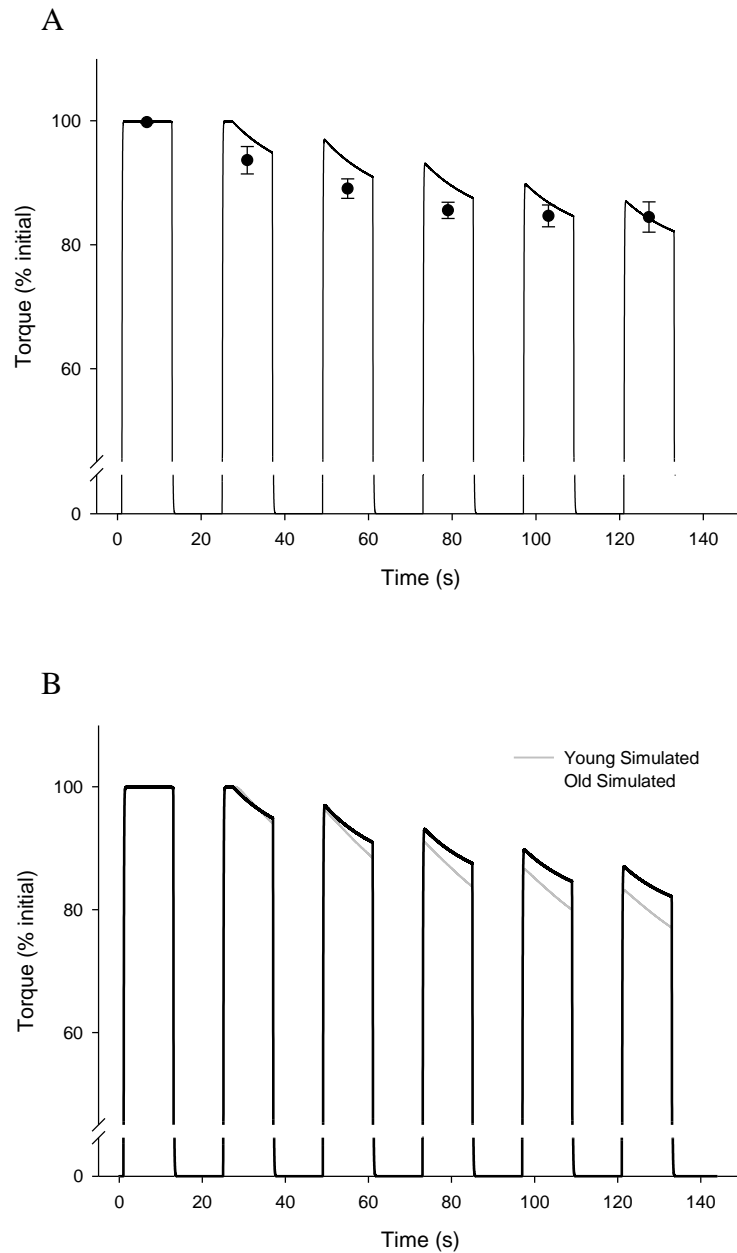
Figure 6.6 (A and B) Predicted fatigue from model simulation. **A:** A simulation of repeated maximum voluntary contractions (solid black line) compared well with the identical contraction protocol performed in vivo (closed circles ± SD). B: Comparison between current simulation (Old model, black line) and previously formulated version of the model meant to emulate neuromuscular function in young men (Young model, grey line). Differences in peak torque (% initial) achieved during repeated contractions were consistent with in vivo measures (Lanza et al, 2007)

125

Discussion

The model simulations presented here are the first to accurately predict contractile, bioenergetic, and ultimately fatigue responses to repeated isometric contractions. Although previous models have been designed and validated to capture the effects of age on activation and contractile function (72; 73; 175), and others have predicted fatigue (40; 118; 159; 190), this is the first to do both simultaneously. Our model employs a physiologically relevant means of activation and high level of integration while maintaining accuracy. Importantly, the Old model predicted age-related differences in contractile and metabolic variables implicated in fatigue resistance. The validation of this model presents a powerful tool for gaining insight to the mechanisms of age-related fatigue resistance.

Methodological Issues

Certain methodological considerations are necessary before applying this model or interpreting its results. Alterations to the present model, relative to that presented previously, were within the range of in vivo data available locally and in the literature. However, many of these measures have a large degree of variability and may depend on factors other than age (114). In addition, variables such as pH depend on multiple inputs, whose precise value can only be approximated. These two considerations open the possibility that multiple errors in our model offset one another and lead to a reasonable predictions through inappropriate means. However, our phenomenological model was validated at multiple steps along its sequential pathway, providing strong evidence that our inputs did not vary widely from in vivo measure.

Multiple variables from the literature were manipulated to some degree, after tuning individual functions to ensure accurate prediction of intermediate steps along the pathway of force production. However, none were altered by more than 50%, and all were within the range of measured values in our dataset, or the literature from which they were derived.

A notable absence from our modeled prediction is ATP produced from oxidative metabolism during contraction. Production of H^+ from oxidative phosphorylation during isometric contraction is modest, and likely not different between old and young individuals. However, during prolonged contractions, especially during fatigue, oxidative metabolism likely plays a key role in fatigue resistance. The fact that older individuals tend to rely on oxidative metabolism to a greater extent than young during prolonged bouts of contraction is likely related to their greater fatigue resistance. In our model, the effects of oxidative phosphorylation and age-related differences in cellular metabolism are captured implicitly by our predictions of PCr and Pi kinetics. However, the absence of an explicit prediction of oxidative metabolism likely precludes the model from accurately predicting the metabolic and fatigue response during more energetically demanding dynamic contractions.

Current Implications and Future Directions

The utility of a computational model depends on accuracy and flexibility to predict results not used during formulation. The model presented here accurately predicts contractile and metabolic responses to voluntary activation based on a combination of literature values and experimentally derived, in vivo data. These formulations combine to predict age-related differences in independent simulations run using two models. Each

of these models was tuned to reflect the neuromuscular responses to activation in older and younger adult males. Our model has demonstrated both accuracy and flexibility by accurately predicting age-related fatigue resistance and overall magnitudes of fatigue consistent with independent data-sets from the literature (111).

An important aspect of the present results is the influence of buffering capacity and Pi recovery kinetics on the fatigue response, and the role these aspects of neuromuscular function likely play in age-related fatigue resistance. Although a formal sensitivity analysis was beyond the scope of the present work, tuning of the model functions to reflect known, age-related changes in neuromuscular function revealed these components had a particularly strong effect on prediction of fatigue. Also noteworthy was the greater fidelity of the Old model than the Young model to fatigue predictions when compared with a separate data-set. Initial indications are that the Pi recovery kinetics in the cohort of older men used to parameterize the Old model were very similar to those of the data-set used for fatigue estimate validation. The calculated values for kPCr were more similar for these groups of older adult men than were the kPCr values in the Young model and young men from Lanza et al (113). The fact that the Young model predicted less fatigue than that reported in Lanza et al is consistent with more rapid Pi recovery in the Young model compared with those in Lanza et al. This highlights the importance of oxidative capacity in fatigue resistance, and provides an early target for future hypothesis testing with the present model.

Future application of this model might include sensitivity analysis of key variables to determine their relative impact on overall fatigue prediction. This process may shed light on the mechanisms of age-related fatigue resistance. In addition, the

model could be adapted to predict the fatigue response in other muscle groups or study populations.

Acknowledgements

CHAPTER 7

A COMPREHENSIVE APPROACH TO MODELING INTERRELATED IN VIVO SYSTEMS

<u>Novel Contributions</u>

The work presented here contributes significantly to a growing list of computational models meant to capture the physiological response to repeated or prolonged activation (38; 39; 43; 118). The development of models with progressively increasing complexity is a daunting process, filled with potential pitfalls. The number of predictions made by a model is accompanied by a necessary increase in the number of assumptions included in the model's formulation. Inaccuracies in these assumptions may have a sizeable impact on the overall conclusions made by the model. A unique contribution of the model presented here is its modular computational structure. Each portion of the models formulation results in a prediction of physiological behavior that can be compared with in vivo observations. This approach provides some degree of security against the potential for single, inaccurate model assumptions to have an overwhelming impact on total model output.

Further, the present model uses a flexible means to control central excitation, in a model of neural activation similar to Fuglevand et al (59), but augmented by a modular, multi-system model of neuromuscular function. Our efforts are, in some respects, similar to others in the literature (38; 39). In many respects, the applications of Dideriksen et al (38; 39) serve as an interesting counterpoint to the model presented here. In both models, the approach presented by Fuglevand et al (59) was adapted to predict fatigue during

repeated voluntary activations. Our approach is distinguished by the use of ^{31}P MRS, MRI and ultrasound data to construct models of metabolic perturbation, muscle force development and dorsiflexor torque generation, respectively. Our model formulations demonstrated both internal consistency and external validity when each step was compared with available data. This successful attempt to characterize physiological events in the pathway to joint torque generation, as opposed to a more generalized approach to describing physiological processes (especially metabolic perturbation) improves our model's ability to provide unique insights to the mechanisms of muscle fatigue.

Methodological Considerations

Despite careful consideration of the impact of parameter optimization at every step along the model's development, the output from model simulations should always be interpreted with some caution. Consistently accurate predictions at intermediate steps along the pathway to torque production limit the potential for widely inaccurate prediction of variables of interest. However, as the model is applied to conditions that diverge from conditions used in its formulation, assumptions made regarding individual functions within the model may reduce the accuracy of model predictions in ways that have not been anticipated.

These considerations must be made with every model forumulation and are no different in the present application. This is especially true of our metabolic perturbation model. While this novel formulation provides a volume of interesting predictions and as well as a means for gaining insight to the role of intracellular metabolic status in fatigue, it may be especially prone to error. This is because the measured values of metabolites

131

via ^{31}P MRS depend on calculations with a number of assumptions. Several investigators have demonstrated the accuracy and validity of ^{31}P MRS under a variety of conditions. Combined with its non-invasive nature and high temporal fidelity ^{31}P MRS is a powerful and useful tool, uniquely suited to the present application. However extremely subtle variation in the values derived from our ^{31}P MRS studies can have significant implications for the models overall prediction.

For example, informal sensitivity analysis in the present model (data not shown) revealed that the rate constant for PCr recovery has a significant impact on muscle fatigue predictions and likely has the greatest influence on the differences we have observed between our age-specific fatigue models (Chapter 6, Figure 5B). This prediction agrees with the literature regarding the role of oxidative metabolism in fatigue resistance, but does not capture the variability, and sometimes inconsistent relationship, between whole muscle oxidative capacity and fatigue resistance (37). These considerations do not necessarily represent limitations in this context, but are important to appropriately interpret the models output.

Future Directions

Here, we present a novel and comprehensive computational model of neuromuscular function, capable of predicting metabolic perturbation and subsequent fatigue during repeated voluntary activations. This model provides us with a powerful tool for improving our understanding of the phenomenon of age-related fatigue resistance. In its current state, formal sensitivity analysis may be performed with the model to gain insight on the relative impact of age-related neuromuscular changes on fatigue resistance. These estimates could be used to form the basis of hypotheses tested

in vivo. Further utility can be found by applying the model in its present state to various fatigue protocols used in the literature to explore the "task-dependent" nature of skeletal muscle fatigue.

The present model has been parameterized to represent the function of healthy young, physically active younger men, and separately, a group of healthy, relatively sedentary older adults. The inputs to the model used to characterize these subject groups could be adapted to represent other populations as well without significant alterations to the computational approach. Clinical populations characterized by altered neural function (multiple sclerosis), cellular metabolism (McCardle's disease, diabetes) or skeletal muscle atrophy (cancer, HIV) could be emulated by the current version of the model.

Despite the comprehensive approach used here, the model's complexity does not approach that of the neuromuscular system, and many simplifications and assumptions were made to achieve reasonable computation times and limit sources of potential error. However, future incarnations of the model might be adapted to include, for example, oxidative metabolic processes during muscle activation. Oxidative metabolism is necessary for cellular function and its role in skeletal muscle contractile function cannot be overstated. The lack of an explicit function describing oxidative processes in the present model likely limits its application to certain experimental conditions. Similarly, the present model is constrained to isometric contractions, but might be significantly more useful as a component in forward dynamic simulations of metabolic cost if it were adapted to perform dynamic contractions. Compared with isometric contractile function, relatively little is known about the metabolic responses to dynamic contractions. The

present model, adapted to voluntary activation during dynamic changes in overall muscle length, might contribute substantially to our understanding of intracellular metabolic function during dynamic muscle contraction.

APPENDIX A

GLOSSARY OF TERMS

Alpha motor neuron: Neurons in the ventral horn of the spinal cord responsible for activation of skeletal muscle. Alpha motor neurons receive excitatory signals primarily from cortico-spinal tracts that deliver signals from the motor cortex. Activation of the alpha motor neurons results in depolarization and conduction down its axon to a group of muscle fibers.

Central activation: The ability of the central nervous system to fully excite a muscle or muscle group. In the case of complete central activation, additional stimulus will not elicit greater force from the activated muscle.

Central fatigue: Component of fatigue that results from insufficient neural activation. Limitations may reflect diminished excitation of the motor cortex, and excitability of alpha motor neurons in the spinal cord.

Cross bridge: Term referring to the bound actin and myosin during muscle activation. Cross bridges provide the foundation for active force generation in skeletal muscle.

Dashpot: A mechanical damper that slows, or smoothes the movement of spring-like oscillators.

Deterministic: Behaving in a definite manner. Deterministic equations will reliably result in identical solutions if initial conditions are identical.

Distribution Moment: Mathematical characterization of probability involving a number of points in space. The even distribution of points around a central focus is typically referred to as a "normal distribution".

Dynamic contraction: Skeletal muscle contraction during which overall muscle length changes resulting in limb movement.

Electromyography: Technique used to record electrical activity of muscles. Depolarization of the sarcolemma causes local changes in voltage that can be recorded using electrodes inserted into the muscle, or applied to the surface of the skin.

Fatigue: Acute loss of force generating capacity in response to repeated or prolonged activation in skeletal muscle fibers.

Group III and IV afferent nerve fibers: Sensory neurons that conduct signal from skeletal muscle to the spinal cord. It is thought that activation of these fibers inhibit activation of alpha motor neurons and may decrease cortical excitability.

Hill muscle model: Muscle model consisting of components that describe the passive and active components of skeletal muscle force generation. Named for A.V. Hill, these phenomenological models describe the behavior of muscles or muscle groups without addressing intracellular mechanisms of force generation.

Huxley muscle model: Muscle model that uses multiple partial differential equations to describe force generation in skeletal muscle at the level of the sarcomere. Named for H. Huxley, these models predict force generation by calculating the probability of force generating interactions between actin and myosin for a given set of conditions.

Isometric contraction: Skeletal muscle contraction during which no external movement occurs.

Magnetic Resonance Spectroscopy: Technique used in chemical sciences to identify the components of molecules, but also applied to physiologic tissues to non-invasively determine the relative concentration of compounds within them. Magnetic resonance spectroscopy relies on the signal generated when nuclei, exposed to a strong magnetic field, are excited using a radio-frequency pulse.

Mechanistic model: A model that mathematically describes a system and the components that determine its overall behavior. Mechanistic models have the capacity not only to predict how a system will behave, but how its underlying mechanisms might individually contribute to that behavior.

Motor unit: An alpha motor neuron and all of the muscle fibers innervated by that neuron.

Myosin heavy chain: Intracellular protein in skeletal muscle formed by multiple myosin II molecules. Myosin heavy chain is arranged in parallel with actin. During activation, myosin heavy chain and actin bind to produce force.

Ordinary differential equation: Mathematical relationship between functions of a single independent variable and one or more derivatives with respect to that variable.

Partial differential equation: Mathematical relationship between several independent variables (functions) and their partial derivatives with respect to those variables.

Peripheral fatigue: Component of fatigue resulting from reduced depolarization of the sarcolemma, reduced calcium release from the sarcoplasmic reticulum, reduced cross bridge formation or reduced force generated per cross bridge.

Phenomenological models: A model that mathematically describes empirical observations of a system. The observable features of the system in question may not reflect all of its underlying mechanisms.

Poisson distribution: Mathematical characterization of event probabilities over time, formulated by Simeon-Denis Poisson.

Stochastic: Behaving in a random manner. Stochastic equations include an element of chance, such that identical initial conditions will not guarantee identical outcomes.

Recruitment threshold: Minimum voltage necessary to cause activation (depolarization) of an alpha motor neuron.

Rheological: Relating to the flow or deformation of matter. Rheological components of a musculo-skeletal models refer to the passive spring-like, and active force-generating components of the model.

APPENDIX B

SOURCE DATA AND PARAMETERS FOR HYPOTHESES 1-3

Table 2 Source of Equations and Data

Model Step	Source of equations and data
Hypothesis 1	
Excitation (S)	Equations 1,2, and 3 dictate S based on difference between target torque (T_t) and current torque (T_c) predicted by model.
Motor Neuron Pool	120 MNs described by Fuglevand (58) Equations 1 and 2 describe activation status and firing rate MFR = 8 Hz PFR = 46-56 Hz
Muscle Activation	Membrane depolarization and Ca^{2+} kinetics calculated with each pulse using equations [9,10,11] according to (75)
Muscle Model	Hill type model based on van Soest (179) and Umberger (175) F for each of 120 models will be distributed similar to recruitment threshold (equation 5) over a 100-fold range, and scaled to theoretical value of peak force generating capacity in the contractile component of ankle dorsiflexor muscle group (Umberger, XIII ISCSB, 2011).
Metabolic Perturbation	From spectroscopy data described in Appendix D, equations 22a and 22b
Joint Torque	Musculo-skeletal model from existing data and parameterized to account for changes in moment arm with force (124)
Simulation Protocol	T_t set to 110%, 50%, 20% predicted MVC torque for 12s
Hypothesis 2	
Excitation (S)	S begins at 0. Increases and subsequent decreases determined by Controller function; equations [1,2,3].
Motor Unit Pool	120 MUs described by Fuglevand (58) Equations 4 and 7 describe activation status and firing rate MFR = 8 Hz PFR = 46-56 Hz
Muscle Activation	Membrane depolarization and Ca^{2+} kinetics calculated with each pulse using equations [9,10,11] according to (75)
Muscle Model	Hill type model based on van Soest (179) and Umberger (175) F for each of 120 models will be distributed similar to recruitment threshold (equation 5) over a 100-fold range, and scaled to theoretical value of peak force generating capacity in the contractile component of ankle dorsiflexor muscle group (Umberger, XIII ISCSB, 2011).
Metabolic Perturbation	From spectroscopy data described in and Appendix D, equations 22a and 22b
Limits on F	From metabolic data in Lanza (91); Equation 5
Joint Torque	Musculo-skeletal model from existing data and parameterized to account for changes in moment arm with force (104)
Simulation Protocol	T_t = 110% predicted MVC for 12s, and 0 for 288s T_t = 50% predicted MVC for 12s, and 0 for 128s T_t = 20% predicted MVC for 12s, and 0 for 128s
Simulation Protocol	T_t = 110% predicted MVC for 6,12s contractions, and 0 for 12s between

Hypothesis 3	
Excitation (*S*)	*S* begins at 0. Increases and subsequent decreases determined by Controller function; equations [1,2,3].
Motor Unit Pool	120 MUs described by Fuglevand (58) Equations 1 and 2 describe activation status and firing rate MFR = 8 Hz PFR = 35-45 Hz (Reduced ~10% according to (29))
Muscle Activation	Membrane depolarization and Ca^{2+} kinetics calculated with each pulse using equations [9,10,11] according to (75)
Muscle Model	Hill type model based on van Soest (149) *F* for each of 120 models will be distributed in accordance with equations 5 and 6 from Fuglevand (49) and scaled to muscle size ((O = 266 cm^3) unpublished observations). Further adjustments will reflect changes to contractile kinetics (144), force per motor unit (25) and pennation angle (unpublished observations) with age
Limits on *F*	From metabolic data in Lanza (91); Equation 5
Joint Torque	Musculo-skeletal model from existing data and parameterized to account for changes in moment arm with force (104)
Controller	Control model according to Xia (156) and equations 9 and 10

APPENDIX C

PROJECT TIMELINE

Table 3. Project Timeline

Task	Task Components	Duration	Total Time
Data collection/processing	Assessment of contractile cost via MRS. Musculo-skeletal parameterization from tendon tracing procedures. *Other model variables to be taken from literature*	4 weeks	4 weeks
Model Formulation	Each proposed parameter in the model will be tested and sensitivity analysis will be performed. Model components will begin with commonly reported values in the literature but greater scrutiny will be given those components having the greatest influence.	16 weeks	20 weeks
Model Validation	Once each component of the model is successfully run, it will be valid to determine fatigue within one standard deviation of experimental data reported in the literature. Further sensitivity analysis will reveal which model components have the greatest effect on prediction of fatigue	2 weeks	22 weeks
Model Alteration	The model will be altered to reflect known physiologic changes with age. These will include alterations to peak MU firing rates, slowed contractile kinetics, decreased contractile cost, and relatively less accumulation of hydrogen ion for a given amount of metabolic work. The models predictions will again be compared to literature values.	2 weeks	24 weeks
Model Conclusions and Defense	The results of these comparisons and model performance will be written into a formal dissertation document.	8 weeks	32 weeks

APPENDIX D

CALCULATIONS FOR THE INTEGRATED NEUROMUSCULAR MODEL

The model parameters were sourced from experimental, and published values. The model was constructed based on the following scheme. Roman numerals correspond to model steps illustrated in Figure 1:

I. An error function evaluates the difference between current torque (T_c) and a pre-defined target torque (T_t); Equation 1. Values for T_t are calculated prior to running the model, and T_c is calculated as show in equation 38.

   a. *Stimulation (S) to model adjusted*

$$T_{diff} = T_c - T_t \tag{1}$$

$$\uparrow S = S + (RT_{diff} \cdot (1 - S)) \tag{2}$$

$$\downarrow S = S - (RT_{diff})^r \cdot S \tag{3}$$

Where T_{diff} is the absolute difference between the current and target torque values. RT_{diff} is T_{diff} expressed relative to the expected maximum torque generating capacity of the model. The exponent r moderates the rate of decreasing stimulation. Informal optimization for the most realistic stimulation kinetics resulted in a value of 0.7 for r.

II. Recruitment model determines the firing rate *(FR)* within specified range (minimum: *MFR*; peak: *PFR*) for each motor neuron (*m*: 1-120) after recruitment threshold (*muRT*) is met.

Current firing rate (*FR*) is the product of gain (*G*) and the difference between the current stimulation level (*S*) and the recruitment threshold of motor neuron m ($mnRT_m$) when S exceeds $mnRT_m$.

$$FR = G \cdot (S - (mnRT_m)) + MFR \tag{4}$$

a is a coefficient whose value is determined by the range of desired activation thresholds (A_{range}) and the total number of simulated motor neurons (MN_{num}).

$$a = \log(A_{range}) / MN_{num} \tag{5}$$

The recruitment threshold of the last-recruited *MN* (RT_{last}) is a function of a and the index of the last *MN* (MN_{num}).

$$RT_{last} = \exp(a \cdot MN_{num}) \tag{6}$$

The recruitment of each motor neuron (*m*) follows the same function.

$$mnRT_m = \exp(a) \tag{7}$$

Peak firing rate for the mth motor neuron is determined by subtracting the product of the range of desired firing rates (FR_{range}) and the recruitment threshold of of the mth motor neuron (expressed relative to the highest recruitment threshold of the pool) from the desired peak firing rate (PFR).

$$mnPFR_m = PFR - (FR_{range} \cdot (mnRT/RT_{last}))$$

(8)

Where $G = 2$, the gain for the activation signal; $A_{range} = 30$, the desired range of activation thresholds; $FR_{range} = 10$, the desired range of peak firing rates; $MFR = 8$, the minimum firing rate in Hz; $PFR = 56$, the highest observed firing rate; and $MN_{num} = 120$, the total number of motor neurons.

III. Current firing rate (FR) is used to calculate the inter-pulse interval (IPI), which is compared with the calcium transient duration ($Ca_{on} = 0.023$s). At each time step during the simulation, a counter is initiated for each active motor neuron, tracking its IPI. Throughout the simulation, the active counter for reach MN is compared with Ca_{on}. When the counter is less than Ca_{on}, $Stim = $ "1". When the counter is greater than Ca_{on}, but less than IPI, $Stim = $ "0". When the counter is = to IPI, the counter resets to zero. Activation kinetics are determined by the following equations:

$$\dot{act} = (Stim - act) \cdot (rc_1 \cdot Stim + rc_2)$$

(9)

$$rc_2 = 1/t_{deact}$$

(10)

$$rc_1 = 1/t_{act} - rc_2$$

(11)

Where t_{act} has values between 0.060 - 0.039 depending on motor neuron (m) and represents the activation time constant. Deactivation time constants are defined by t_{deact} and have values between 0.092 - 0.064.

IV. Vector equations determine rates of change for state variables meant to represent contractile dynamics: The muscle model consists of a contractile element (ce) and series elastic element (see). The behaviors of these elements depended on their respective lengths (lce, and sel respectively) and their sum always equaled the length of the myotendenous unit (lmt) in order to simulate an isometric contraction.

   a. Contractile dynamics
   Because simulated contractions are isometric, change in lmt is equal to zero.
   $$\dot{lmt} = 0 \; (isometric)$$
   (12)

c_0 is a coefficient defined by the width of the *force-length* relationship and is used to moderate isometric force generating capacity of the ce (f_{iso}) depending on current lce with respect to the optimum force-generating capacity length lce_{opt}.
   $$c_0 = {}^-1/\omega$$
   (13)

$$f_{iso} = c_0 \cdot (lce / lce_{opt})^2 - 2 \cdot c_0 \cdot (lce / lce_{opt}) + c_0 + 1 \qquad (14)$$

$$f_{act} = act^{0.3} \qquad (15)$$

Change in *lce* depends on current activation level (f_{act}) f_{iso}, and maximum shortening velocity, defined by *arel* and *brel*, modified Hill coefficients according to van Soest et al, 1993 (179). The following equation refers specifically to concentric contractions.

$$\dot{lce} = ^{-}1 \cdot f_{act} \cdot lce_{opt} \cdot ((((f_{iso} + arel) \cdot brel) / (fce / (f_{max} \cdot act) + arel)) - brel) \qquad (16_{con})$$

Pennation angle (*pen*) is calculated based on current *lce*.

$$pen = (180 / \pi) \cdot (a\sin((lce_{opt} \cdot \sin((\pi / 180) \cdot pen_0)) / lce)) \qquad (17)$$

The current values for *pen* and *lce* are used to determine *sel*.

$$sel = lmt - lce \cdot \cos(pen \cdot \pi / 180) - l_{slack} \qquad (18)$$

The *see* is modeled as a non-linear spring whose force (*fsee*) is based on *sel* and a spring constant *ksee*.

$$fsee = ksee \cdot sel^2 \qquad (19)$$

Finally, force in the *ce* (*fce*) must equal that in the *see* while accounting for pennation angle.

$$fce = fsee / \cos(pen \cdot \pi / 180) \qquad (20)$$

Where $\omega = 0.56$ (179) and $lce_{opt} = 0.058$; *arel* is between 0.2 - 0.14 and *brel* is between 2.4 - 2.52. These values correspond to a and b coefficients for a typical Hill muscle model respectively.

IVa. Metabolic dynamics include inorganic phosphate (*Pi*), activation of glycolysis (*Gact*) and glycolytic rate (*L*). Hydrogen production from glycolysis (*H*) is offset by consumption of proton during the creatine kinase reaction (H_1). During recovery from contraction, the resynthesis of PCr will produce protons, as will oxidative phosphorylation (H_2). Net proton production or consumption is buffered (H_3) and used to calculate the current cytosolic pH (equation 31).

b. *Metabolic dynamics*

The activation level for metabolic dynamics (act_{rel}) is expressed relative to the maximum rate of inorganic phosphate (*Pi*) accumulation observed in vivo.

$$act_{rel} = (0.0045 + (^{-}0.0161 \cdot (act \cdot 100) + 4.19e^{-5} \cdot (act \cdot 100)^2)) / 1.189 \qquad (21)$$

During muscle model activation, *Pi* accumulates at a rate depending on act_{rel}, the duration of the contraction (*Ct*) and coefficients defining the sigmoidal relationship between contraction duration and *Pi* concentration (Pi_a, Pi_b, Pi_x).

$$\uparrow Pi = Pi_a / 1 + (\exp((^{-}Ct + Pi_x) / Pi_b)^2 / (Pi_b \cdot \exp(^{-}Ct + Pi_x / Pi_b)^{-} act_{rel}) \qquad (22a)$$

Recovery to resting levels of *Pi* were dependent on the duration of recovery (*Ct*) and recovery coefficients Pi_{ar} and Pi_{br}.

$$\downarrow Pi = {}^{-}Pi_{ar} \cdot Pi_{br} \cdot \exp({}^{-}Pi_{br} \cdot Ct) \tag{22b}$$

Pi_{ar} describes the amplitude of *Pi* recovery and depends on the peak concentration of *Pi* observed during muscle activation (Pi_p).

$$Pi_{ar} = -5.049 + 1.196 \cdot Pi_p \tag{23}$$

Pi_{br} is the rate constant for *Pi* recovery and also depends on Pi_p.

$$Pi_{br} = 0.0296 + 1.0236 \cdot \exp(-0.4093 \cdot Pi_p) \tag{24}$$

A model of glycolytic rate (*L*) depends on the activation of glycolysis and current *Pi* concentration. The activation of *L* is determined from rate constants determining activation and deactivation kinetics of *L* similar to *ce* activation, both of which are dictated by *Stim*.

$$Grc_2 = 1/GT_{dact} \tag{25}$$

$$Grc_1 = 1/(GT_{act} - Grc_2) \tag{26}$$

$$\dot{Gact} = (Stim - Gact) \cdot (Grc_1 \cdot Stim + Grc_2) \tag{27}$$

Pi was assumed to influence *L* through Michaelis Menten kinetics.

$$\dot{L} = \dot{Gact} \cdot ((L_o \cdot (Pi - Pi_{rest}))/(K_m - Pi_{rest}) + (Pi - Pi_{rest})) \tag{28}$$

Protons (*H*) generated from *L* were based on the assumption that 3 glycolytic ATP are generated per proton produced through anaerobic glycolysis.

$$\dot{H} = \dot{L}/1.5 \tag{29}$$

Total protons produced must be balanced by those consumed in the creatine-kinase reaction. This is the product of θ and the breakdown of phosphocreatine, which is stoichiometrically equivalent to the amount of *Pi* generated.

$$\dot{H_1} = \dot{H_0} - (\theta \cdot Pi) \tag{30}$$

During the recovery of *Pi* to resting levels, protons are also generated from oxidative phosphorylation. Recovery of *Pi* is assumed to be an exclusively oxidative process but for possible minor contribution of glycolysis for a brief period immediately following sessation of activation. This is reflected in the model by assuming the rate of *Pi* recovery, minus current *L,* is equivalent to the rate of oxidative phosphorylation. The coefficient M defines the number of protons produced per oxidative ATP.

$$\dot{H_2} = \dot{H_1} - (M \cdot (\dot{Pi} - \dot{L})) \tag{31}$$

Finally, the total change in proton load (H_2) is divided by the total cytosolic buffering capacity (β_{total}) to determine the observed change in proton concentration (H_3).

$$\dot{H_3} = \dot{H_2}/\beta_{total} \tag{32}$$

Where $Pi_a = 48.19$, $Pi_b = 10.94$, and $Pi_x = 6.03$; Pi_{ar} and Pi_{br} are coefficients taken from a fit of Pi recovery following contraction. $GT_{act} = 0.2$, the time constant for

activation of glycolysis and $GT_{dact} = 1.2$, the time constant for deactivation of glycolysis; L_0 is the maximum rate of glycolysis and is a range between 0.86 - 1.71 mM $ATP \cdot s^{-1}$; $Pi_{rest} = 3.94$ and is the resting Pi concentration in mM; $Km = 15$ and is the concentration in mM of Pi at which glycogen phosphorylase reaches half its full activation. Coefficients for proton generation in the creatine kinase reaction (θ) and oxidative phosphorylation (M) were set at 0.357 and 0.14 respectively at the onset of exercise, but varied during the simulation, according to pH (183).

> c. *Vector equations determine state variables for current time point (t).*
>   *Variables reflecting the "intracellular state" for pH, diprotonated phosphate*
>   *(H_2PO_{4-}) buffering capacity of inorganic phosphate (B_{Pi}) and phosphocreatine*
>   *(PCr) for each MN(m) are then updated:*

$$pH = {}^{-}\log_{10}(H_3) + 7 \tag{33}$$

$$H_2PO_{4-} = Pi /(1 + 10^{(pH - 6.75)}) \tag{34}$$

$$\beta_{Pi} = (3.303 \cdot Pi)/(1 + 10^{(pH - 6.75)}) \cdot (1 + 10^{(6.75 - pH)}) \tag{35}$$

$$PCr = 42.5 - Pi \tag{36}$$

V. Metabolic and torque values are combined for all motor neurons/muscle model pairs (motor units), to calculate the sum total of modeled behavior at each time point. These are the representative output for each respective variable and are compared directly with experimental data.
    a. The weighted sum of metabolic variables are combined to reflect the value for each variable at each time point (*t*) for all motor units.

$$MetT = \sum_{m=1}^{MU_{num}} (Met_m \cdot f_{\max m}) / \sum_{m=1}^{MU_{num}} f_{\max m} \tag{37}$$

   ○ $f_{\max m} = 0.56 - 54.5$

VI. Force values for motor units are taken from *fsee* and summed linearly to estimate force at the tendon (F_t) which is then used to calculate moment arm length (L_{ma}) and current torque (T_c).
    a.

$$F_t = \sum_{m=1}^{MU_{num}} fsee_{(m)} \tag{38}$$

$$L_{ma} = L_{ma0} + ((L_{ma0} \cdot L_{maR})/(F_{\max} / F_t)) \tag{39}$$

Finally, the newly calculated T_c is compared with the designated T_t and the preceding steps are repeated.

$$T_c = F_t \cdot L_{ma} \tag{40}$$

Where L_{ma0} is the resting moment arm length (0.027m), L_{maR} is the potential range of increased moment arm length (0.249) and F_{max} is the maximum force possible at the tendon: $\sum_{m=1}^{MU_{num}} f_{max\ m} = 1433.4$ N

APPENDIX E

FORMULATION OF THE BIOENERGETIC MODEL

A key feature of the integrated neuromuscular model (Appendix D) is the bioenergetics component (Step IVa, equations 21-37). During activation and subsequent recovery, functions simulated the metabolic perturbation and return to homeostasis, respectively observed in vivo. A detailed description of the procedures followed to derive those functions follows below:

Contraction

The accumulation of inorganic phosphate (Pi) and depletion of phosphocreatine (PCr) during activation are based on maximal 12s contractions. The relationship between [Pi] and contraction time (*Ct*) was described by a sigmoidal function (Pi_a, Pi_b, Pi_x), selected for its goodness of fit with these experimental data. Our in vivo observations were augmented by a theoretical data point at 60s according to Lanza et al (110; 134) in order to more completely describe the relationship

between *Ct* and [Pi]. The first derivative of this function determines the rate of change of [Pi] in the bioenergetics model.
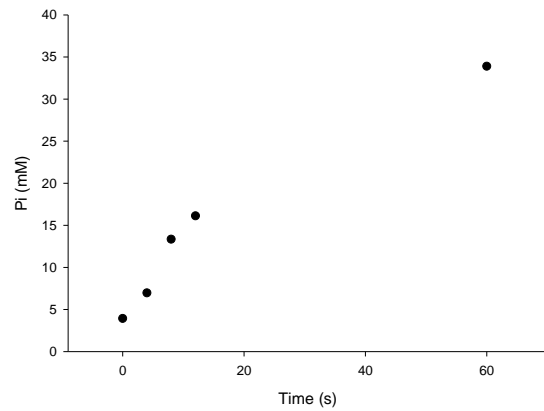
$$Pi = Pi_a / 1 + \exp((^-Ct + Pi_x)/Pi_b)^2 /(Pi_b \cdot \exp(^-Ct + Pi_x / Pi_b)) \qquad (1)$$

The relationship describing the initial rate of PCr depletion as a quadradic function of activation level (*act*) was used to scale changes in Pi predicted from equation 1. The first derivative of this function is expressed relative to the maximum rate of PCr depletion ($Dep_{max} = -1.189$) to scale the rate of change in activation (act_{rel}).
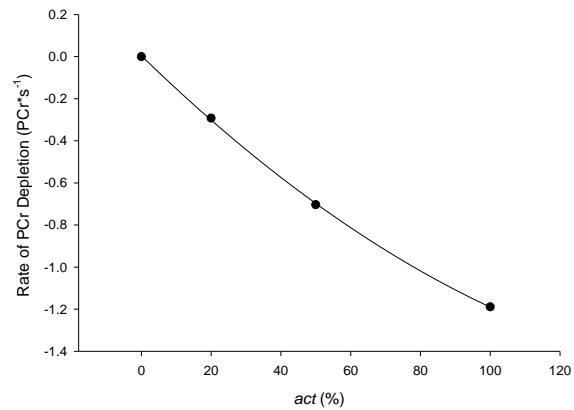
$$act_{rel} = (0.0045 + (^-0.0161 \cdot (act \cdot 100) + 4.19e^{-5} \cdot (act \cdot 100)^2)) / Dep_{max} \qquad (2)$$

Recovery

The bioenergetics model's calculations are highly dependent on Pi kinetics, but experimentally, these values suffer from inconsistent signal to noise during portions of the recovery from activation. Because the model assumes the ration between PCr and Pi to vary inversely and linearly (Pi + PCr = 42.5 mM), the kinetics of Pi recovery in the model were based on a hybrid of in vivo PCr and Pi recovery kinetics, described below.
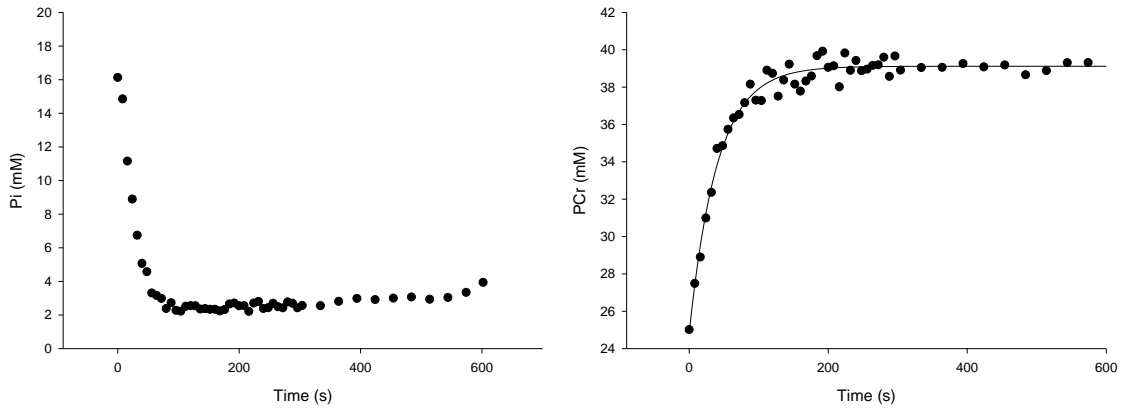
The time course of recovery to resting values for each metabolite was fit using 3-parameter, monoexponential functions. The coefficients for these functions (Y_0, Pi_{ar} and Pi_{br}) were used define the rate of recovery of [Pi] following contraction. The first derivative of the function describing [Pi] with respect to recovery time (Rt) was used to defined instantaneous recovery rate:

$$\dot{Pi} = {}^-Pi_{ar} \cdot Pi_{br} \cdot \exp({}^-Pi_{br} \cdot Rt) \tag{3}$$

In vivo observation revealed substantial variation in the recovery rate constant Pi_{br} depending on intensity of the previous contraction, defined by the peak [Pi] achieved during activation (Pi_P). To capture this within the model, Pi_{ar} and Pi_{br} were calculated as a function of Pi_P .
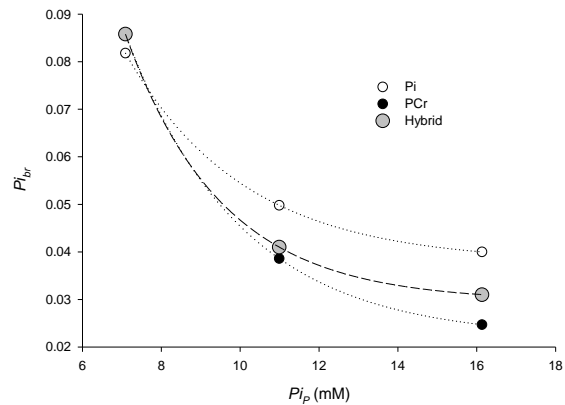
$$Pi_{br} = 0.0296 + 1.0236 \cdot \exp(-0.4093 \cdot Pi_p) \tag{4}$$

152

A similar approach was applied to the calculation of Pi_{ar} although less variation was observed between fits of PCr and Pi with Pi_{ar}. A linear function describing Pi_{ar} as a function of Pi_P fit both data sets equally well.
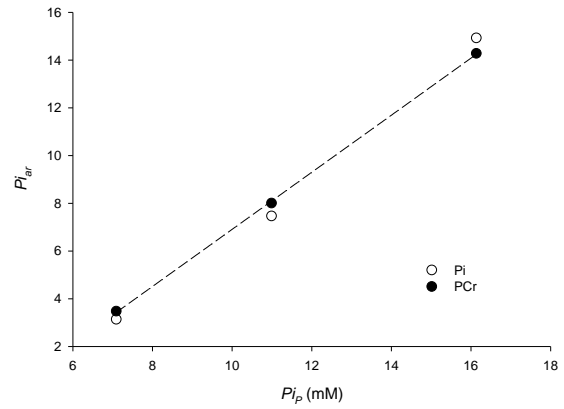
$$Pi_{ar} = -5.049 + 1.196 \cdot Pi_p \qquad (5)$$

APPENDIX F

ALTERATIONS TO THE BIOENERGETIC MODEL TO REFLECT CHANGES

WITH AGE

Alterations in the current model extended to bioenergetics formulation. During activation and subsequent recovery, functions simulated the metabolic perturbation and return to homeostasis respectively observed in vivo. A description of the procedures used to derive those functions, and how they differ from formulation of the Young model are listed below:

Contraction

Similar to the Young model, Pi accumulation kinetics during activation were based on in vivo observations of [Pi] during a 12s maximal isometric contraction in a cohort of older men (Christie et al, unpublished and Lanza et al (111)). In the present application, the relationship between [Pi] and contraction time (*Ct*) was fit with an exponential rise to maximum function. Corresponding data and sigmoidal line fit from the Young model are shown (grey circles, dashed line respectively) for comparison.
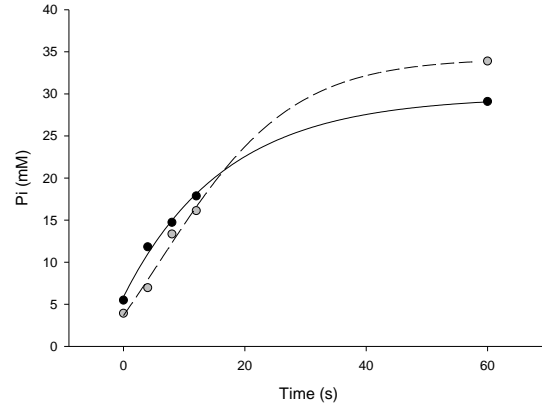
$$\dot{Pi} = Pi_a \cdot Pi_b \cdot \exp(-Pi_b \cdot (Ct)) \qquad (1)$$

The magnitude of changes in [Pi] were adjusted for current activation level (*act*) by dividing the output from equation 1 by the output of an equation that defined the rate of [PCr] depletion as a function of current activation level. This equation was formulated based on in vivo observation of initial [PCr] depletion rate at multiple contraction intensities. This relationship was fit with a 3 parameter exponential decay function. The first derivative of this function was used with equation 1 to define the [Pi]
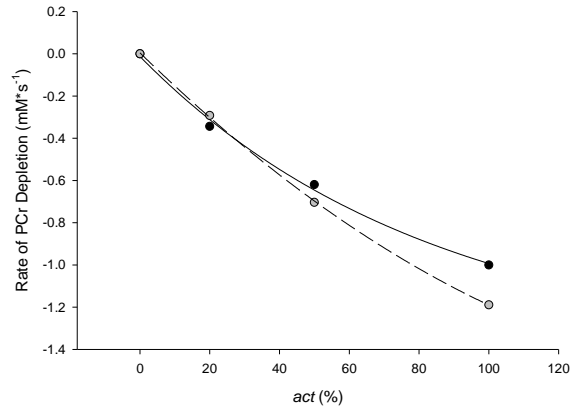
accumulation, scaled to current activation level (*act_rel*) and the maximum observed rate of PCr depletion ($Dep_{max} = 0.9944$ mM·s^{-1}). Corresponding data and fit are shown for the Young model (grey circles and dashed line respectively).

$$act_{rel} = (^-1.4175 + 1.4046 \cdot \exp(-0.012 \cdot (act \cdot 100))) / Dep_{max} \qquad (2)$$

155

Recovery

Similar to the Young model, the present application depends heavily on calculation of [Pi] during contraction and subsequent recovery. Again, a hybrid of [Pi] and [PCr] recovery kinetics were used to formulate functions that predicted [Pi] in the model. For either metabolite, recovery kinetics were described by a function whose derivation was similar to that of the Young model (equation 3, Appendix E):

$$\dot{Pi} = {}^{-}Pi_{ar} \cdot Pi_{br} \cdot \exp({}^{-}Pi_{br} \cdot Rt) \tag{3}$$

The rate and amplitude recovery coefficients for equation 3 (Pi_{ar} and Pi_{br}) were dependent on the degree of [Pi] accumulation at the end of the preceding contraction (Pi_P mM). Again, this feature of the model is similar to that outlined for the Young model (Appendix E, equations 4 and 5).

Pi_{br} varied minimally as a function of Pi_P in contrast to observations that dictated the Young model. A similar function described the relationship between Pi_{br} and Pi_P regardless of whether Pi_{br} was calculated from [PCr] or [Pi] recovery kinetics. This relationship was used to determine Pi_{br} during recovery in the model. The results of the same procedure for the Young model are illustrated for comparison (grey circles, dashed line).
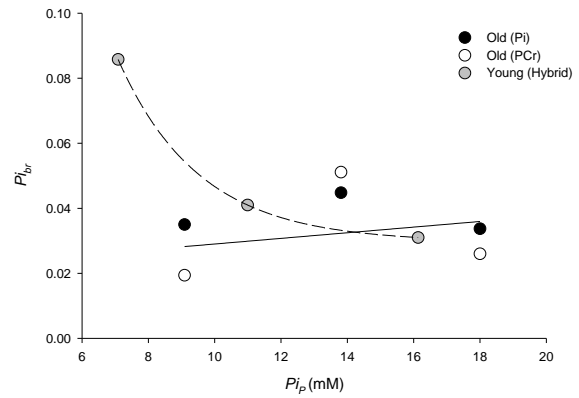
$$Pi_{br} = 0.0203 + 0.0009 \cdot Pi_p \tag{4}$$

The derivation for the function that defines recovery coefficient Pi_{ar} in the model was similar to that described for the Young model. However, the relationship between PiP and $Piar$ was fit with a quadratic equation (equation 5) because this approach improved the goodness of fit compared with a linear approximation. The formulation of Young model is included for the purposes of comparison (grey circles, dashed line).
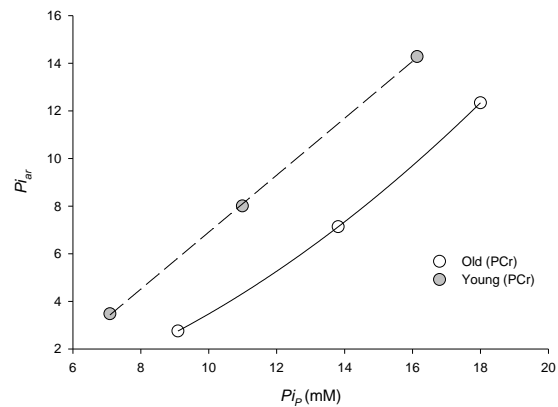
$$Pi_{ar} = -1.2379 + 0.117 \cdot Pi_p + 0.0354 \cdot Pi_p{}^2 \tag{5}$$

156

REFERENCE LIST

1. **Allen DG, Clugston E, Petersen Y, Roder IV, Chapman B and Rudolf R**. Interactions between intracellular calcium and phosphate in intact mouse muscle during fatigue. *J Appl Physiol* 111: 358-366, 2011.

2. **Allen DG, Lee JA and Westerblad H**. Intracellular calcium and tension during fatigue in isolated single muscle fibres from Xenopus laevis. *J Physiol* 415:433-58.: 433-458, 1989.

3. **Allman BL and Rice CL**. Incomplete recovery of voluntary isometric force after fatigue is not affected by old age. *Muscle Nerve* 24: 1156-1167, 2001.

4. **Allman BL and Rice CL**. An age-related shift in the force-frequency relationship affects quadriceps fatigability in old adults. *J Appl Physiol* 96: 1026-1032, 2004.

5. **Aniansson A, Grimby G and Rundgren A**. Isometric and Isokinetic Quadriceps Muscle Strength in 70 Year Old Men. *Scand J Rehab Med* 12: 161-168, 1980.

6. **Ansved T, Wallner P and Larsson L**. Spatial distribution of motor unit fibres in fast- and slow-twitch rat muscles with special reference to age. *Acta Physiol Scand* 143: 345-354, 1991.

7. **Barany M, Barany K, Burt CT, Glonek T and Myers TC**. Structural changes in myosin during contraction and the state of ATP in the intact frog muscle. *J Supramol Struct* 3: 125-140, 1975.

8. **Barany M and Close RI**. The transformation of myosin in cross-innervated rat muscles. *J Physiol* 213: 455-474, 1971.

9. **Bassey EJ, Fiatarone MA, O'Neill EF, Kelly M, Evans WJ and Lipsitz LA**. Leg extensor power and functional performance in very old men and women. *Clin Sci (Lond)* 82: 321-327, 1992.

10. **Baudry S, Klass M, Pasquet B and Duchateau J**. Age-related fatigability of the ankle dorsiflexor muscles during concentric and eccentric contractions. *Eur J Appl Physiol* 100: 515-525, 2007.

11. **Bazzucchi I, Marchetti M, Rosponi A, Fattorini L, Castellano V, Sbriccoli P and Felici F**. Differences in the force/endurance relationship between young and older men. *Eur J Appl Physiol* 93: 390-397, 2005.

12. **Bellemare F and Grassino A**. Evaluation of human diaphragm fatigue. *J Appl Physiol* 53: 1196-1206, 1982.

13. **Bilodeau M, Henderson TK, Nolta BE, Pursley PJ and Sandfort GL**. Effect of aging on fatigue characteristics of elbow flexor muscles during sustained submaximal contraction. *J Appl Physiol* 91: 2654-2664, 2001.

14. **Boska MD, Moussavi RS, Carson PJ, Weiner MW and Miller RG**. The metabolic basis of recovery after fatiguing exercise of human muscle. *Neurology* 40: 240-244, 1990.

15. **Brady AJ**. The three element model of muscle mechanics: its applicability to cardiac muscle. *Physiologist* 10: 75-86, 1967.

16. **Brierley EJ, Johnson MA, James OF and Turnbull DM**. Effects of physical activity and age on mitochondrial function. *QJM* 89: 251-258, 1996.

17. **Burt CT, Glonek T and Barany M**. Analysis of phosphate metabolites, the intracellular pH, and the state of adenosine triphosphate in intact muscle by phosphorus nuclear magnetic resonance. *J Biol Chem* 251: 2584-2591, 1976.

18. **Butler JE, Taylor JL and Gandevia SC**. Responses of human motoneurons to corticospinal stimulation during maximal voluntary contractions and ischemia. *J Neurosci* 23: 10224-10230, 2003.

19. **Calderon JC, Bolanos P, Torres SH, Rodriguez-Arroyo G and Caputo C**. Different fibre populations distinguished by their calcium transient characteristics in enzymatically dissociated murine flexor digitorum brevis and soleus muscles. *J Muscle Res Cell Motil* 30: 125-137, 2009.

20. **Callahan DM, Foulis SA and Kent-Braun JA**. Age-related fatigue resistance in the knee extensor muscles is specific to contraction mode. *Muscle Nerve* 39: 692-702, 2009.

21. **Chan KM, Raja AJ, Strohschein FJ and Lechelt K**. Age-related changes in muscle fatigue resistance in humans. *Can J Neurol Sci* 27: 220-228, 2000.

22. **Chasiotis D, Sahlin K and Hultman E**. Regulation of glycogenolysis in human muscle at rest and during exercise. *J Appl Physiol* 53: 708-715, 1982.

23. **Chilibeck PD, McCreary CR, Marsh GD, Paterson DH, Noble EG, Taylor AW and Thompson RT**. Evaluation of muscle oxidative potential by 31P-MRS during incremental exercise in old and young humans. *Eur J Appl Physiol* 78: 460-465, 1998.

24. **Christie A, Snook EM and Kent-Braun JA**. Systematic review and meta-analysis of skeletal muscle fatigue in old age. *Med Sci Sports Exerc* 43: 568-577, 2011.

25. **Chung LH, Callahan DM and Kent-Braun JA**. Age-related resistance to skeletal muscle fatigue is preserved during ischemia. *J Appl Physiol* 103: 1628-1635, 2007.

26. **Coggan AR, Abduljalil AM, Swanson SC, Earle MS, Farris JW, Mendenhall LA and Robitaille PM**. Muscle metabolism during exercise in young and older untrained and endurance-trained men. *J Appl Physiol* 75: 2125-2133, 1993.

27. **Coggan AR, Spina RJ, King DS, Rogers MA, Brown M, Nemeth PM and Holloszy JO**. Histochemical and enzymatic comparison of the gastrocnemius muscle of young and elderly men and women. *J Gerontol* 47: B71-B76, 1992.

28. **Cogshall J and Bekey G**. A stochastic model of skeletal muscle based on motor unit properties. *Mathematical Biosciences* 7: 405-419, 1970.

29. **Conley KE, Jubrias SA and Esselman PC**. Oxidative capacity and ageing in human muscle. *J Physiol* 526 Pt 1: 203-210, 2000.

30. **Connelly DM, Rice CL, Roos MR and Vandervoort AA**. Motor unit firing rates and contractile properties in tibialis anterior of young and old men. *J Appl Physiol* 87: 843-852, 1999.

31. **Cooke R, Franks K, Luciani GB and Pate E**. The inhibition of rabbit skeletal muscle contraction by hydrogen ions and phosphate. *J Physiol* 395:77-97.: 77-97, 1988.

32. **Crowther GJ, Carey MF, Kemper WF and Conley KE**. Control of glycolysis in contracting skeletal muscle. I. Turning it on. *Am J Physiol Endocrinol Metab* 282: E67-E73, 2002.

33. **Danieli-Betto D, Germinario E, Esposito A, Biral D and Betto R**. Effects of fatigue on sarcoplasmic reticulum and myofibrillar properties of rat single muscle fibers. *J Appl Physiol* 89: 891-898, 2000.

34. **Davies CTM, Thomas DO and White MJ**. Mechanical Properties of Young and Elderly Human Muscle. *Acta Med Scand* 711: 219-226, 1986.

35. **De Luca CJ, LeFever RS, McCue MP and Xenakis AP**. Control scheme governing concurrently active human motor units during voluntary contractions. *J Physiol* 329:129-42.: 129-142, 1982.

36. **Debold EP, Romatowski J and Fitts RH**. The depressive effect of Pi on the force-pCa relationship in skinned single muscle fibers is temperature dependent. *Am J Physiol Cell Physiol* 290: C1041-C1050, 2006.

37. **Degens H and Veerkamp JH**. Changes in oxidative capacity and fatigue resistance in skeletal muscle. *Int J Biochem* 26: 871-878, 1994.

38. **Dideriksen JL, Enoka RM and Farina D**. Neuromuscular adjustments that constrain submaximal EMG amplitude at task failure of sustained isometric contractions. *J Appl Physiol* 111: 485-494, 2011.

39. **Dideriksen JL, Farina D and Enoka RM**. Influence of fatigue on the simulated relation between the amplitude of the surface electromyogram and muscle force. *Philos Transact A Math Phys Eng Sci* 368: 2765-2781, 2010.

40. **Ding J, Wexler AS and Binder-Macleod SA**. A predictive model of fatigue in human skeletal muscles. *J Appl Physiol* 89: 1322-1332, 2000.

41. **Ding J, Wexler AS and Binder-Macleod SA**. A mathematical model that predicts the force-frequency relationship of human skeletal muscle. *Muscle Nerve* 26: 477-485, 2002.

42. **Ding J, Wexler AS and Binder-Macleod SA**. A predictive fatigue model--I: Predicting the effect of stimulation frequency and pattern on fatigue. *IEEE Trans Neural Syst Rehabil Eng* 10: 48-58, 2002.

43. **Ding J, Wexler AS and Binder-Macleod SA**. A predictive fatigue model--II: Predicting the effect of resting times on fatigue. *IEEE Trans Neural Syst Rehabil Eng* 10: 59-67, 2002.

44. **Ditor DS and Hicks AL**. The effect of age and gender on the relative fatigability of the human adductor pollicis muscle [In Process Citation]. *Can J Physiol Pharmacol* 78: 781-790, 2000.

45. **Dudel J**. Depolarization amplitude and Ca2+ -inflow control the time course of quantal releases at murine motor nerve terminals. *Eur J Neurosci* 30: 1219-1226, 2009.

46. **Fabiato A and Fabiato F**. Effects of pH on the myofilaments and the sarcoplasmic reticulum of skinned cells from cardiace and skeletal muscles. *J Physiol* 276:233-55.: 233-255, 1978.

47. **Faulkner JA, Davis CS, Mendias CL and Brooks SV**. The aging of elite male athletes: age-related changes in performance and skeletal muscle structure and function. *Clin J Sport Med* 18: 501-507, 2008.

48. **Fitts RH**. Cellular mechanisms of muscle fatigue. *Physiol Rev* 74: 49-94, 1994.

49. **Fitts RH**. Muscle fatigue: the cellular aspects. *Am J Sports Med* 24: S9-13, 1996.

50. **Fitts RH**. The cross-bridge cycle and skeletal muscle fatigue. *J Appl Physiol* 104: 551-558, 2008.

51. **Fitts RH and Balog EM**. Effect of intracellular and extracellular ion changes on E-C coupling and skeletal muscle fatigue. *Acta Physiol Scand* 156: 169-181, 1996.

52. **Fitts RH and Holloszy JO**. Contractile properties of rat soleus muscle: effects of training and fatigue. *Am J Physiol* 233: C86-C91, 1977.

53. **Forbes SC, Paganini AT, Slade JM, Towse TF and Meyer RA**. Phosphocreatine recovery kinetics following low- and high-intensity exercise in human triceps surae and rat posterior hindlimb muscles. *Am J Physiol Regul Integr Comp Physiol* 296: R161-R170, 2009.

54. **Fortune E and Lowery MM**. Effect of extracellular potassium accumulation on muscle fiber conduction velocity: a simulation study. *Ann Biomed Eng* 37: 2105-2117, 2009.

55. **Frontera WR, Hughes VA, Fielding RA, Fiatarone MA, Evans WJ and Roubenoff R**. Aging of skeletal muscle: a 12-yr longitudinal study. *J Appl Physiol* 88: 1321-1326, 2000.

56. **Frontera WR, Hughes VA, Lutz KJ and Evans WJ**. A cross-sectional study of muscle strength and mass in 45-78 year old men and women. *J Appl Physiol* 71: 644-650, 1991.

57. **Frontera WR, Meredith CN, O'Reilly KP, Knuttgen HG and Evans WJ**. Strength conditioning in older men: skeletal muscle hypertrophy and improved function. *J Appl Physiol* 64: 1038-1044, 1988.

58. **Fuglevand AJ and Segal SS**. Simulation of motor unit recruitment and microvascular unit perfusion: spatial considerations. *J Appl Physiol* 83: 1223-1234, 1997.

59. **Fuglevand AJ, Winter DA and Patla AE**. Models of recruitment and rate coding organization in motor-unit pools. *J Neurophysiol* 70: 2470-2488, 1993.

60. **Gacesa JZ, Jakovljevic DG, Kozic DB, Dragnic NR, Brodie DA and Grujic NG**. Morpho-functional response of the elbow extensor muscles to twelve-week self-perceived maximal resistance training. *Clin Physiol Funct Imaging* 2010.

61. **Galea V**. Electrical characteristics of human ankle dorsi- and plantar-flexor muscles. Comparative responses during fatiguing stimulation and recovery. *Eur J Appl Physiol* 85: 130-140, 2001.

62. **Giat Y, Mizrahi J and Levy M**. A musculotendon model of the fatigue profiles of paralyzed quadriceps muscle under FES. *IEEE Trans Biomed Eng* 40: 664-674, 1993.

63. **Giat Y, Mizrahi J and Levy M**. A model of fatigue and recovery in paraplegic's quadriceps muscle subjected to intermittent FES. *J Biomech Eng* 118: 357-366, 1996.

64. **Gregory CM, Vandenborne K and Dudley GA**. Metabolic enzymes and phenotypic expression among human locomotor muscles. *Muscle Nerve* 24: 387-393, 2001.

65. **Guralnik JM, Ferrucci L, Pieper CF, Leveille SG, Markides KS, Ostir GV, Studenski S, Berkman LF and Wallace RB**. Lower extremity function and subsequent disability: consistency across studies, predictive models, and value of gait speed alone compared with the short physical performance battery. *J Gerontol A Biol Sci Med Sci* 55: M221-M231, 2000.

66. **Guralnik JM, Ferrucci L, Simonsick EM, Salive ME and Wallace RB**. Lower-extremity function in persons over the age of 70 years as a predictor of subsequent disability. *N Engl J Med* 332: 556-561, 1995.

67. **Gustafsson B and Pinter MJ**. An investigation of threshold properties among cat spinal alpha-motoneurones. *J Physiol* 357:453-83.: 453-483, 1984.

68. **Guth L, Samaha FJ and Albers RW**. The neural regulation of some phenotypic differences between the fiber types of mammalian skeletal muscle. *Exp Neurol* 26: 126-135, 1970.

69. **Hakkinen K**. Neuromuscular fatigue and recovery in women at different ages during heavy resistance loading. *Electromyogr Clin Neurophysiol* 35: 403-413, 1995.

70. **Hanson J and Huxley HE**. Structural basis of the cross-striations in muscle. *Nature* 19;172: 530-532, 1953.

71. **Harridge SD**. Plasticity of human skeletal muscle: gene expression to in vivo function. *Exp Physiol* 92: 783-797, 2007.

72. **Hasson CJ, Caldwell GE and Van Emmerik RE**. Scaling of plantarflexor muscle activity and postural time-to-contact in response to upper-body perturbations in young and older adults. *Exp Brain Res* 196: 413-427, 2009.

73. **Hasson CJ, Miller RH and Caldwell GE**. Contractile and elastic ankle joint muscular properties in young and older adults. *PLoS One* 6: e15953, 2011.

74. **Hawkins D and Hull ML**. Muscle force as affected by fatigue: mathematical model and experimental verification. *J Biomech* 26: 1117-1128, 1993.

75. **Hawkins DA and Hull ML**. An activation-recruitment scheme for use in muscle modeling. *J Biomech* 25: 1467-1476, 1992.

76. **He J, Levin VS and Loeb GE**. Feedback Gains for Correcting Small Perturbations to Standing Posture. *IEEE Trans Autom Control* 1: 322-332, 1991.

77. **Heckman CJ and Binder MD**. Computer simulation of the steady-state input-output function of the cat medial gastrocnemius motoneuron pool. *J Neurophysiol* 65: 952-967, 1991.

78. **Henneman E**. Relation between size of neurons and their susceptibility to discharge. *Science* 126: 1345-1347, 1957.

79. **Henneman E, Somjen G and Carpenter DO**. FUNCTIONAL SIGNIFICANCE OF CELL SIZE IN SPINAL MOTONEURONS. *J Neurophysiol* 28: 560-580, 1965.

80. **Hepple RT, Hagen JL, Krause DJ and Baker DJ**. Skeletal muscle aging in F344BN F1-hybrid rats: II. Improved contractile economy in senescence helps compensate for reduced ATP-generating capacity. *J Gerontol A Biol Sci Med Sci* 59: 1111-1119, 2004.

81. **Hill AV**. The Heat of Shortening and the Dynamic Constants of Muscle. *Proceedings of the Royal Society of London Series B, Biological Sciences* 126: 136-195, 1938.

82. **Hill AV**. The heat of activation and the heat of shortening in a muscle twitch. *Proc R Soc Lond B Biol Sci* 136: 195-211, 1949.

83. **Hill TL**. Two elementary models for the regulation of skeletal muscle contraction by calcium. *Biophys J* 44: 383-396, 1983.

84. **Hoult DI, Busby SJ, Gadian DG, Radda GK, Richards RE and Seeley PJ**. Observation of tissue metabolites using 31P nuclear magnetic resonance. *Nature* 252: 285-287, 1974.

85. **Houmard JA, Weidner ML, Gavigan KE, Tyndall GL, Hickey MS and Alshami A**. Fiber type and citrate synthase activity in the human gastrocnemius and vastus lateralis with aging. *J Appl Physiol* 85: 1337-1341, 1998.

86. **Hunter SK**. Sex differences and mechanisms of task-specific muscle fatigue. *Exerc Sport Sci Rev* 37: 113-122, 2009.

87. **Hunter SK, Butler JE, Todd G, Gandevia SC and Taylor JL**. Supraspinal fatigue does not explain the sex difference in muscle fatigue of maximal contractions. *J Appl Physiol* 101: 1036-1044, 2006.

88. **Hunter SK, Critchlow A and Enoka RM**. Muscle endurance is greater for old men compared with strength-matched young men. *J Appl Physiol* 99: 890-897, 2005.

89. **Hunter SK, Thompson MW, Ruell PA, Harmer AR, Thom JM, Gwinn TH and Adams RD**. Human skeletal sarcoplasmic reticulum Ca2+ uptake and muscle function with aging and strength training. *J Appl Physiol* 86: 1858-1865, 1999.

90. **Huxley HE**. The double array of filaments in cross-striated muscle. *J Biophys Biochem Cytol* 3: 631-648, 1957.

91. **Huxley HE**. Structural changes during muscle contraction. *Biochem J* 125: 85P, 1971.

92. **Jakobsson A, Borg K and Edstrom L**. Fiber-type composition, structure and cytoskeletal protein location of fibres in anterior tibial muscle. *Acta Neuropath* 80: 459-468, 1990.

93. **Jarvis JC, Sutherland H, Mayne CN, Gilroy SJ and Salmons S**. Induction of a fast-oxidative phenotype by chronic muscle stimulation: mechanical and biochemical studies. *Am J Physiol* 270: C306-C312, 1996.

94. **Jeneson JA, Schmitz JP, van den Broek NM, van Riel NA, Hilbers PA, Nicolay K and Prompers JJ**. Magnitude and control of mitochondrial sensitivity to ADP. *Am J Physiol Endocrinol Metab* 297: E774-E784, 2009.

95. **Jewell BR and Wilkie DR**. An analysis of the mechanical components in frog's striated muscle. *J Physiol* 143: 515-540, 1958.

96. **Kamen G and De Luca CJ**. Unusual motor unit firing behavior in older adults. *Brain Res* 482: 136-140, 1989.

97. **Kamen G and Knight CA**. Training-related adaptations in motor unit discharge rate in young and older adults. *J Gerontol A Biol Sci Med Sci* 59: 1334-1338, 2004.

98. **Kamen G, Sison SV, Duke Du CC and Patten C**. Motor unit discharge behavior in older adults during maximal-effort contractions. *J Appl Physiol* 79(6): 1908-1913, 1995.

99. **Kemp GJ**. Physiological constraints on changes in pH and phosphorus metabolite concentrations in ischemically exercising muscle: implications for metabolic control and for the interpretation of 31P-magnetic resonance spectroscopic studies. *MAGMA* 5: 231-241, 1997.

100. **Kemp GJ, Roussel M, Bendahan D, Le Fur Y and Cozzone PJ**. Interrelations of ATP synthesis and proton handling in ischaemically exercising human forearm muscle studied by 31P magnetic resonance spectroscopy. *J Physiol* 535: 901-928, 2001.

101. **Kemp GJ, Taylor DJ and Radda GK**. Control of phosphocreatine resynthesis during recovery from exercise in human skeletal muscle. *NMR Biomed* 6: 66-72X, 1993.

102. **Kemp GJ, Thompson CH, Taylor DJ and Radda GK**. Proton efflux in human skeletal muscle during recovery from exercise. *Eur J Appl Physiol Occup Physiol* 76: 462-471, 1997.

103. **Kent-Braun JA**. Central and peripheral contributions to muscle fatigue in humans during sustained maximal effort. *Eur J Appl Physiol* 80: 57-63, 1999.

104. **Kent-Braun JA and Ng AV**. Specific strength and voluntary muscle activation in young and elderly women and men. *J Appl Physiol* 87: 22-29, 1999.

105. **Kent-Braun JA and Ng AV**. Skeletal muscle oxidative capacity in young and older women and men. *J Appl Physiol* 89: 1072-1078, 2000.

106. **Kent-Braun JA, Ng AV, Doyle JW and Towse TF**. Human skeletal muscle responses vary with age and gender during fatigue due to incremental isometric exercise. *J Appl Physiol* 93: 1813-1823, 2002.

107. **Khang G and Zajac FE**. Paraplegic standing controlled by functional neuromuscular stimulation: Part II--Computer simulation studies. *IEEE Trans Biomed Eng* 36: 885-894, 1989.

108. **Klass M, Baudry S and Duchateau J**. Aging does not affect voluntary activation of the ankle dorsiflexors during isometric, concentric, and eccentric contractions. *J Appl Physiol* 99: 31-38, 2005.

109. **Krause U and Wegener G**. Control of glycolysis in vertebrate skeletal muscle during exercise. *Am J Physiol* 270: R821-R829, 1996.

110. **Lanza IR, Befroy DE and Kent-Braun JA**. Age-related changes in ATP-producing pathways in human skeletal muscle in vivo. *J Appl Physiol* 2005.

111. **Lanza IR, Larsen RG and Kent-Braun JA**. Effects of old age on human skeletal muscle energetics during fatiguing contractions with and without blood flow. *J Physiol* 583: 1093-1105, 2007.

112. **Lanza IR, Russ DW and Kent-Braun JA**. Age-related enhancement of fatigue resistance is evident in men during both isometric and dynamic tasks. *J Appl Physiol* 97: 967-975, 2004.

113. **Lanza IR, Wigmore DM, Befroy DE and Kent-Braun JA**. In vivo ATP production during free-flow and ischemic muscle contractions in humans. *J Physiol* 2006.

114. **Larsen RG, Callahan DM, Foulis SA and Kent-Braun JA**. In vivo oxidative capacity varies with muscle and training status in young adults. *J Appl Physiol* 107: 873-879, 2009.

115. **Larsson L**. Motor units: remodeling in aged animals. *J Gerontol A Biol Sci Med Sci* 50 Spec No: 91-95, 1995.

116. **Larsson L, Li X, Yu F and Degens H**. Age-related changes in contractile properties and expression of myosin isoforms in single skeletal muscle cells. *Muscle Nerve Suppl* 5: S74-S78, 1997.

117. **Lennmarken C, Bergman T, Larsson J and Larsson LE**. Skeletal muscle function in man:force, relaxation rate, endurance and contraction time-dependence on sex and age. *Clinical Physiology* 5: 243-255, 1985.

118. **Levin O and Mizrahi J**. EMG and metabolite-based prediction of force in paralyzed quadriceps muscle under interrupted stimulation. *IEEE Trans Rehabil Eng* 7: 301-314, 1999.

119. **Lexell J**. Ageing and human muscle: observations from Sweden. *Can J Appl Physiol* 18: 2-18, 1993.

120. **Liu JZ, Brown RW and Yue GH**. A dynamical model of muscle activation, fatigue, and recovery. *Biophys J* 82: 2344-2359, 2002.

121. **Lloyd DG and Besier TF**. An EMG-driven musculoskeletal model to estimate muscle forces and knee joint moments in vivo. *J Biomech* 36: 765-776, 2003.

122. **Lopez-Guajardo A, Sutherland H, Jarvis JC and Salmons S**. Induction of a fatigue-resistant phenotype in rabbit fast muscle by small daily amounts of stimulation. *J Appl Physiol* 90: 1909-1918, 2001.

123. **Lymn RW and Taylor EW**. Mechanism of adenosine triphosphate hydrolysis by actomyosin. *Biochemistry* 10: 4617-4624, 1971.

124. **Macintosh BR, Jones D, Devrome AN and Rassier DE**. Prediction of summation in incompletely fused tetanic contractions of rat muscle. *J Biomech* 40: 1066-1072, 2007.

125. **Mademli L and Arampatzis A**. Effect of voluntary activation on age-related muscle fatigue resistance. *J Biomech* 41: 1229-1235, 2008.

126. **Maganaris CN**. A predictive model of moment-angle characteristics in human skeletal muscle: application and validation in muscles across the ankle joint. *J Theor Biol* 230: 89-98, 2004.

127. **Maganaris CN, Baltzopoulos V, Ball D and Sargeant AJ**. In vivo specific tension of human skeletal muscle. *J Appl Physiol* 90: 865-872, 2001.

128. **Marion MS, Wexler AS and Hull ML**. Predicting fatigue during electrically stimulated non-isometric contractions. *Muscle Nerve* 41: 857-867, 2010.

129. **Martonosi AN**. Mechanisms of Ca2+ release from sarcoplasmic reticulum of skeletal muscle. *Physiol Rev* 64: 1240-1320, 1984.

130. **McNeil CJ and Rice CL**. Fatigability is increased with age during velocity-dependent contractions of the dorsiflexors. *J Gerontol A Biol Sci Med Sci* 62: 624-629, 2007.

131. **Melzer W, Rios E and Schneider MF**. Time course of calcium release and removal in skeletal muscle fibers. *Biophys J* 45: 637-641, 1984.

132. **Metzger JM and Fitts RH**. Role of intracellular pH in muscle fatigue. *J Appl Physiol* 62: 1392-1397, 1987.

133. **Metzger JM and Moss RL**. Greater hydrogen ion-induced depression of tension and velocity in skinned single fibres of rat fast than slow muscles. *J Physiol* 393:727-42.: 727-742, 1987.

134. **Meyer RA**. A linear model of muscle respiration explains monoexponential phosphocreatine changes. *Am J Physiol* 254: C548-53, 1988.

135. **Miller RG, Boska MD, Moussavi RS, Carson PJ and Weiner MW**. 31P nuclear magnetic resonance studies of high energy phosphates and pH in human muscle fatigue. Comparison of aerobic and anaerobic exercise. *J Clin Invest* 81: 1190-1196, 1988.

136. **Milner-Brown HS, Stein RB and Yemm R**. Changes in firing rate of human motor units during linearly changing voluntary contractions. *J Physiol* 230: 371-390, 1973.

137. **Mizrahi J, Seelenfreund D, Isakov E and Susak Z**. Predicted and measured muscle forces after recoveries of differing durations following fatigue in functional electrical stimulation. *Artif Organs* 21: 236-239, 1997.

138. **Moon RB and Richards JH**. Determination of intracellular pH by 31P magnetic resonance. *J Biol Chem* 248: 7276-7278, 1973.

139. **Narayanan N, Jones DL, Xu A and Yu JC**. Effects of aging on sarcoplasmic reticulum function and contraction duration in skeletal muscles of the rat. *Am J Physiol* 271: C1032-C1040, 1996.

140. **Narici MV, Bordini M and Cerretelli P**. Effect of aging on human adductor pollicis muscle function. *J Appl Physiol* 71: 1277-1281, 1991.

141. **Narici MV, Roi GS, Landoni L, Minetti AE and Cerretelli P**. Changes in force, cross-sectional area and neural activation during strength training and detraining of the human quadriceps. *Eur J Appl Physiol* 59: 310-319, 1989.

142. **Nielsen OB and de Paoli FV**. Regulation of Na+-K+ homeostasis and excitability in contracting muscles: implications for fatigue. *Appl Physiol Nutr Metab* 32: 974-984, 2007.

143. **Nosek TM, Fender KY and Godt RE**. It is diprotonated inorganic phosphate that depresses force in skinned skeletal muscle fibers. *Science* 236: 191-193, 1987.

144. **Ochala J, Frontera WR, Dorer DJ, Van Hoecke J and Krivickas LS**. Single skeletal muscle fiber elastic and contractile characteristics in young and older men. *J Gerontol A Biol Sci Med Sci* 62: 375-381, 2007.

145. **Oya T, Riek S and Cresswell AG**. Recruitment and rate coding organisation for soleus motor units across entire range of voluntary isometric plantar flexions. *J Physiol* 587: 4737-4748, 2009.

146. **Pate E and Cooke R**. A model of crossbridge action: the effects of ATP, ADP and Pi. *J Muscle Res Cell Motil* 10: 181-196, 1989.

147. **Patten C, Kamen G and Rowland DM**. Adaptations in maximal motor unit discharge rate to strength training in young and older adults. *Muscle Nerve* 24: 542-550, 2001.

148. **Pell KM and Stanfield JW, Jr.** Mechanical model of skeletal muscle. *Am J Phys Med* 51: 23-38, 1972.

149. **Petrella JK, Kim JS, Tuggle SC, Hall SR and Bamman MM**. Age differences in knee extension power, contractile velocity, and fatigability. *J Appl Physiol* 98: 211-220, 2005.

150. **Powers RK and Binder MD**. Experimental evaluation of input-output models of motoneuron discharge. *J Neurophysiol* 75: 367-379, 1996.

151. **Quinonez M, Gonzalez F, Morgado-Valle C and DiFranco M**. Effects of membrane depolarization and changes in extracellular [K(+)] on the Ca (2+) transients of fast skeletal muscle fibers. Implications for muscle fatigue. *J Muscle Res Cell Motil* 31: 13-33, 2010.

152. **Quistorff B, Johansen L and Sahlin K**. Absence of phosphocreatine resynthesis in human muscle during ischaemic recovery. *Biochem J* 291: 681-686, 1992.

153. **Rabischong E and Chavet P**. Regression-based indices of fatigue in paraplegics' electrically stimulated quadriceps. *Med Eng Phys* 19: 749-754, 1997.

154. **Rasmussen UF, Krustrup P, Kjaer M and Rasmussen HN**. Experimental evidence against the mitochondrial theory of aging. A study of isolated human skeletal muscle mitochondria. *Exp Gerontol* 38: 877-886, 2003.

155. **Ren JM, Chasiotis D, Bergstrom M and Hultman E**. Skeletal muscle glucolysis, glycogenolysis and glycogen phosphorylase during electrical stimulation in man. *Acta Physiol Scand* 133: 101-107, 1988.

156. **Rico-Sanz J**. Progressive decrease of intramyocellular accumulation of H+ and Pi in human skeletal muscle during repeated isotonic exercise. *Am J Physiol Cell Physiol* 284: C1490-C1496, 2003.

157. **Riener R, Quintern J and Schmidt G**. Biomechanical model of the human knee evaluated by neuromuscular stimulation. *J Biomech* 29: 1157-1167, 1996.

158. **Ritchie JM and Wilkie DR**. The dynamics of muscular contraction. *J Physiol* 143: 104-113, 1958.

159. **Rohmert W**. [On the theory of recovery pauses in dynamic work.]. *Int Z Angew Physiol* 18:191-212.: 191-212, 1960.

160. **Rubinstein S and Kamen G**. Decreases in motor unit firing rate during sustained maximal-effort contractions in young and older adults. *J Electromyogr Kinesiol* 15: 536-543, 2005.

161. **Russ DW, Vandenborne K, Walter GA, Elliott M and Binder-Macleod SA**. Effects of muscle activation on fatigue and metabolism in human skeletal muscle. *J Appl Physiol* 92: 1978-1986, 2002.

162. **Saltin B, Henriksson J, Nygaard E, Andersen P and Jansson E**. Fiber types and metabolic potentials of skeletal muscles in sedentary man and endurance runners. *Ann N Y Acad Sci* 301:3-29.: 3-29, 1977.

163. **Samaha FJ, Guth L and Albers RW**. The neural regulation of gene expression in the muscle cell. *Exp Neurol* 27: 276-282, 1970.

164. **Samson MM, Meeuwsen IB, Crowe A, Dessens JA, Duursma SA and Verhaar HJ**. Relationships between physical performance measures, age, height and body weight in healthy adults. *Age Ageing* 29: 235-242, 2000.

165. **Short KR, Bigelow ML, Kahl J, Singh R, Coenen-Schimke J, Raghavakaimal S and Nair KS**. Decline in skeletal muscle mitochondrial function with aging in humans. *Proc Natl Acad Sci U S A* 102: 5618-5623, 2005.

166. **Shorten PR, O'Callaghan P, Davidson JB and Soboleva TK**. A mathematical model of fatigue in skeletal muscle force contraction. *J Muscle Res Cell Motil* 28: 293-313, 2007.

167. **Sirikul B, Hunter GR, Larson-Meyer DE, Desmond R and Newcomer BR**. Relationship between metabolic function and skeletal muscle fatigue during a 90 s maximal isometric contraction. *Appl Physiol Nutr Metab* 32: 394-399, 2007.

168. **Stackhouse SK, Stevens JE, Lee SC, Pearce KM, Snyder-Mackler L and Binder-Macleod SA**. Maximum voluntary activation in nonfatigued and fatigued muscle of young and elderly individuals. *Phys Ther* 81: 1102-1109, 2001.

169. **Stary CM, Mathieu-Costello O and Hogan MC**. Resistance to fatigue of individual Xenopus single skeletal muscle fibres is correlated with mitochondrial volume density. *Exp Physiol* 89: 617-621, 2004.

170. **Stephenson DG and Williams DA**. Calcium-activated force responses in fast- and slow-twitch skinned muscle fibres of the rat at different temperatures. *J Physiol* 317:281-302.: 281-302, 1981.

171. **Tang CY, Stojanovic B, Tsui CP and Kojic M**. Modeling of muscle fatigue using Hill's model. *Biomed Mater Eng* 15: 341-348, 2005.

172. **Taylor JL, Allen GM, Butler JE and Gandevia SC**. Supraspinal fatigue during intermittent maximal voluntary contractions of the human elbow flexors. *J Appl Physiol* 89: 305-313, 2000.

173. **Taylor JL and Gandevia SC**. A comparison of central aspects of fatigue in submaximal and maximal voluntary contractions. *J Appl Physiol* 104: 542-550, 2008.

174. **Tevald MA, Foulis SA, Lanza IR and Kent-Braun JA**. Lower energy cost of skeletal muscle contractions in older humans. *Am J Physiol Regul Integr Comp Physiol* 298: R729-R739, 2010.

175. **Thelen DG**. Adjustment of muscle mechanics model parameters to simulate dynamic contractions in older adults. *J Biomech Eng* 125: 70-77, 2003.

176. **Trappe TA, Lindquist DM and Carrithers JA**. Muscle-specific atrophy of the quadriceps femoris with aging. *J Appl Physiol* 90: 2070-2074, 2001.

177. **Umberger BR, Gerritsen KG and Martin PE**. A model of human muscle energy expenditure. *Comput Methods Biomech Biomed Engin* 6: 99-111, 2003.

178. **Van Cutsem M, Feiereisen P, Duchateau J and Hainaut K**. Mechanical properties and behaviour of motor units in the tibialis anterior during voluntary contractions. *Can J Appl Physiol* 22: 585-597, 1997.

179. **van den Broek NM, De Feyter HM, de Graaf L, Nicolay K and Prompers JJ**. Intersubject differences in the effect of acidosis on phosphocreatine recovery kinetics in muscle after exercise are due to differences in proton efflux rates. *Am J Physiol Cell Physiol* 293: C228-C237, 2007.

180. **van der Laarse WJ, Diegenbach PC and Elzinga G**. Maximum rate of oxygen consumption and quantitative histochemistry of succinate dehydrogenase in single muscle fibres of Xenopus laevis. *J Muscle Res Cell Motil* 10: 221-228, 1989.

181. **van Soest AJ, Schwab AL, Bobbert MF and Ingen Schenau GJ**. The influence of the biarticularity of the gastrocnemius muscle on vertical-jumping achievement. *J Biomech* 26: 1-8, 1993.

182. **Walsh B, Howlett RA, Stary CM, Kindig CA and Hogan MC**. Measurement of activation energy and oxidative phosphorylation onset kinetics in isolated muscle fibers in the absence of cross-bridge cycling. *Am J Physiol Regul Integr Comp Physiol* 290: R1707-R1713, 2006.

183. **Walter G, Vandenborne K, Elliott M and Leigh JS**. In vivo ATP synthesis rates in single human muscles during high intensity exercise. *J Physiol* 519 Pt 3: 901-910, 1999.

184. **Walter G, Vandenborne K, McCully KK and Leigh JS**. Noninvasive measurement of phosphocreatine recovery kinetics in single human muscles. *Am J Physiol* 272: C525-C534, 1997.

185. **Webber SC, Porter MM and Gardiner PF**. Modeling age-related neuromuscular changes in humans. *Appl Physiol Nutr Metab* 34: 732-744, 2009.

186. **Westerblad H, Allen DG, Bruton JD, Andrade FH and Lannergren J**. Mechanisms underlying the reduction of isometric force in skeletal muscle fatigue. *Acta Physiol Scand* 162: 253-260, 1998.

187. **Wexler AS, Ding J and Binder-Macleod SA**. A mathematical model that predicts skeletal muscle force. *IEEE Trans Biomed Eng* 44: 337-348, 1997.

188. **Wilkie DR**. The mechanical properties of muscle. *Br Med Bull* 12: 177-182, 1956.

189. **Winters JM and Stark L**. Muscle models: what is gained and what is lost by varying model complexity. *Biol Cybern* 55: 403-420, 1987.

190. **Xia T and Frey Law LA**. A theoretical approach for modeling peripheral muscle fatigue and recovery. *J Biomech* 20;41: 3046-3052, 2008.

191. **Yoon T, De Lap BS, Griffith EE and Hunter SK**. Age-related muscle fatigue after a low-force fatiguing contraction is explained by central fatigue. *Muscle Nerve* 37: 457-466, 2008.

192. **Zahalak GI and Ma SP**. Muscle activation and contraction: constitutive relations based directly on cross-bridge kinetics. *J Biomech Eng* 112: 52-62, 1990.

193. **Zhang SJ, Andersson DC, Sandstrom ME, Westerblad H and Katz A**. Cross bridges account for only 20% of total ATP consumption during submaximal isometric contraction in mouse fast-twitch skeletal muscle. *Am J Physiol Cell Physiol* 291: C147-C154, 2006.